UNIVERSITÀ
DEGLI STUDI
DI PADOVA

Sede Amministrativa: Università degli Studi di Padova

Department of: Information Engineering

CORSO DI DOTTORATO DI RICERCA IN: INGEGNERIA DELL'INFORMAZIONE
CURRICOLO: BIOINGEGNERIA
CYCLE: 29th

Retinal Vascular Measurement Tools for Diagnostic Feature Extraction

Thesis written with the financial support of:
Marie Curie grant from the European Commission in the framework of the REVAMMAD ITN (Initial Training Research network), Project number 316990

Supervisore: Alfredo Ruggeri

Dottorando : Jeffrey Wigdahl

Retinal Vascular Measurement Tools for Diagnostic Feature Extraction

Jeffrey Wigdahl

Submitted in total fulfilment of the requirements of the degree of

Doctor of Philosophy

Department of Information Engineering

UNIVERSITA DEGLI STUDI DI PADOVA

November 2016

Abstract

The contributions of this work are in the development of new and state of the art algorithms for retinal image analysis including optic disc detection, tortuosity estimation, and cross-over abnormality detection. The retina is one of the only areas of the human body that blood vessels can be visualized noninvasively. Retinal imaging has become a standard in the ophthalmologist's office because it is an easy and inexpensive way to monitor not just eye health, but also systemic vascular diseases. Changes to the retinal vasculature can be the early signs of diseases such as diabetic and hypertensive retinopathy, of which early detection can save vision, money, and improve overall health for the patient. When looking at the retinal vasculature, ophthalmologists generally rely on a qualitative assessment which can make comparisons over time or between different ophthalmologists difficult. Computer aided systems are now able to quantify what the ophthalmologist is qualitatively measuring in what they consider to be the most important features of the vasculature. These include, but are not limited to, tortuosity, arteriolar narrowing, cross-over abnormalities, and artery-vein (AV) ratio. The University of Padova has created a semi-automatic system for detecting and quantifying retinal vessels starting from optic disc detection, vessel segmentation, width estimation, tortuosity calculation, AV classification, and AV ratio. We propose a new method for optic disc detection that converts the retinal image into a graph and exploits vessel enhancement methods to calculate edge weights in finding the shortest path between pairs of points on the periphery of the image. The line segment with the maximum number of shortest paths is considered the optic disc location. The method was tested on three publicly available datasets: DRIVE, DIARETDB1, and Messidor consisting of 40, 89, and 1200 images and achieved an accuracy of 100, 98.88, and 99.42% respectively. The second contribution is a new algorithm for calculating abnormalities at AV crossing points. In retinal images, Gunn's sign appears as a tapering of the vein at a crossing point, while Salus's sign presents as an S-shaped

curving. This work presents a method for the automatic quantification of these two signs once a crossover has been detected; combining segmentation, artery vein classification, and morphological feature extraction techniques to calculate vein widths and angles entering and exiting the crossover. Results on two datasets show separation between the two classes and that we can reliably detect and quantify these signs under the right conditions. The last contribution in tortuosity consists of two parts. A comparative study was performed on several of the most popular methods for tortuosity estimation on a new vessel dataset. Results show that several methods have good Cohen's kappa agreement with both graders, while the tortuosity density metric has the highest single metric average agreement across vessel type and grader. The second is a new way to enhance curvature in segmented vessels based on a difference of Gabor filters to create a curvature enhanced image. The proposed method was tested on the RET-TORT database using several methods to calculate tortuosity, and had best Pearson's correlation of .94 for arteries and .882 for veins, outperforming single mathematical formulations on the data. This held true after testing the method on the propose dataset as well, having higher correlation values across grader and vessel type compared with other tortuosity metrics.

Summary of Results:

The optic disc detection method was tested on three publicly available datasets: DRIVE, DIARETDB1, and Messidor consisting of 40, 89, and 1200 images and achieved an accuracy of 100, 98.88, and 99.42% respectively.

The AV nicking quantification method was tested on a small dataset of 10 crossing provided by doctors at Papageorgiou Hospital, Aristotle University of Thessaloniki, Thessaloniki, Greece. Results showed separation between the normal and abnormal classes for both the Gunn and Salus sign. The method was then tested on a larger, publicly available dataset which showed good separation for the Gunn sign.

The proposed tortuosity method was tested on the RET-TORT database using several methods to calculate tortuosity, and had best Pearson's correlation of .94 for arteries and .882 for veins, outperforming single mathematical formulations on the data. It was then tested on the dataset proposed in this thesis, further corroborating the effectiveness of the method.

Acknowledgements

I would like to take this moment to express my gratitude to the people who helped make this research possible. To my advisor, Prof. Alfredo Ruggeri, for giving his support, guidance and giving us the freedom to explore interesting topics. His decades of knowledge and experience were invaluable to the success of this project. I would also like thank Prof. Emanuele Trucco for supporting me in my time at the University of Dundee. Also, to the students and staff at the University of Padova for their help traversing the Italian system.

I would like to thank the entire REVAMMAD training network for providing their knowledge, experience and time in ensuring that the early stage researchers received the best training possible. Our meetings at the University of Lincoln, Charitè Medical University in Berlin, FORTH Computer Science Institute in Crete and the University of Padova provided us with the background knowledge necessary to carry out our research. A special thanks to Dr. Andrew Hunter for putting together this European project and compiling the leaders in multiple fields to ensure a well-rounded teaching experience. To the ESR's, whom there are too many to name, thank you for sharing this experience with me. A special thanks to Pedro Guimaraes, Georgios Leontidis, Roberto Annunziata, Carlos Matas, and Sergio Crespo, for our collaborations through the project.

Finally I would like to thank my wife, parents, brother and sister for supporting me while I undertook this three year journey. Their love, support and motivation made this a much easier time than it could have been.

Preface

This thesis has been written at the Department of Information Engineering, The University of Padova. The novelty of this thesis resides in the new and state-of-the-art algorithms developed for optic disc detection, AV nicking and tortuosity estimation, expanded upon in the following chapters and based on the following publications.

Chapter 3 is based on the following publication:

1. Jeffrey Wigdahl, Pedro Guimaraes, Alfredo Ruggeri. “A Shortest Path Approach to Optic Disc Detection in Retinal Fundus Images”, Journal of Modelling in Ophthalmology, Vol. 2 2016. (accepted)

Chapter 4 is based on the following publication:

1. Jeffrey Wigdahl, Pedro Guimaraes, Georgios Leontidis, Areti Triantafyllou, Alfredo Ruggeri. “Automatic Gunn and Salus sign quantification in retinal images”, Proceedings of the Annual International Conference of the IEEE Engineering in Medicine and Biology Society, EMBS, 2015.

Chapter 5 is based on the following publications:

1. Wigdahl, J., Annunziata, R., Hughes, L., Borooah, S., Trucco, E., Ruggeri, A., Retinal Image Database for Tortuosity Estimation, Association for Research in Vision and Ophthalmology (ARVO) 2016.
2. Jeffrey Wigdahl, Pedro Guimaraes, Alfredo Ruggeri. “Difference of Gabor Filters as a Curvature Feature in Tortuosity Estimation”, Proceedings of the Annual International Conference of the IEEE Engineering in Medicine and Biology Society, EMBS, 2016.

Chapter 6 is based on the following:

1. Wigdahl, J., Guimaraes, P., Poletti, E., Ruggeri, A., ReVMS (Retinal Vessel Measurement System), ARVO 2015

Table of Contents

List of Figures

List of Tables

Chapter 1

Introduction

1.1. Motivation

The eye is said to be a window into the body. Through this window, we can get a unique view at the body's microcirculation. Abnormal changes here not only impact eye health, but also the general health of the body. Systemic diseases, such as hypertension and diabetes, can show up as abnormal changes in the retinal vasculature [16]. These diseases have had a serious impact on society and continue to grow in prevalence throughout the world.

According to the World Health Organization (WHO), 40% of adults over the age of 25 have hypertension (defined as systolic blood pressure greater than 140mmHg and diastolic over 90mmHg). These percentages are higher in low to middle income countries, where people are more likely to go undiagnosed, untreated and uncontrolled [17]. In the United States, nearly a third of the population has high blood pressure, costing the country nearly $50 billion each year [18]. Uncontrolled hypertension can lead to kidney disease, blindness, stroke, and heart attack. Complications due to hypertension kill 9.4 million people per year [19]. People with prolonged hypertension are also at a higher risk of suffering from dementia and/or mild cognitive impairment [20], [21]. The lack of symptoms early on in hypertension has given rise to the nickname, 'the silent killer,' where often there is little warning before a severe event, such as a heart attack or stroke.

The percentage of people living with diabetes has nearly doubled in the last 35 years (estimated at 422 million in 2014) and is the direct cause of over 1.5 million deaths a year [1]. Type 2 diabetes, once only seen in adults, is now occurring at younger ages [22]. The longer a person has diabetes, the higher the likelihood of them having a complication, such as diabetic foot, kidney failure, diabetic retinopathy (DR), or heart attack [1]. From Fig. 1, the demographics show increases in every region of the world and every income group, although deaths related to high blood glucose disproportionally affect low-income regions. DR, a complication of diabetes, is also the leading cause of blindness in in working-age adults [23].

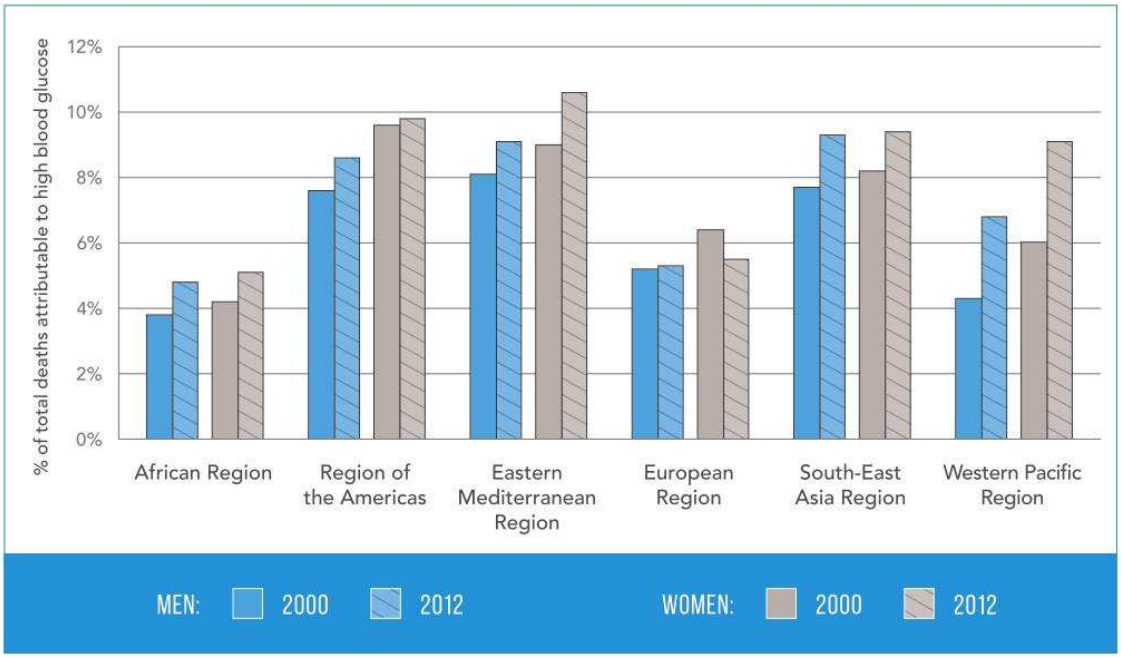

Figure 1.1 Percentage of all deaths attributed to high blood glucose aged 20-69, by region and sex [1]

The good news is that these two diseases can be controlled through treatment, lifestyle changes, and regular screening. At least some of the damage due to hypertension can be reversed (vascular narrowing[24]) and people can live longer with diabetes without the secondary complications [25], [26]. These factors also highlight the usefulness of retinal screening and tools for retinal vessel analysis. Changes in the retina due to diabetes occur many years after an initial diagnosis [27]. Regular screening can track changes and insure action is taken before vision

becomes impaired. Changes in the vasculature related to hypertension can be seen early on, possibly alerting a patient to the condition and tracking changes after facilitating treatment [28]. Many of the changes that occur in the retinal vasculature are difficult to quantitatively assess by a human. Ophthalmologists generally use qualitative metrics, such as high or low, that are difficult to track outside of a binary setting. Quantitative metrics are much simpler to produce and reproduce with the help of a computer and specially designed software. Retinal fundus cameras are a staple of the clinician's office and have been shown effective in patient screening as well as in a tele-retinal environment [29],[30]. The reasons for this are - they have a relatively low price point ($5000 - $20000 that has been dropping), are portable, easy to use and allow the viewing of multiple diseases. Combining retinal imaging with a framework for retinal vessel quantification gives the clinician a powerful tool in combating vision loss and tracking systemic diseases.

The University of Padova has created tools for the evaluation of the retinal vasculature; mainly a tool for calculating artery/vein (AV) ratio and tortuosity [31], [32]. We propose the combining of these tools with the addition of state-of-the-art algorithms in optic disc detection, tortuosity, and AV nicking (the main contributions of this work). These new tools, along with those previously created at the University allow for the accurate measurement of several of the most common vessel metrics used by clinicians today.

1.2. Research Objectives

This research aims to add to a retinal vasculature measurement framework, of which many steps have been previously developed. This framework includes many image processing steps before a vascular measurement can be taken. Generally these steps include preprocessing, optic disc (OD) detection, vessel segmentation and key point detection (cross-over, bifurcation and end points). The outputs of these steps are used to quantify several of the known vessel parameters affected by disease, such as vessel narrowing, AV nicking, AV ratio and tortuosity. The contributions of this work address three areas within this framework with new and state-of-the-art algorithms for: 1)

automatic detection of the optic disc, 2) computer-aided measurement of AV nicking signs, and 3) curvature enhancement for tortuosity estimation.

1.2.1. Optic disc detection

In this work, our main goal is the accurate detection of the optic disc in fundus images. In many algorithms, optic disc detection is usually a first step. This occurs for several reasons: 1) the subsequent processing is to focus on that area (such as in glaucoma, papilledema or AV ratio calculation), 2) one wants to mask this region from subsequent processing due to its brightness and contrast and 3) to take advantage of its geometric properties with respect to other landmarks in the image. Many methods have been developed for this task that take into account several of the obvious features of the OD. In general, it is the brightest region of the retina, has a circular to oval shape and is the entry point for the vascular tree into the retina. These properties would seem to make its detection trivial. However, any amount of disease, less than perfect image quality or normal variants can make this a challenging problem. Over the years, retinal imaging has improved in terms of image quality, field of view and resolution, and these quality images can generally be taken without the need of pupil dilation [33](This can still be difficult for patients with small pupils, the elderly and those with a central cataract [34]). Imaging standards have also been adopted for disease screening that have normalized the imaging process in terms of the field of view covered [35], and picture archival and communication systems (PACS) have made the storing of large amounts of patient imaging data a safe and simple process [36]. With all of these advancements, we felt that a new, accurate algorithm for optic disc detection would be an improvement to those proposed in the literature and contribute greatly to the performance of the vessel analysis framework.

1.2.2. Arteriovenous nicking measurement

The advancements in retinal imaging have also led to our ability to quantify vessel abnormalities that were previously unavailable. This includes arteriovenous nicking, where low contrast and low

resolution in the small areas of occurrence, made meaningful quantitative analysis impossible. Arteriovenous nicking (AVN) occurs when an artery, under a prolonged state of high blood pressure, pushes down on a vein at a crossing point. The exact cause is still speculation, but this can cause the vein to taper at the crossing and/or be displaced, entering and exiting the crossover at a right angle. These abnormalities, named after famous ophthalmologists from the early 1900's, are known as the (Marcus) Gunn and (Robert) Salus signs respectively [37][38]. AVN is an important sign in hypertension and hypertensive retinopathy due to its correlation with branch retinal vein occlusions (BRVO), where blood supply can be lost to an entire hemisphere of the retina [39]. Assessment of AVN is typically done in a qualitative manner by a human grader as a binary marker. Automated measurement of these AVN signs allows for a more accurate assessment of severity, leading to a less subjective grading standard and adding an important tool to the vessel analysis framework.

1.2.3. Tortuosity estimation

Tortuosity in the retina is the abnormal curving of the vessels. Generally, the vessels run in a straight parabolic arc, branching and splitting to cover the retina. While a subset of people have normally tortuous vessels (known as familial tortuosity [40]), it is generally a sign that the vessel is under a state of high pressure and has changed course to adapt. Tortuosity is one of the earliest signs of hypertension in the vessels and its severity is directly correlated to the hypertensive state [41]. Given this fact, measuring and tracking of tortuosity over multiple visits has become a popular method of tracking patient compliance with medication and lifestyle changes. Over the years, there have been many formulas used to define tortuosity at the vessel level and many combinational approaches to give an image level grade for tortuosity. The underlying issue, however, is that the human grader does not have a way to quantitatively measure the tortuosity they are seeing in the image. Grades are generally given as low, medium, or high (or 0 -2) and low inter and intra grader variability make standardization a difficult task [41]. Since these

mathematical tortuosity measurements are being correlated with the human grader qualitative measurements, it becomes difficult to tell which tortuosity metric is the most effective and makes the case for a more adaptable approach to tortuosity quantification.

1.3. **Thesis Contribution**

The main contributions of this thesis are three new, state-of-the-art algorithms developed as part of a retinal vessel analysis framework to address the problems mentioned in the previous section. An example image showing the areas of interest for this thesis can be seen in Fig. 1.2. Details for each of these contributions are outlined in the following sections.

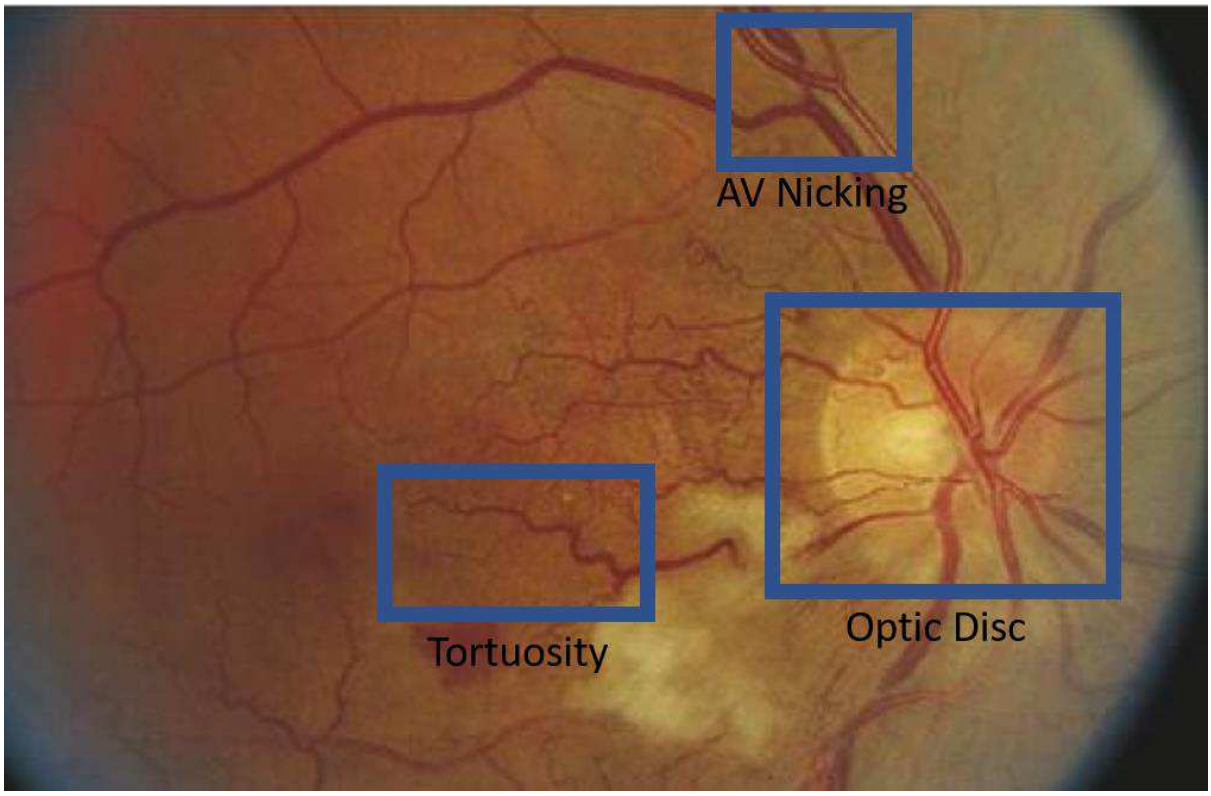

Figure 1.2 Visualization of the main landmarks and vessel abnormalities covered in this thesis. They include optic disc detection, tortuosity estimation and AV nicking quantification. Image adapted from [2].

1.3.1. **Optic disc detection**

We have proposed a novel method for the accurate detection of the optic disc in fundus images. The method converts the image to a graph, with vertices being all pixels in the foreground of the image and uses vessel enhancement techniques to calculate edge weights between these vertices. The shortest distance between 8 points on the periphery of the image to mirrored points on the other side are calculated. Each path generally follows the major vessels, which originate at the optic disc. The number of paths that cross each vertex is calculated, with the segment covering the maximum number of shortest paths being considered the area of interest for the optic disc. To ensure a precise location, a multi-feature template matching approach is used in this region and the maximum response is considered to optic disc. If certain thresholds are not met with respect to correlation and maximum path number, an iterative approach is used to expand the area of interest or ultimately determine that the OD was not found. The method was tested on three publicly available datasets: DRIVE [42], DIARETDB1 [10], and Messidor [43] consisting of 40, 89, and 1200 images and achieved an accuracy of 100, 98.88, and 99.42% on databases respectively. The method performs as well or better than state-of-the-art methods on these datasets, with processing taking an average of 32 seconds (+-1.2) to detect the optic disc, with the bulk of the time used for the vessel enhancement process. The accuracy over a wide variety of images shows that the method is robust and would be optimal in a retinal vessel analysis system, as it combines steps for vessel segmentation and OD localization.

1.3.2. Arteriovenous nicking measurement

An efficient method for calculating the signs associated with AVN is proposed in this work. Using information provided as to the location of the crossovers, either from the vessel framework or as a semiautomatic user input, the method combines segmentation, artery vein classification, and morphological feature extraction techniques to calculate vein widths and angles entering and exiting the crossover for the calculation of both the Gunn and Salus signs. First, a region of interest around the selected crossover is cropped from the original image. The vessels are then segmented

using the method introduced by Frangi [44]. The four corners of the crossing are detected and used to create a bounding box to separate the four vessel segments. Color and intensity profiles are used to determine artery from vein. Vessel widths are detected using monodimensional matched filtering perpendicularly along the vessel axis. This gives all the information needed to calculate the Gunn and Salus signs. The method was tested on a small set of crossings (5 normal, 5 abnormal), graded by a set of 3 doctors who were in agreement as having or not having Gunn/Salus sign. Results show separation between the two classes and that we can reliably detect and quantify these signs under these higher quality imaging conditions. We then tested the method on a publicly available dataset [45],[46](32 normal crossings, 31 showing signs of AV nicking at different levels). The results further corroborated our findings, showing the ability to separate normal crossings from abnormal.

1.3.3. Tortuosity Estimation

First, we develop a new dataset for tortuosity estimation based on the grading of 5 doctors. The most common methods for tortuosity estimation are tested on this dataset to compare with other studies on the efficacy of each method. We then propose a new method for enhancing curvature as a feature for calculating tortuosity, based on a difference of Gabor filters, which can be used on a segmented vessel or vessel skeleton. The rationale for using different sets of Gabor filterbanks is in their response at curves. The difference in Gabor filters comes from the aspect ratio used in the Gaussian envelope; elongated envelopes will have different responses at curvature points along the vessel compared to rounder envelopes, when other factors are normalized. This difference between the maximum responses of the two filterbanks gives a higher response at regions of curvature. This, along with the other variables associated with Gabor filters allows for the tuning of these filters to emphasize different wavelengths of curves, thought to be important to a clinician making a tortuosity assessment. The curvature-enhanced image can be combined with the typical mathematical calculations for tortuosity to provide a tortuosity score

that can be optimized based on the grader. The proposed method was tested on the RET-TORT database using several methods to calculate tortuosity, and had a Pearson's correlation coefficient of .91 for arteries and .82 for veins. However, since we allow for the customization of the filter banks, using different parameters for arteries and for veins yielded the best results of .94 and .88 correlation coefficients respectively, outperforming the best rigid methods for tortuosity estimation on this database. The proposed method was then tested on the newly developed dataset and had higher correlation values across both graders and vessel types than any of the standard metrics used for tortuosity estimation.

1.4. Thesis Organization

The rest of the thesis is organized as follows:

Chapter 2: Research Background

The chapter presents the relevant background knowledge for this research. First, the anatomy of the retina is presented followed by a review of some of the retinal imaging technologies that allow our analysis. Then a review of the relevant pathologies associated with hypertension and diabetes with respect to the retina are covered. We then present a review on the steps in a typical vessel analysis framework and conclude with an in depth literature review of relevant methods associated with optic disc detection, tortuosity and arteriovenous nicking.

Chapter 3: Optic Disc Detection

This chapter presents an automatic method for the detection of the optic disc (OD). A novel approach that treats the image as a graph and calculates the shortest path between points on the periphery of the image using a vessel enhancement as weights, is proposed. This method uses the fact that the retinal vessels originate at the OD, and since shortest paths will follow along the major vessel paths, the largest accumulation of shortest paths will be in the area of the OD. The method is tested on several of the well-known, publicly available datasets including DIARETDB1, Messidor, and DRIVE, achieving equal or better results than state-of-the-art algorithms. A true

OD location was considered anything inside the OD. Overall, the method is tested on 1456 retinal images and achieves an average accuracy of 99.45%.

Chapter 4: Arteriovenous nicking quantification

This chapter presents a novel method for quantifying the signs related to arteriovenous nicking (AVN). AVN is clinical marker in hypertensive retinopathy and its association with sight threatening events makes the accurate quantification of AV crossings an important tool for vessel quantification. There are two distinct phenomena that can occur due to AVN. A visual tapering of the vein going into and coming out of the crossing, known as the Gunn sign. Also, the displacement of the vein at the crossing, visualized as a 90° change of path at the crossing, known as the Salus sign. This work presents a method for the automatic quantification of these two signs once a crossover has been detected; combining segmentation, artery vein classification, and morphological feature extraction techniques to calculate vein widths and angles entering and exiting the crossover. The method was tested on two datasets: A small dataset of 10 crossings, graded by a set of 3 doctors who were in agreement as having or not having Gunn/Salus sign, and again on a larger publicly available dataset (63 crossings grading from 0-3). The method shows the ability to separate the normal and abnormal crossings in agreement with the ground truth.

Chapter 5: Tortuosity estimation

This chapter presents a comparison of many of the popular tortuosity metrics as well as a novel method for curvature enhancement along with several methods for using this information in creating new, adaptable tortuosity metrics. The proposed method uses the difference of Gabor filter banks whose aspect ratios are different. In general, this creates low filter responses in straighter region of vessel segmentations and higher responses at curves, with respect the Gabor filter bank chosen. The method was tested on dilated vessel centerlines recreated from the RET-TORT dataset; a set of 30 arteries and 30 veins with ordered gradings by two clinicians. The method achieves a highest rank correlation of .94 for arteries and .88 for veins, exceeding results from the general mathematical formulations for tortuosity. The method was then tested on the

newly developed dataset, producing higher correlation values than the standard metrics across vessel type and grader.

Chapter 6: Retinal Vessel Measurement Framework

This chapter combines the methods developed in the previous chapters with algorithms developed in the past at the University of Padova into a vessel measurement framework. Pulling from previously developed semiautomatic tools, this chapters goes through the process of measuring the important features related to vascular disease, including user input for fixing the optic disc location and vessel tree segments. Vessel width, multiple tortuosity metrics, AV ratio and crossover analysis can all be measured through this framework. A look at other available systems for vessel measurement are also presented.

Chapter 7: Conclusions and Future Work

This chapter presents the vessel analysis framework with the new algorithms added to the system. A summary of the contributions from the previous sections are presented as well as a discussion of the possibilities for future work in this area.

Chapter 2
Research Background

The chapter presents the relevant background knowledge for this research. First, the anatomy of the retina is presented followed by a review of some of the retinal imaging technologies that allow our analysis. Then a review of the relevant pathologies associated with hypertension and diabetes with respect to the retina are covered. We then present the typical vessel analysis framework and conclude with a literature review of relevant methods associated with optic disc detection, tortuosity and arteriovenous nicking.

2.1 Introduction

The retina is an extension of the central nervous system [47]. It is connected to the brain through the optic nerve and has the main duty of translating the many frequencies of light into nerve signals that our brain then interprets into what we see. The retina is made up of roughly 10 layers, including three made up of nerve-cell bodies and two containing synapses [48]. The inner limiting membrane (the inner most layer) separates the retina from the vitreous, and the outermost layer, the retinal pigment epithelium (RPE), forms a blood barrier with the choroid (a vessel rich layer that supplies the outer retina) and is just behind the layer of photoreceptors [48]. Fig. 2.1 shows these layers. The retinal layers seem to be reversed from conventional think. Light

is captured by light receptors at the back of the retina as opposed to the front, travelling through the many layers of nerve cells and synapses before being captured. The RPE cells contains melanin, which absorbs light passing through the retina so that it does not reflect and scatter inside the eye [49]. Proteins in the photoreceptors absorb photons and begin the process of photo-transduction (conversion of light to electrical signals) [50]. Information is passed up to the middle layers of the retina containing three types of nerve cells for processing. Horizontal cells link photoreceptors to bipolar cells and amacrine cells link the bipolar cells to the outer layer of ganglion cells. The ganglion cells then pass the information across the retina to the optic nerve and are then sent to the brain. These cell connections can be visualized in Fig. 2.2. There are two types of photoreceptors collecting light information; rods which are more sensitive to light and are primarily responsible for our low light vision and cones which make up the bulk of our color and fine vision [51]. Cones can be further broken to down into the frequency of light they are most sensitive to, which in terms of color are red, green and blue. Their sensitivities do overlap, which allows cones to work in combination so that we can see the entire array of visible colors [52]. Rods outnumber cones in the retina approximately 120 million to 6 million, and both are disproportional spread across the retina as we will see later.

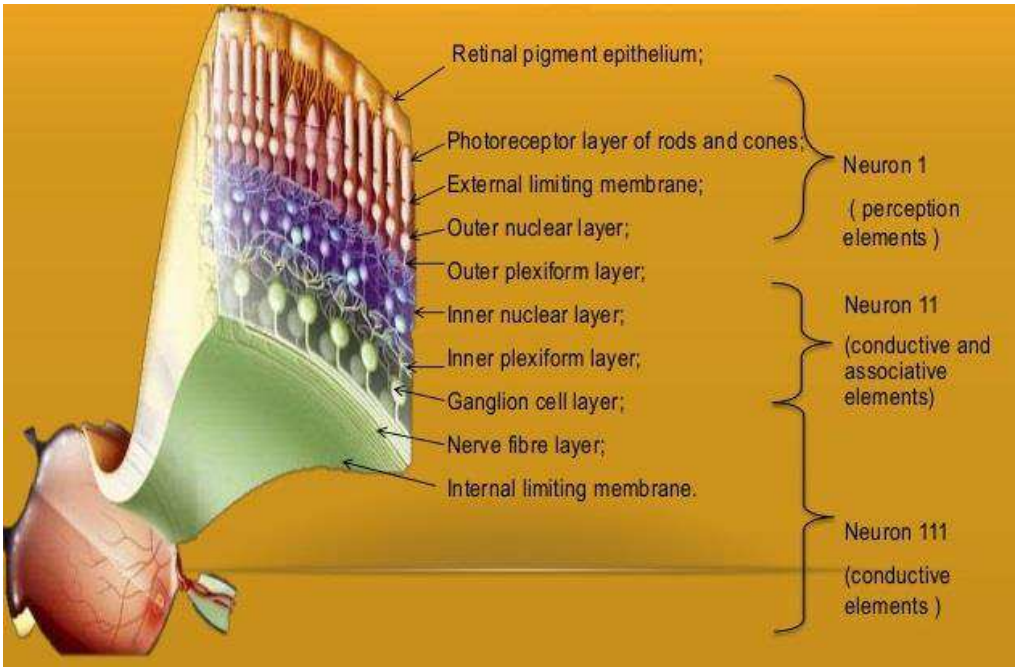

Figure 2.1 The layers of the retina from the retinal pigment epithelium to the internal limiting membrane. Image from [3].

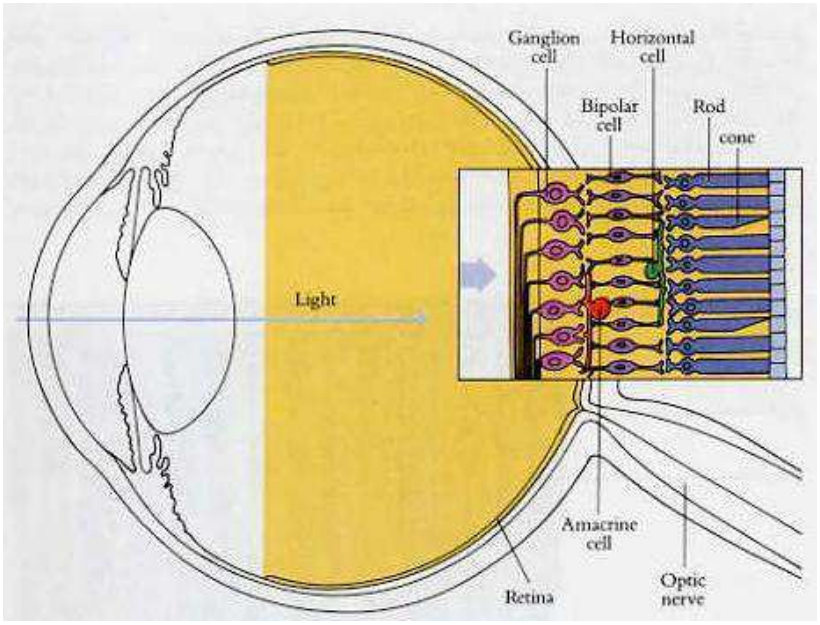

Figure 2.2 Connections shown between the Rods and cones, bipolar and ganglion cells. Light passes through these first layers of cells to the rods, cones and RPE. The information is converted to a biological message and then into an electrical impulse that is sent to the brain via the network of ganglion cells. Image from [53].

The retina covers approximately 75% of the inner eye wall. It can be broken down into several separate distinguishing features as shown in Fig 2.3. The macula lutae is an ovalish pigmented area near the center of the retina. The dense pigmentation in this region helps to reduce the

scatter of light and is a dense location of cones [54]. It is also important because at the center of this region is the fovea, an avascular region where our central vision comes from. This region has the highest concentration of cones in the retina (200,000 – 300,000 cones/mm) and has a central depression. Displacement of the neuronal layers and lack of vasculature leaves direct access to the photoreceptor layer [55]. When we look at an object, this is where we fixate that object on the retina for our clearest vision. When there is disease in this area of the retina, there is a large chance that vision will be impaired.

The optic nerve head (disc) is probably the most distinguishing feature of the retina. It does not have the same layers as the rest of the retina, containing only the nerve fiber layer and the internal limiting membrane. This accounts for the pale appearance as there is no RPE with the dark melanin to absorb light. There are no photoreceptors in this region which makes it our natural blind spot [56]. This is also the region where all of the ganglion cell axons converge and exit the eye through the optic nerve to the brain. The average optic disc is an oval with a major axis of approximately 1.8mm and minor axis of 1.5mm [57]. It shares a geometric relation with the fovea, generally being located 3 to 4mm to its nasal side. The optic disc is also the entry point for the main retinal vessels, the central retinal artery and vein. As can be seen in Fig. 2.3, the vessel arcades leave vertically from the optic disc before curving into a parabolic shape around the macula. The central retinal artery supplies 20-30% of the blood flow to the retina (the choroid supplies a much greater portion 65 – 85%), breaking off into four main branches to cover the retina and feed oxygenated blood to the capillary networks [58]. The central retinal vein then drains these capillaries and sends the deoxygenated blood back toward the heart. The lack of oxygen in the blood accounts for the darker appearance of the veins in fundus images. Some standard key points are generally identified in the vessels are:

Branching points – a branch point is the point where a smaller vessel comes out of a larger vessel.

Bifurcation points - a bifurcation point is when a vessel splits into two equally sized vessels.

Crossover points – a crossover points is when an artery crosses a vein or a vein crosses an artery.

These points make the analysis of the retinal vasculature much easier for a computer since the vessels can be broken down into common segments where widths can be compared and the vascular trees can be separated.

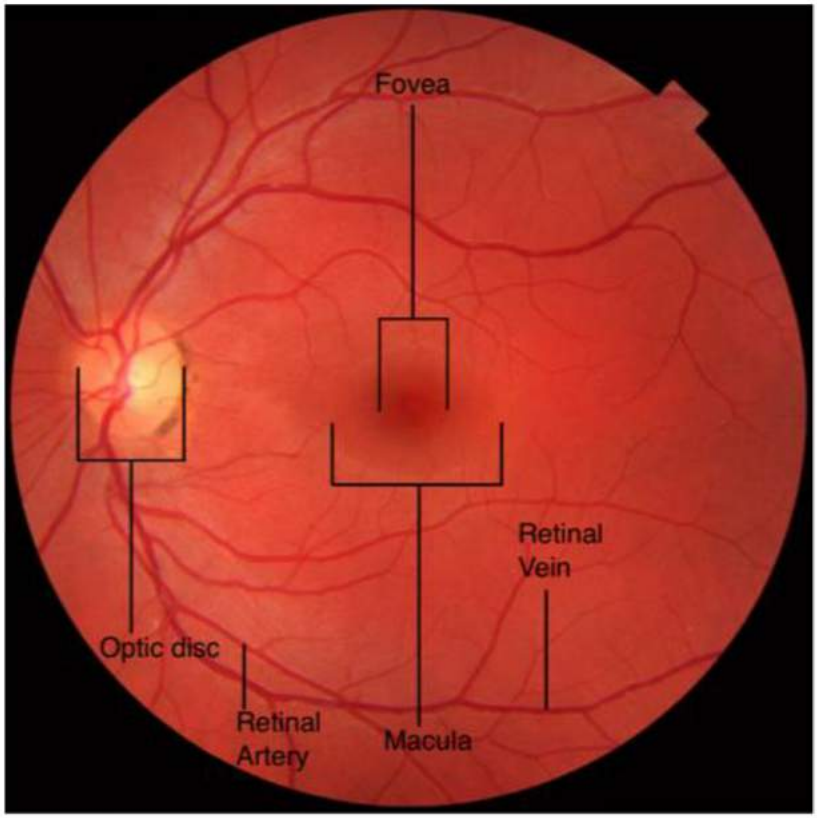

Figure 2.3 A fundus photograph depicting the main features of the retina including the optic disc, fovea and main retinal arcades, adapted from [4].

2.2 Imaging Technologies

Through the years, many methods have been developed for the imaging of the retina and its layers. These methods include direct fundus photography, angiography, confocal scanning laser ophthalmoscopy and optical coherence tomography. Each method, including pros and cons is listed and briefly described in the following sections.

2.2.1 Fundus photography

Fundus photography, or color fundus retinal photography, is the combination of a microscope and a normal camera back for imaging the retina (as shown in Fig. 2.4). Light is shown into the eye

and the magnified image is captured. Generally there is a fixation point for the patient to follow to capture different fields of view. This can be done with or without pupil dilation. Pupil dilation generally provides higher quality images and can allow for a larger imaging area. Fundus photography has many advantages: it is non-invasive, inexpensive, comfortable and the cameras are easy to operate (automatic cameras are also available [59], [60]). They allow for clear viewing of all the major retinal landmarks and have especially good contrast with blood, making them ideal for vascular measurement and abnormalities. There are of course drawbacks to a two-dimensional image of a three dimensional object. The biggest being a lack of depth. Several sight threatening diseases require some depth perception in the macula and optic disc. The closest thing to depth that can be achieved is by taking multiple images from slightly different angles and combing the information to get depth from disparity, much in the way our eyes combine information [61].

Figure 2.4 Typical fundus camera setup with camera back and digital interface. This particular model is a KOWA nonmydriatic 7 with VK-2 digital imaging system from [5].

2.2.2 Angiography and autofluorescence

Angiography is used to visualize the insides of vessels in the body. To do this a contrast medium is injected into the patient. For the retinal vessels, this is typical fluorescein and for the choroid, it is indocyanine green. As the dye passes through the blood vessels in the eye, a camera equipped

with special filters can image the blood flow [62]. This has the ability to show the arterial and venous networks separately (since the blood will be passes through them at different times) and show any leaking that may be occurring in the vessel network (as shown in Fig. 2.5). While this is an excellent way to visualize the vascular network, it requires the invasive step of injecting the dye. More recently, autofluorescence has been used, taking advantage of the fluorescent properties of pigments in the retina [63].

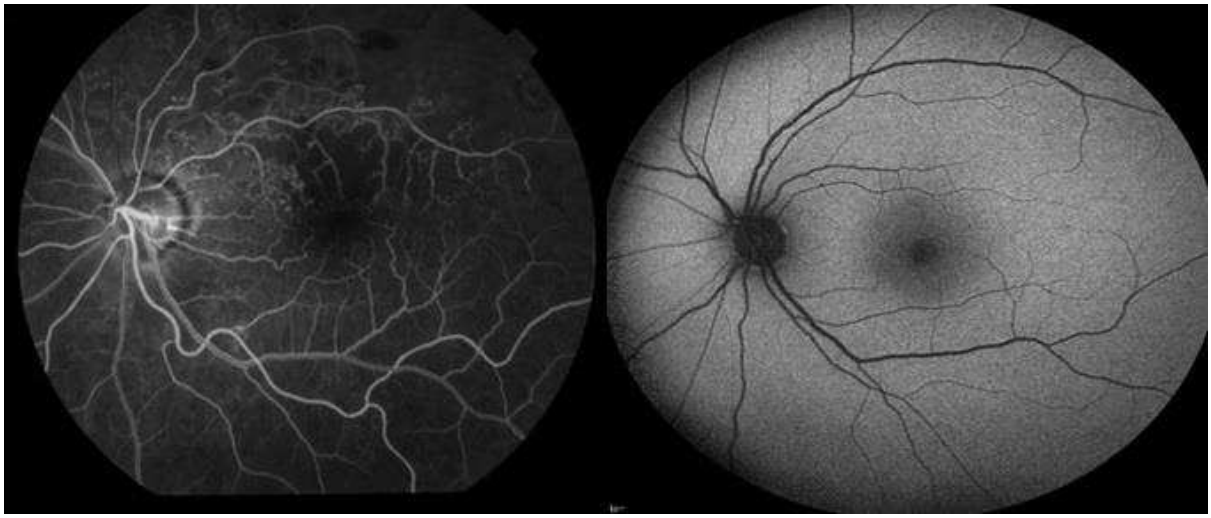

Figure 2.5 Left image: Image of the vessel network with leakage taken with fluorescein angiography. Right Image: Autofluorescence image of the retina. Images from [6]*,* [7] *respectively.*

2.2.3 Confocal scanning laser ophthalmoscopy (cSLO)

This technique uses a laser beam to scan across the retina in a raster pattern. The light reflected from each point is multiplied and recorded. Confocal means that the detection takes place through a focal point, eliminating light reflected from outside the spot illuminated by the laser [64]. This creates a retinal image that can have a very high spatial resolution. The depth of the laser can also be adjusted to capture different layers of the retina as well as provide depths maps of the optic disc or macula. Also, since the laser enter the eye as a pinpoint, it provides for the ability to generate much larger field of view images. Ultra-widefield has now become its own subsection of SLO imaging (up to 200° field of view which can be seen in Fig. 6) [8],[65]. Of course,

this can produce its own problems, since scanning that far into the periphery can create geometric artifacts due to the disparity of depth in the images. This can partially be corrected with software and the method allows for the possible viewing of disease in the periphery that would go unnoticed until it made its way to the central retinal area. Previously, the size and cost of these machines was burdensome outside the major hospital setting, but both have come down considerably in the last ten years [66].

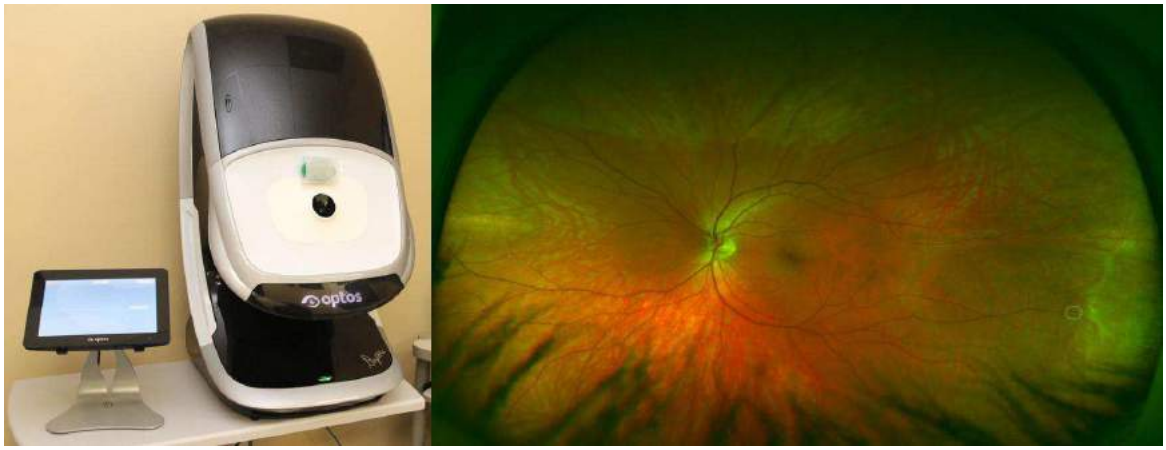

Figure 2.6 Left Image: An optos, ultra-widefield system. Right Image: An ultra-widefield image from this system [8].

1.2.4 Optical coherence tomography (OCT)

The main idea of OCT is to compare the difference of flight times of light waves when sent into a biological media with that of a reference signal, similar to ultrasound (but with light waves) [67]. This can be done at a single point (A-scan), a line of points to get a cross section view (B-Scan), or done over an entire area (x and y directions 3D volumetric view). Each layer of the retina can be visualized, as seen in Fig. 2.7, and has become the standard for detecting many of the sight threatening retinal diseases. There are now multiple methods for OCT, including the more recent spectral domain (SD-OCT) and swept source (SS-OCT, subset of SD-OCT) methods to accompany the original time domain (TD-OCT) method. These newer methods improved upon the signal to noise ratio and acquisition time by measuring the spectrum of the output which can be captured for an entire B-scan all at the same time. The drawback is losing some of the sensitivity along the

axial range of the scan, whereas the sensitivity is constant in TD-OCT [68]. One of the few drawbacks of these methods is the inability to discern blood reliably, a key factor in blood vessel analysis.

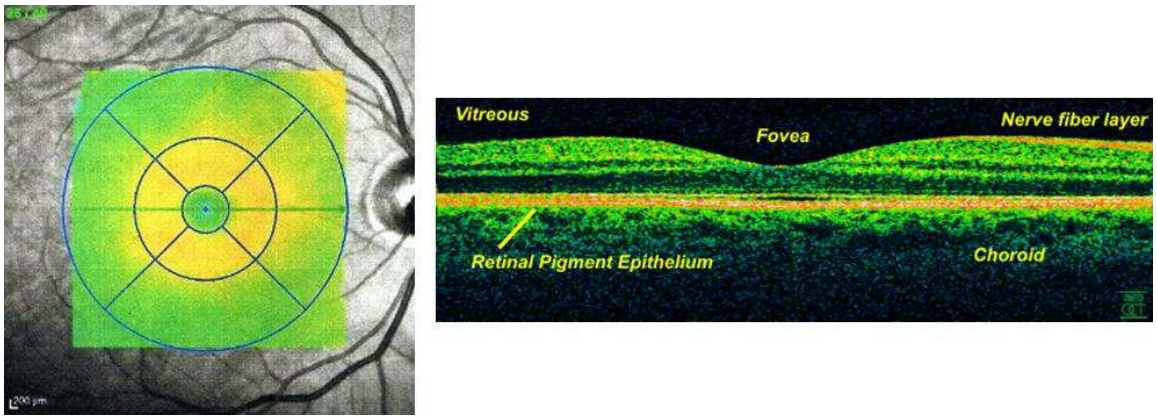

Figure 2.7 Examples of OCT images. Left: Overlay showing the region of interest covered with green arrow across the fovea denoting B-scan location and Right: A B scan through the fovea showing the individual layers and depth in the region. Images adapted from [9].

Due to the nature of this study with an emphasis on the retinal vasculature, fundus photography is used to make all measurements. The combination of high blood vessel contrast, medium resolution, wealth of data, cost effectiveness and noninvasive nature make it just as relevant today as it was 40 years ago, even without any major breakthroughs along the way. While generally not used to diagnose, in many clinics it is one of the first procedures undergone before determining if other procedures are necessary. Studies have also shown that fundus photography is very useful in the monitoring and screening of disease [29], [30]. These cameras can be taken to remote locations to screen underserved populations. Images can be read online or with the help of automated software and recommendations can be made for follow up exams. Temporal images can track the course of disease and determine patient compliance and the effect of medication or determine when future intervention will be necessary [69].

2.3 Retinal Pathologies

Hypertension and Diabetes effect the retina in different ways. Their effect, along with those from other diseases, are known as retinal pathologies. Generally with these two disease, vision loss becomes a factor when the pathologies are in the area of the macula and fovea. Pathology in the periphery can go unnoticed visually but serves as a warning of future vision loss and damage that may be occurring in other parts of the body. A description of both hypertensive and diabetic retinopathy is discussed in the following sections starting with a brief description at the biological level and moving on to the presentation in retinal images.

2.3.1 Diabetic retinopathy

Diabetic retinopathy (DR) occurs as a complication of diabetes due to damage of the blood vessels by high sugar levels. Early on, arteries begin to narrow and blood flow to the retina is reduced. The opposite then occurs as the disease progresses [70], [71]. At the cellular level, pericytes, which provide vascular stability and control endothelial proliferation, are damaged and/or lost. This can lead to blood leakage from the destabilized capillary bed [72]. In response, the retina either increases it vascular permeability, which can lead to swelling, or can form new, weak vessels that can grow out into the vitreous and possibly leak. There are several categories of DR which can be broken down into the following manner:

Non-proliferative diabetic retinopathy (NPDR) - this stage is characterized by the formation of lesions on the retina. These lesions include microaneurysms, hemorrhages, hard exudates (lipid residue left over from a serious leak) all caused by the leaking capillary bed due to the previously mentioned vessel breakdown. Other lesions include cotton wool spots, which are abnormalities in the nerve fiber layer caused by swelling. This category can be broken down further based on the number, type and location of lesions present as mild moderate and severe as shown in Table 1.

Proliferative diabetic retinopathy - this stage is marked by the growth of new vessels. Vascular endothelial growth factor (VEGF) protein expression is elevated, stimulating the growth of new, small and weak vessels. These vessels are able to grow into the vitreous where they are prone to

leak [73]. These new vessels are given a different name depending on their location in the retina. If they are on the optic disc, they are known as neovascularization of the disc (NVD), and known as neovascularization elsewhere (NVE) on the rest of the retina.

Macular Edema – separately, swelling of the macula caused by the leakage of fluid is known as macular edema. This can occur in conjunction with the other categories of DR, but immediately raises the severity, as vision is generally affected due to the region it effects [74]. Exudates in the macula are a sign of either present or previous edema in the region and are used to determine the presence when depth imaging methods (such as OCT) are unavailable.

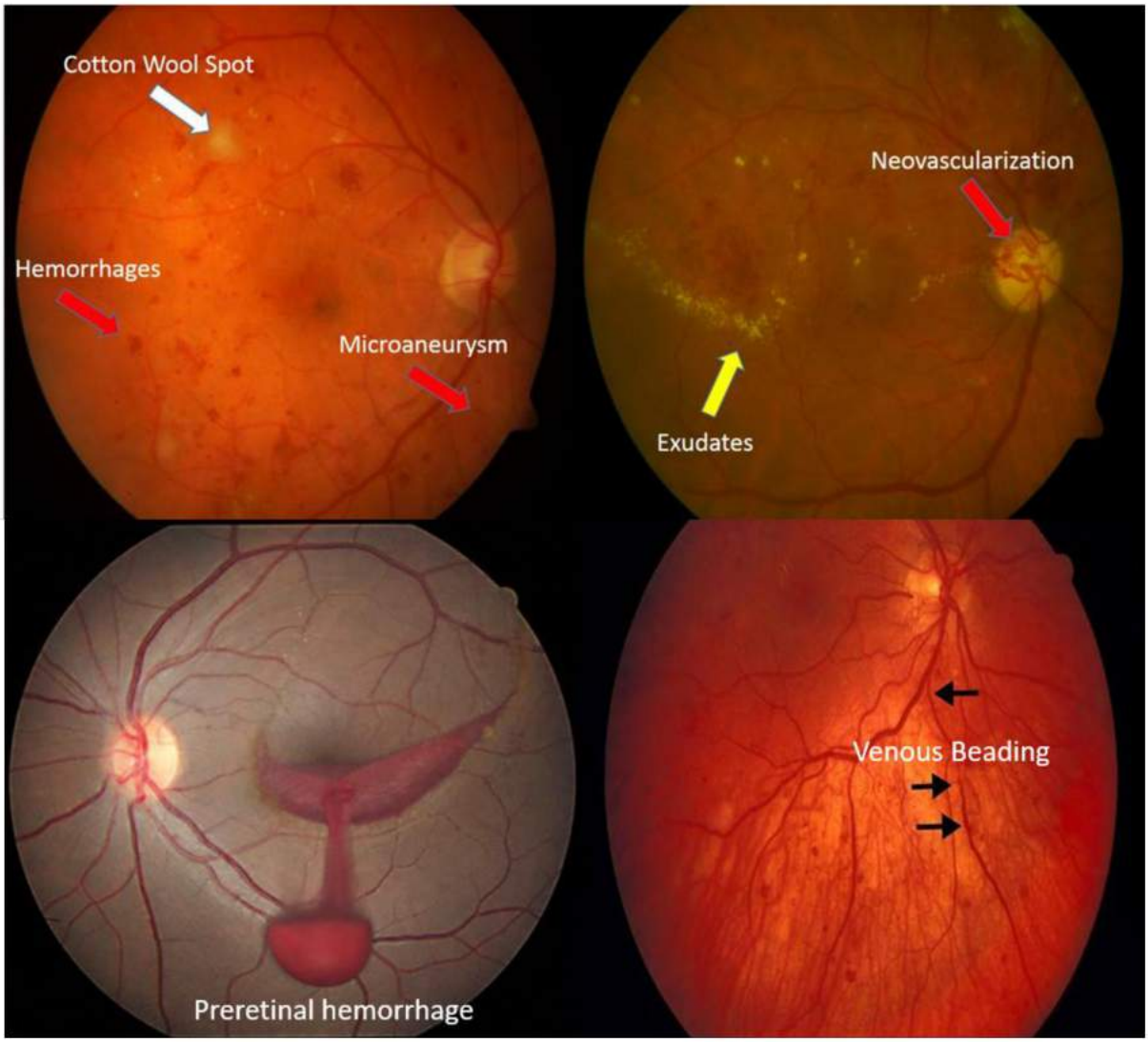

Figure 2.8 Images depicting some of the common lesions and abnormalities present in diabetic retinopathy. They include exudates, microaneurysms, hemorrhages, cotton wool spots, venous

beading, preretinal hemorrhage and neovascularization at the disc. Exudates in the macula denote past or present edema. Images adapted from DIARETDB1 [10].

Table 2.1: Levels of DR proposed by Wilkinson et al. [15] *breaking down the type, number and quadrant of pathologies.*

Proposed Disease Severity Level	Findings Observable on Dilated Ophthalmoscopy
No apparent retinopathy	No abnormalities
Mild nonproliferative diabetic retinopathy	Microaneurysms only
Moderate nonproliferative diabetic retinopathy	More than just microaneurysms but less than severe nonproliferative diabetic retinopathy
Severe nonproliferative diabetic retinopathy	Any of the following: more than 20 intraretinal hemorrhages in each of 4 quadrants; definitive venous beading in 2+ quadrants; prominent intraretinal microvascular abnormalities 1+ quadrant; No signs of proliferative retinopathy
Proliferative diabetic retinopathy	One or more of the following: neovascularization, vitreous/preretinal hemorrhage.

2.3.2 Hypertensive retinopathy

Hypertensive retinopathy (HR) refers to the damage associated with the retinal vessels under prolonged elevated blood pressure. The pressure puts stress on the blood vessels, causing damage that can lead to a blockage or rupture as well as adaptive changes to the vessels themselves [75]. One of these adaptation is in the course of the vessel path, known as tortuosity. While mild tortuosity is relatively common in the general population, elevated levels are a clear indicator of disease. Many of the same lesions present in DR are also present in hypertensive retinopathy. It has historically been graded on scale (known as the Keith Wagener Barker scale) of 1 – 4, based on the type and severity of the signs [76]. Examples of many of the lesions and abnormalities associated with HR are presented in Fig. 2.9. Grade 1 (mild hypertension) signs include generalized arteriolar narrow and sclerosis (presents as a 'copper wiring effect' due to increased thickness of the vessel walls). Grade 2 signs include focal arteriolar narrowing (Fig. 2.9 A) and crossing abnormalities such as the Gunn and Salus signs (Fig. 2.9 B). There is also an

exaggerated light reflex along the arterioles. Grade 3 signs include exudates, hemorrhages, and cotton wool spots, similar the described in the previous section. Grade 4 signs are an increase in the grade 3 signs plus papilledema (optic disc swelling).

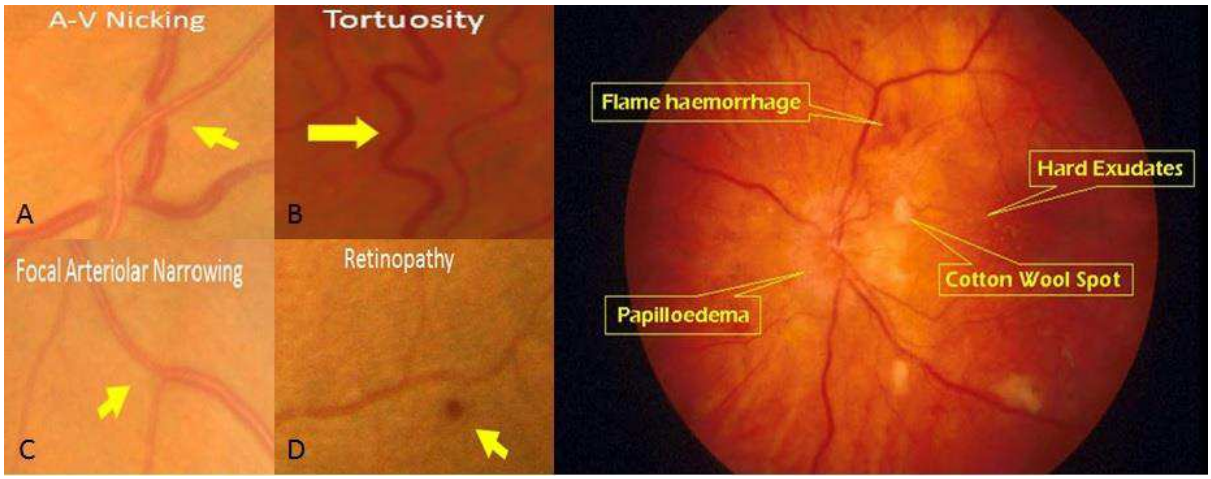

Figure 2.9: Signs associated with hypertensive retinopathy. (A) AV nicking showing both tapering and displacement of the vein. (B) A highly tortuous vessel. (C) Focal thinning of an artery. (D) A microaneurysm. (Right) Advanced lesions in DR including flame hemorrhages, hard exudates, cotton wool spots, and optic disc swelling. Images adapted from [11].

The two signs that are the focus of this work are tortuosity and cross over abnormalities. Tortuosity, or curving in the vessels, has been associated with both hypertensive retinopathy and DR (among other diseases). The underlying causes of tortuosity are not well understood, but it is thought that changes in blood pressure, weakening of the vessel wall, and axial tension may all play a part [77], [78]. Highly tortuous vessels can limit blood flow or occlude it all together, cutting off the blood supply to large parts of the retina. AV nicking occurs when an artery, under hypertensive conditions (sclerotic, stiff walls), pushes down on a vein at a crossing. The vein becomes pinched down at this point leading to lower blood flow and visual tapering of the vein at the crossing point. The pressure can also displace the vein at the crossing, changing the angle of vein at the crossing (Fig. 2.9 A).

2.4 Retinal Vessel Measurement Framework

In order to make computer based quantification of retinal vessel abnormalities, certain processing steps are generally followed. Although this thesis is only concerned with certain parts of this framework, an explanation of each step is provided along with popular methods of completing these tasks. An in depth literature review of the thesis topics is presented within this discussion. Fig. 2.10 shows a flow chart of a typical retinal vessel measurement framework. A retinal image typically undergoes preprocessing to increase contrast and even illumination. The optic disc region and vessels are segmented either individually, simultaneously or using joint information. This information is used to create a skeleton of the vessel network from which key points and vessel widths are found and used to help classify arteries and veins. Finally, with all of this information, the typical vessel metrics can be calculated.

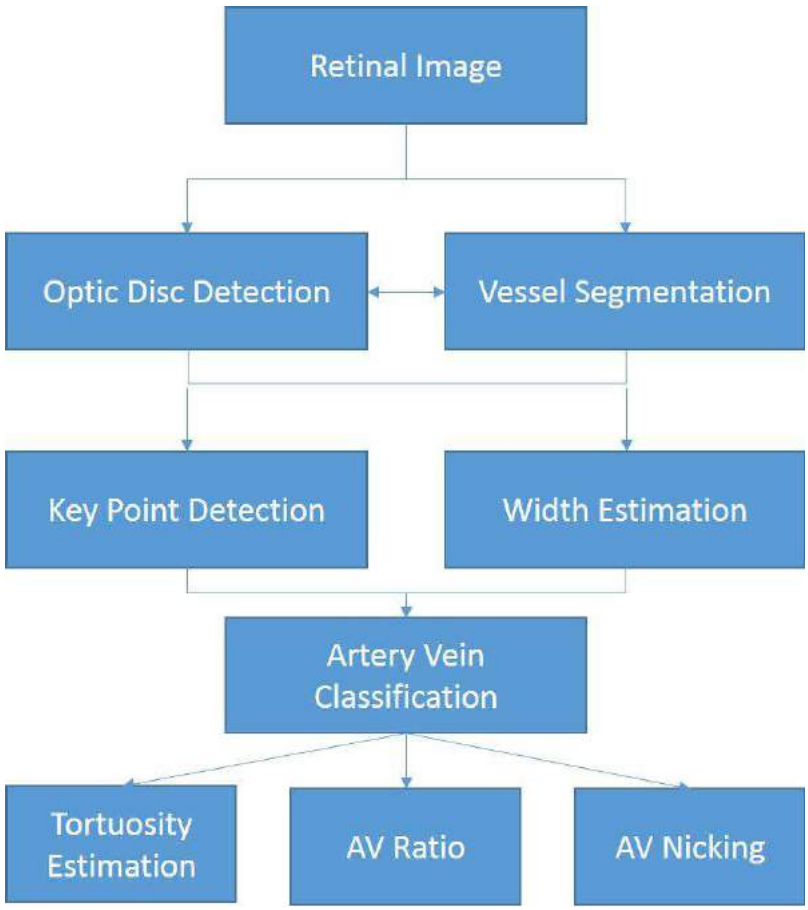

Figure 2.10: A typical flow chart for retinal vessel analysis. A retinal image is preprocessed and OD detection and/or vessel segmentation takes place. A skeleton of the vascular network is formed and key points and vessel widths are extracted. Artery/Vein classification is performed before the typical vessel metrics are calculated.

2.5 Literature Review

A literature review is presented of the main topics of this thesis. This includes methods for the detection of the optic disc, cross-over abnormality detection and tortuosity measurement.

2.5.1 Optic disc detection

There have been many methods proposed in the literature for optic disc detection. Normally, the OD presents as the brightest region in the image. However, retinopathies, image quality and normal variations can make this untrue, which makes OD localization a surprisingly difficult task that has led to many advanced methodologies. Some methods have focused just on OD detection, while others perform OD segmentation as well. A look at many of the popular and newer OD detection algorithms will now be discussed. For an in-depth look at earlier OD algorithms, please see Youssif et al. (2008) for an extensive review [79]. In 2003, Hoover and Goldbaum [80] used the fuzzy convergence of vessel end points from a vessel segmented image to determine the convergence of blood vessels and ultimately the OD location, obtaining an 89% detection rate on the STARE dataset. This dataset consists of 80 images with ground truth of highly diseased retinas. In 2004, Foracchia et al. [81] fit a parabolic model to the main arcades in the image, with the OD location being the area of convergence of all vessels. Based on this model, the OD location is able to be determine even if it is not present in the image. The method achieved a 98% detection rate when tested on the STARE dataset. Neimeijer, Abramoff, and Van Ginneken (2009) [82] used a k-nearest neighbor regressor with features from the original image and a vessel segmentation to predict the distance of each pixel in the image to the optic disc. The method achieved a 99.4% OD detection rate on an in-house dataset. Mahfouz et al. (2010) [83] encoded the x and y coordinates of the OD in 1-D projections based on certain retinal features. The method had a combined 97% detection rate on 4 publicly available datasets. Welfer et al. (2010) [84] used an adaptive morphological approach that prunes a skeletonized vessel segmentation until just the main arcades are present. The OD is localized using the intersection of the centroid of the

skeleton and the remaining vessel arcade fragment. The method obtained 100% and 97.75% detection rates on the DRIVE and DIARETDB1 databases. Aquino et al. (2010) [85] combined three methods for OD detection (maximum difference, maximum variance, and a low-pass filtering method) into a voting procedure based on the location found in each method. The method obtained a 99% detection rate in the Messidor database. Qureshi et al. (2012) [86] also combined OD detection algorithms using geometric rules. The methods include pyramidal decomposition, edge detection, entropy, Hough transform, and feature vector combination and achieved a 100% and 94.02% on the DRIVE and DIARETDB1 databases respectively. Yu et al. (2013) [87] used adaptive template matching to determine OD candidates and the final OD location was determined from the vessel characteristics in these regions. The method achieved a 99.08 detection rate on the Messidor dataset. Pereira et al. (2013) [88] used an ant colony optimization algorithm which mimics swarm behavior as the ants move based on local intensity variation and achieved a 93.25% detection rate on the DIARETDB1 database. Yu, Ma and Li (2015) [89] employed a morphological approach on a combination of intensity and vessel convergence information and achieved a 99.52% detection rate on several publicly available datasets. Rahebi et al. (2016) [90] detected the OD location using the firefly algorithm. The algorithm compares fireflies, moving the insects based on intensity values in the image until an optimal insect is found as the OD location. The method achieved a 100% and 94.38% detection rate in the DRIVE and DIARETDB1 databases. Abdullah et al. (2016) [91] used the circular Hough transform after morphologically removing the vessels from a preprocessed image to determine the OD location.

2.5.2 Vessel segmentation

Methods for retinal vessel segmentation can generally be broken down into two main classes: supervised and unsupervised, being broken down further by the underlying methods (matched filtering, vessel tracking, multiscale approaches and model based). Many works have been developed in each of these categories, but we will focus on the more recent and popular methods

in supervised and unsupervised with a brief discussion on the subcategories. For an in depth review on all methods, please see Fraz et al. [92].

Supervised methods require a training set with manually annotated ground truth to learn the rules of extraction from the features provided. While generally offering better classification results, they may be limited by the availability of ground truth data or the quality of said data. Staal et al. (2004) [42] presented a ridge-based vessel segmentation combined with a k-nearest neighbor (knn) classifier to separate vessel pixels from the background. Niemeijer et al. (2004) [93] also used a knn classifier in conjunction with multiscale Gaussian matched filters to create a vessel probability map which is then thresholded to achieve the final segmentation. Soares et al. (2006) [94] used the response on 2D multiscale Gabor wavelets paired with a Bayesian classifier to segment the vessels. Ricci and Perfetti (2007) [95] used the response from a series of line operators with a linear support vector machine (SVM) classifier. They added a small orthogonal component to their lines, which made them more robust in vessel detection. Osareh and Shadagar (2009) [96] used multiscale Gabor filters and a Gaussian mixture model (GMM)/ SVM classification system to detect vessels. Xu and Luo (2010) used adaptive local thresholding to find candidate vessels, which are then classified using SVM. Marin et al. (20011) [97] used gray level and moment invariant features fed to a neural network (NN) for vessel pixel classification.

Unsupervised methods attempt to classify vessels without the input of ground truth. They look for patterns in data that allows for the separation of classes. Salem et al. (2007) used the radius based clustering algorithm along with partial supervision to segment blood vessels. Bhuiyan et al. (2007) [98] use a bank of Gabor filters to describe texture features in the image and a fuzzy-c means clustering for classification. Kande et al. (2009) [99] used illumination correction and matched filter responses with a spatially weighted fuzzy-c means clustering to threshold the vasculature. Ng et al. (2010) [100] proposed using the maximum likelihood of scale space parameters to a vessel model based on a Gaussian profile. Bankhead et al. (2012) [45] proposed

the use of the wavelet transform as vessel enhancement which is then thresholded to get a preliminary segmentation, which is then refined through a gradient analysis.

Other methods for vessel segmentation include those related to matched filters, vessel tracking and multiscale approaches. Some of the methods have been used in conjunction with classifiers as seen in the previous sections. A quick mention of some these methods follows:

Matched Filters: methods have incorporated multi-threshold probing [101], [102], 2D Gaussian matched filters [103], [104],[105], Laplacian of Gaussian filtering [106] and phase concurrency and log-Gabor filtering [107].

Vessel Tracking: methods include recursive tracking [108], [109], matched filter based tracking [110] and model based tracking [111].

Multiscale: methods include Hessian eigenvalue decomposition [44], maximum principal curvature [112] and multiscale line tracking [113].

Modelling: methods include laplacian profile modelling [114],snakes [115], ribbon of twins [116]and level sets [117].

2.5.3 Key point detection

Two types of methods exist for key point extraction from the retinal vasculature, tracking based and vessel segmentation based. In this context, tracking refers to the spatial tracking of points along vessel segments as opposed to the more common definition of tracking movement over time. Tracking methods generally rely on seed points to begin working through the vasculature to find key points. They rely heavily on these seed points and can be computationally expensive. Vessel segmentation methods rely heavily on the accurate results of the vessel segmentation step. A skeleton is made of the vessel segmentation and rules are followed to determine crossings, bifurcations and branches. Grisan et al. (2004) developed an automatic tracking system for key point detection. Seeds are automatically dispersed on the vasculature. From the seeds, the method moves along the vessel extracting center points, width and directional information. When tracking reaches a key point, a circular area around the point is analyzed to determine the type of

key point it has encountered. Also in 2004, Tsai et al. developed a model based method for estimating crossover and bifurcation points. After tracking, position refinement and region exclusion are used to omit traces and combine center line points based on location and orientation.

In 2002, Martinez-Perez et al. [118] proposed a semiautomatic method derived from a vessel segmentation. A vessel skeleton is created from morphological thinning of the vessel segmentation. Aeries of rules are used to correct for misleading points (crossover points that appear to be 2 branching points close together). Other methods have attempted to deal with this issue by incorporating local information at every key point to determine the type, including using rotationally invariant masks along the centerline [119] and angle and width information such as in Martinez-Perez [120].

2.5.4 Vessel width measurement

While vessel width is a quantification metric unto itself, it typically only needs the information from the vessel segmentation step to be performed. Many methods for vessel segmentation include vessel width measurement as part of the procedure. In 1994, Zhou et al. [110] proposed a method for width estimation based on the intensity profile of a Gaussian model. In the same year, Rassam et al. developed an algorithm for measuring the half height points on each side of a centerline point on a vessel. The full width half max is he distance between these two points. Lowell et al. (2004) [121] developed a measurement based on a difference of Gaussian model. This method is able to model the light reflex in if it is present. Otherwise the normal Gaussian model is used in its place. In 2008, Bhuiyan et al. [122] used adaptive region growing to detect the edges of vessels and an unsupervised texture classification to detect vessel centerlines. From the centerline, a rotationally invariant mask is used to find the shortest length between edge points.

2.5.5 Artery/Vein classification

Artery vein classification is another important step for calculating vessel quantification metrics. In Fig. 2.10, AV classification comes as the last step before making most of the retinal vessel measurements. This is a difficult step due to the needed accuracy of previous step to create an accurate account of the vessels and key points. Errors in these steps will propagate forward and give faulty results in the vessel measurements. In 2002, Chrastek et al. [123] developed a fully automated system that used the red channel information at crossing to classify segments. Grisan et al. (2003) [124] found that features relating the variance of the red channel and mean of the channel were particularly discriminative. They calculated these features in quadrants around the optic disc. The group later moved to calculation using the strength of the central reflex as the discriminative feature [125]. Rothaus et al. 2009 [126] developed a semi-automated method based on a set of rules propagated from a few labelled vessel segments. The rules are based on anatomical features of the vessels (ex. arteries don't cross arteries). Niemeijer et al. (2011) [127] combined their previous methods in vessel segmentation, optic disc detection and vessel width measurement for AV classification. This is only performed in the AV ratio region described in the following section. Features are extracted for vessel centerline pixels and classified based on the median label for each segment. Zamperini et al. (2012) [128] looked back at previous works to determine what features have worked the best in separating arteries and veins. They found that a mix of features related to color and contrast both inside and outside the vessels and positional information gives the best classification results. In 2015, Eppenhof et al. developed a method for AV classification based on graph cut optimization. Local and contextual information is extracted from the vessels and integrated into an energy function which is then optimized.

2.5.6 Artery/Vein ratio (AV ratio)

AV ratio is a fairly straight forward calculation once the rest of the information has been gathered from the image. In 1999, Hubbard et al. [129] laid out the basis for standards in calculating AV ratio based on earlier work by Parr in 1974 [130]. The Parr-Hubbard formula estimated the central retinal artery and vein equivalent (CRAE, CRVE). This was updated in 2003 by Knudtson which

made slight adjustments to the formula [131]. The protocol includes centering on the optic disc and performing the analysis in a donut region one half a disc diameter to one and a half disc diameters away from the optic disc. In this region, the widths of the arteries and veins are calculated and a form and plugged into the CRAE and CRVE formulas. The AV ratio is then the ratio of these two values with values farther from one being more suspect.

2.5.7 Arteriovenous nicking quantification (AV nicking)

There has been much less work in the area of AV nicking and more specifically the signs that make up AV nicking. This is due to the difficulty of quantification and the previous lack of high quality imaging that is now abundant. We have found two other methods for AV nicking quantification. In 2013, Nguyen et al. [120] developed an automated method for AV nicking assessment. The system consists of vessel segmentation and crossover point detection systems previously developed to isolate the areas of interest. The vein widths at the crossing are calculated directly from the vessel segmentation, which uses global threshold values. In 2014, Roy et al. [132] improved upon the method by replacing the vein widths from the segmentation with local intensity and gradient information. Neither of these methods attempted add in the angle information associated with the Salus sign in AV nicking, an effect we think makes AV nicking a more robust and reliable metric.

2.5.8 Tortuosity measurement

Several methods for retinal vessel tortuosity quantification have been developed over the years. One of the earliest metrics was proposed by Lotmar et al. in 1979 [133]. The metric, known as arc to chord ratio, is simply the ratio of the distance between the vessel end points and the distance along the entire curve. This method has been popular due to its simplicity, but several studies have shown that the method would produce similar tortuosity scores for in vessels that humans perceive as varying widely in tortuosity [134], [135]. Several methods proposed to improve upon this metric. Bullit et al. (2003) [136] introduced inflexion points into the measurement as a multiplicative term to the arc to chord ratio. Also in 2003, Grisan et al. [135] improved upon the

arc to chord method by implementing the inflexion point method with a slight twist. The arc to chord ratio is calculated for every curve in the vessel and summed (rather than over the entire vessel) while incorporating the number of curves and overall length of the vessel into the calculation. The normalization over the length of the vessel is what makes this known as a tortuosity density metric. This method has been one of the best performing methods since its inception, but a recent study has shown that it can be susceptible to non-ideal sampling rates [134]. On a different line, Chandrinos (1998) [137] proposed a method for tortuosity estimation based on local direction variation, computing the average of the angle change between sample points along the vessel path. In 1999, Hart et al. [138] came up with a series of integral curvature metrics for tortuosity quantification. The idea being that the integral measures would measure the variability of the vessel direction. They also incorporated the chord length into their calculations to normalize for the length of the vessel. In 2006, Azegrouz et al. [139] expanded on one of Hart's measures based on local curvature by adding the thickness of the vessel into the equation. This work was expanded upon in 2010 by Trucco et al. [140], which showed evidence for vessel caliber playing a role in tortuosity. Dougherty et al. (2000) [141] quantified arterial tortuosity based on the second difference of the vessel centerline. The method is sampling independent and similar to calculating the net total curvature of the vessel. Similar to the methods in Hart et al., Patasius et al. (2005) [142] proposed a method based on the integral of the squared derivatives of curvature, thought to capture directional change information in the curves. In 2013, Bribiesca et al. [143] came up with a method known as slope chain coding (SCC). The method approximates a vessel centerline as a piecewise linear curve and calculates the slope change between adjacent line segments. The summation of the absolute value of these slope changes is the final metric. The metric has been shown to vary depending on the frequency of sampled slope points.

2.6 Conclusions

This chapter has presented the background knowledge necessary to the understanding of retinal vessel quantification with respect to hypertensive and diabetic retinopathies. The disease pathologies in terms of biological processes and image level presentations have been described as well as the most common methods for imaging and diagnosis. The typical retinal vessel measurement framework was described along with popular methods for achieving each step in the process. Finally, an in depth literature review of the main thesis topics of optic disc detection, AV nicking and tortuosity measurement were presented. The following chapters will present the proposed methods and results for the detection and quantification of these three important steps.

Chapter 3

Optic Disc Detection

The optic disc is the bright circular region of the retina that houses the optic nerve head and is the entrance point of the main retinal artery. In this chapter, we propose a novel method for the detection of the optic disc. This chapter is based on the following publication:

Wigdahl, J., Guimaraes, P., Ruggeri, A., A Shortest Path Approach to Optic Disc Detection in Retinal Fundus Images, Journal of Modelling in Ophthalmology, Vol. 2 2016 (Accepted)

3.1 Introduction

The optic disc (OD) is one of the most important features of the retina and appears as a bright, yellowish oval. The size of the OD varies among adults with an average of 1.88 and 1.77 mm in the vertical and horizontal diameters [144]. It is the entrance point for blood vessels into the retina and the exit point for ganglion cell axons, which form the optic nerve upon leaving the eye. Detection of the OD can aid in the detection of other retinal landmarks such as the fovea and retinal arcades, which share geometric properties with the OD. Further, analysis of the optic cup-to-disc ratio can aid in the diagnosis of glaucoma while analysis of the OD boundary can be important for swelling of the OD in papilledema. Neovascularization at the disc is an important sign in proliferative DR. Masking the OD out of the image can also be helpful as it removes a bright

area with sharp contrast that could be falsely detected as vasculature or pathology. Studies have shown that during a retinal imaging session, two images per eye are generally sufficient to capture signs of sight threatening disease [29],[145]. A field 1 image (based on the ETDRS seven fields of view) and field 2 image which are optic disc centered and macula centered respectively, with the optic disc on either the right or left side of the image depending on the eye being imaged [146].

The literature review showed that OD detection is a problem that has been worked on for many years and that the methods can be broken down into the OD features chosen for analysis. Many methods exploit the brightness of the optic disc, as it should be the brightest region in the image. In normal cases, this is generally true, but different lesions such as exudates or cotton wool spots can be brighter, or non-uniform illumination across the retina can make this simply not true even in the normal cases. Other methods have proposed to use the information of the vessels. The main arcades exit the OD vertically before curving around the retina, forming a parabola. Other methods have used the shape of the OD to use a template matching approach or the circular Hough transform. Both of these types of methods will have trouble dealing with low contrast images or normal variants.

This work presents a new method for OD detection in retinal images that converts the retinal image to a graph and calculates the shortest path between selected points in the periphery of the image using edge weights calculated from a vessel enhanced image. Through the calculation of several shortest paths (using Dijkstra's shortest path algorithm [147]), the algorithm is able to detect the vascular origin and thus the OD location, after refinement using a combination template matching / vertical edge detection technique. Dijkstra's shortest path algorithm has been used in many image processing applications [148], [149], but has not been used to our knowledge to detect the OD in this way. The method is evaluated on 3 publicly available datasets containing a total of 1329 images of varying levels of pathology and image quality and has a

combined detection rate of 99.40%. These results show that the algorithm is robust and comparable with other state-of-the-art methods for OD detection.

The rest of the chapter is organized in the following manner: in Section 3.2, the data and methods are described. The results and discussions are presented in Section 3.3. Finally, Section 3.4 concludes this chapter.

3.2 Materials and Methods

3.2.1 Datasets

The proposed method was tested on several publicly available datasets and one in house dataset that combine normal images, diseased images, and varying levels of image quality.

In-house: The in-house dataset consists of 127 images with varying degrees of image quality. The images are all 45° field of view and 3168x4752 pixels. There are no diseased images, but the set contains imaging artifacts such as eyelashes and bright halos as well as dark, low contrast images.

DRIVE: The DRIVE dataset was created to compare vessel segmentation algorithms and consists of 40 images (7 with mild diabetic retinopathy, 33 with no signs of disease) used to make clinical diagnoses [42]. The image were acquired on a Canon CR5 non-mydriatic camera at a 45° field of view and 768x584 pixels and were compressed into JPEG. While this dataset consists of high quality images with little disease, it has been used to benchmark OD detection algorithms for many years and is included for this reason.

DIARETDB1: The diabetic retinopathy database and evaluation protocol consists of 89 images (5 with no signs of disease, 84 with at least mild non proliferative retinopathy) [10]. Images were acquired at a 50° field of view and 1152x1500 pixels and saved in the PNG format.

Messidor: The Messidor database consists of 1200 image. All images were acquired using a Topcon TRC NW6 non-mydriatic camera at 45° field of view, 800 with pupil dilation [43]. The images were captured using 8 bits per color plane at 1440x960, 2240x1488 or 2304x1536 pixels.

3.2.2 Methods

This work calculates the shortest path between selected points on the periphery of a fundus image, based on edges weights calculated from a vessel enhanced image, to determine the approximate OD location. The segment with the maximum number of 'shortest paths' is combined with the results from OD template matching and the vertical Hessian component to localize the OD location. Correlation values are then used as a check to determine if the location found is a likely OD location. If not, an iterative process checks larger portions of the shortest path until conditions are satisfied or a lower bound reverts the location back to the original. Fig. 3.1 shows the flow of the algorithm from preprocessing through OD localization.

3.2.2.1 Preprocessing

All preprocessing steps are performed for vessel enhancement. Images are resized based on the image resolution and the background is cropped before processing. All processing is performed on the green channel image due to its superior contrast between blood elements and background. To prevent unwanted contrast along the circular edge of the field of view, a mirroring technique is used to fill in the remaining black background pixels that roughly follows formula 3.0.

$$G_{mir}(x,y) = \begin{cases} G(x,y), & when\ G_{mask} = 1 \\ G(2 * dist(\sim G_{mask}) \pm x, 2 * dist(\sim G_{mask}) \pm y), & when\ G_{mask} = 0 \end{cases} \quad (3.0)$$

A mask, $G_{MASK,}$ of the field of view is created, with all pixels outside the mask needing to be mirrored. Pixel values are mirrored from the original green channel image, *G*, based on their distance from the circular edge of G_{MASK}, with respect to the center of G_{MASK} as seen in Fig. 3.1. The sign change for x and y depends on the quadrant of the image the mirroring is being done. A variation of this formula allows for the varying of the angle with respect to the center of the image

which allows one to pull different amounts of information from the x and y directions. This removes all of the black background pixels and leaves a rectangular region for future processing.

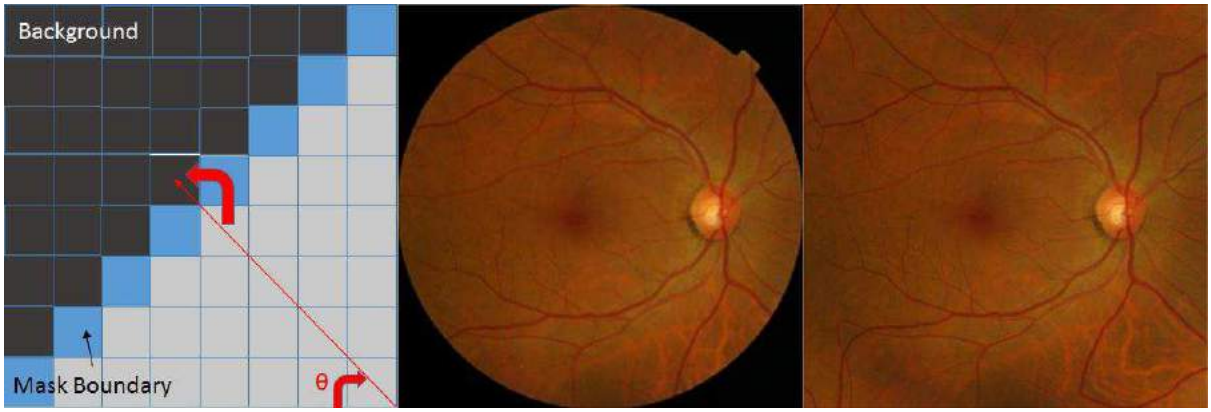

Figure 3.1 Process and example of image mirroring of the background in a retinal image. At a 45°, the mirroring is 1 t 1 based on the distance from the mask boundary. Different angles will pull more information from the x or y direction depending on the angle. The purpose, however, is to remove the boundary between the foreground and background, making further processing easier.

The image then undergoes illumination correction by means of background estimation. The background illumination is estimated using a Gaussian low-pass filter with a large kernel as in the following equation.

$$G_{ill} = G(x,y) - G_{LPF}(x,y) + mean(G_{LPF}(x,y)) \quad (3.1)$$

Where $G_{LPF,}$ the low-pass filtered version of G, is subtracted from G and the mean value of G_{LPF} is then added back to create G_{ill}, the illumination corrected image. The largest kernel size used for the low-pass filter is 1/10*((rows+columns)/2). The Contrast was then normalized and enhanced using contrast limited adaptive histogram equalization (CLAHE), which operates on windows of pixels rather than attempting to equalize the histogram of the entire image at once [150]. When performing adaptive histogram equalization under a relatively small intensity range, noise can be amplified and/or artifacts can appear in the region. Contrast enhancement is directly proportional to the slope of the cumulative density function (CDF) at that intensity (this is equated to the height of the histogram at that intensity). Therefore, to limit contrast enhancement in areas of the CDF

with a sharp slope, we can clip the histogram of that region at a predefined value. An example is shown in Fig. 3.2.

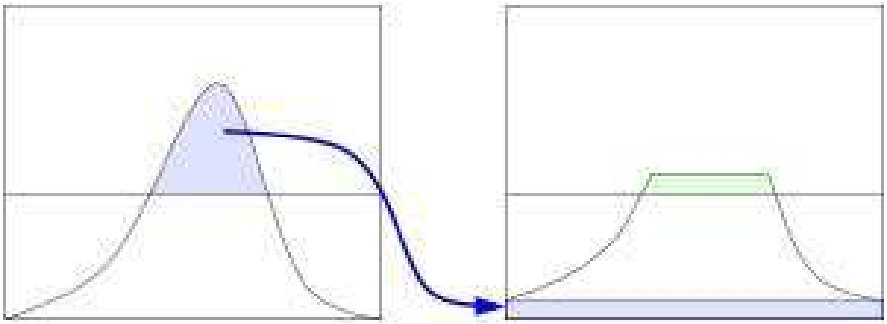

Figure 3.2 Example of the clipped region of a histogram being redistributed evenly through the histogram. This will push the height of the histogram above the clip limit again, so it advantageous to choose a value slightly lower than the value needed. Image provided by [12].

The clipped area of the histogram should then be redistributed evenly throughout the histogram. This will push the height of the histogram over the value chosen for the clip limit, so it is recommended to choose a value slightly lower than the desired contrast limit to counteract this. This method has been very useful in medical imaging, where there can be high levels of noise, large dynamic intensity ranges and low contrast. This method allows for the enhancing of contrast without overly enhancing the noise, which could be confounding to subsequent processing. For the purposes of this method, the tile size chosen was 8x8 pixels and clip limit of .01, which will increase contrast without over amplification of noise. A visual example of the preprocessing steps is shown in Fig. 3.3.

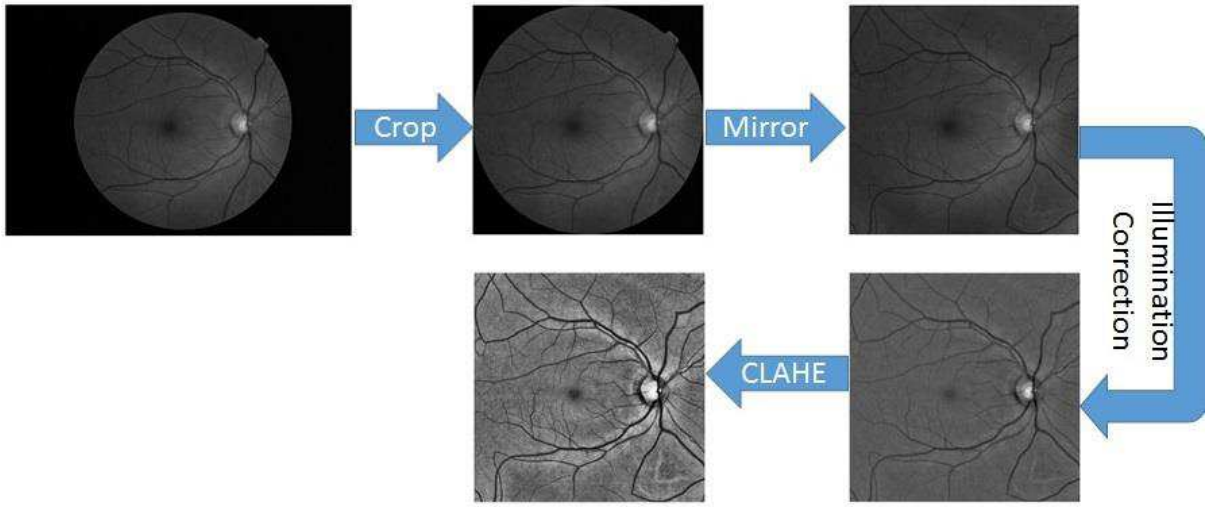

Figure 3.3 The preprocessing steps before the vessel enhancement procedure. The image is cropped and the black border is mirrored. The background illumination is corrected before the contrast is adjusted.

3.2.2.2 Edge weight calculation

An undirected graph *Gr*(*V, E*) is a set of vertices and edges, where in our images *V* is every pixel in the foreground of the image and *E* is the set of connections between pixels. Each edge, *E*, can have an associated weight. General values for edge weights can be some measure of distance between vertices or in this case, the images pixel intensity values. The edge weights are taken as the pixel values after performing Frangi vessel enhancement [44]. As a short explanation, Frangi vessel enhancement uses the eigenvalues of the Hessian 2D matrix of the image to enhance vessel-like structures. The Hessian consists of second-order partial derivatives, as shown in formula 2, which are generally smoothed by a simple Gaussian function.

$$H(x,y) = \begin{vmatrix} D_{xx} & D_{xy} \\ D_{yx} & D_{yy} \end{vmatrix} \tag{3.2}$$

Where D_{xx} through D_{yy} are the partial second derivatives of the Hessian, H(*x,y*), that describe the gradient of the image in different directions. The amount of smoothing is controlled by the

standard deviation (sigma) of the Gaussian function. From the Hessian, the eigenvalues are decomposed and the following formulas are used to extract candidate tubular information:

$$R_B = \left(\frac{\lambda_1}{\lambda_2}\right)^2 \tag{3.3}$$

$$S = \sqrt{(\lambda_1)^2 + (\lambda_2)^2} \tag{3.4}$$

Where $\lambda_1$and λ_2 are the two largest eigenvalues, R_B represents a "blobness" measure and S represents a second order structure measure. These two metrics are then combined into the following "vesselness" metric.

$$I_{enh}(s) = \begin{cases} 0 & if\ \lambda_2 < 0 \\ \exp(-\frac{R_B^2}{2\beta^2})(1 - \exp(-\frac{S^2}{2c^2})) \end{cases} \tag{3.5}$$

Where β and c are constants that control the tubular filter. $I_{enh}(s)$ is the vessel enhanced image at sigma value s. The enhancement is performed at multiple scales (varying the standard deviation of the Gaussian smoothing filter) and the maximum response at each pixel becomes the vessel enhanced image. In this particular case, we want to ignore the smaller vessels and only capture the primary and secondary vessels in the image (This is done to lessen the possibility of false paths being created as we will see later). Thus, a higher band of sigma values (16-26) were used so that the tertiary vessels were not enhanced. The values from the vessel enhanced image are used as

the edge weights in our graph after being normalized between 0 and 255 and inverted, so that vessel pixels have lower weights. We now must determine the starting and ending points from which to calculate the shortest paths. The points chosen are equally spread around the periphery of the graph. The image is cut into four quadrants as shown in Fig. 3.4. Starting points in quadrants 1 and 2 are matched with end points in quadrants 3 and 4. Four points from each quadrant are matched with each point in the adjacent quadrant for a total of 32 shortest paths. As converting the image to a graph and calculating the shortest paths is an expensive process, the image is down-sampled by a factor of 4 after vessel enhancement. To calculate the shortest path between the selected points, Dijkstra's shortest path algorithm is used [147]. The algorithm allows for the finding of the shortest path from a starting node to every other node in the graph in $O(log(V) * E)$ time, where V is the number of vertices and E is the number of edges. In the attempt to find the shortest path to the other side of the image, the main arcades and secondary vessels will act as highways, directing the shortest path through the convergence of vessels at the optic disc. As more 'shortest paths' are calculated, a histogram is built up of the number of shortest paths at each point in the graph, corresponding to each pixel in the image. The line segment that is maximum from the histogram will be the rough estimate of the OD location.

3.2.2.3 Template matching/Edge detection

The use of OD templates and vertical vessel information has been used before to detect the OD and has proven effective in its own right [87]. In this case, the method differs in that the information is combined into a single image and used only in the line segment of OD candidate. The line segment found from the shortest path must be narrowed to a single pixel location. To do this, a combination of correlation with an OD template and vertical edge information is calculated in the region of interest. The OD template incorporates the assumption that the OD is a bright oval region with darker vessels exiting nasally, while the vertical edge information assumes that the main arcades exit the OD vertically before curving into a parabolic shape. The calculation of

the vertical edge information has already been carried out when we previously calculated the Hessian for vessel enhancement. We use the normalized gradient information from *Dyy* in formula 2 as the vertical vessel component, combined with template matching correlation scores. The OD template used is 100x100 pixels and is composed of the combination of 10 randomly selected OD's (seen in Fig. 3.4), extracted from 10 images from an in-house dataset, averaged together and normalized. Since there is no a priori information or recognition of whether the image is from a right or left eye, two templates were used. The original was created from left eye images and then flipped for right eyes, as using a different template for both eyes could create a bias. The maximum value combining the normalized template correlation values and vertical gradient information along the segment with the highest number of shortest paths gives the OD location.

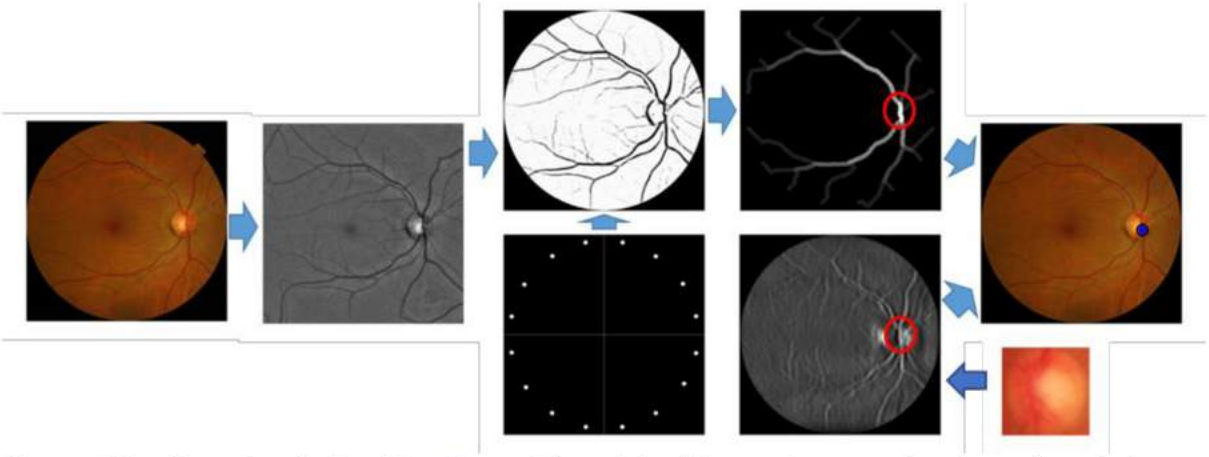

Figure 3.4: Example of algorithm flow. The original image is cropped, mirrored, and the illumination is corrected. The Frangi vessel enhanced image is used for the graph weights. Points along the outside of the image are connected via shortest path across quadrants. The area with the maximum number of 'shortest paths' is the initial search zone, and the final optic disc location comes as the maximum of the edge detection/template matching combination on that line.

3.2.2.4 Correction

There are several cases where it becomes clear the incorrect OD location has been found. While this happens rarely, an iterative process is deployed to determine if there is a more likely OD location. If the template / vessel gradient information is much lower than the maximum value in the image, the maximum segment requirement is decreased, to allow for a slightly larger search

area. This process will continue until areas that have 60% of the maximum number of shortest paths have been checked. At this point, if a better candidate has not been found, the OD location will revert to the original location found on the segment with the maximum number of shortest paths.

3.3 Results and Discussion

Results are given for the three publicly available datasets and compared with many other algorithms on these datasets which can be found in Table 3.1. The results of the DRIVE dataset were a 100% detection rate of the optic disc. From Table 3.1, it can be seen that many methods obtain these same results as these image are typically of good quality and contain very little disease (7 images with mild DR). It should also be noted that correction in this dataset was unnecessary. Fig. 3.5 shows a sampling of correctly detected images from the database. A 98.88% detection rate was achieved on the DIARETDB1 database. This amounts to missing a single image from the 89 image dataset. That image can be seen as the last image in Fig. 3.8. A combination of a dark OD and low contrast in the area had the algorithm second guess its initial estimate, which was just below the OD. Correctly identified OD locations from the dataset can be seen in Fig. 3.6. The dataset contains 84 images with at least mild diabetic retinopathy. Since nothing in this algorithm is done to depress the contribution of lesions in the vessel enhancement step, large numbers of lesions can occasionally create a short circuit in the shortest paths calculation, splitting some paths and requiring correction to properly detect the OD. While this occurred, the algorithm was able to correct the OD location in each case. The optic disc was found in 1193 of the 1200 images in the Messidor data set for a 99.42% detection rate. Correctly detected OD locations for this database can be seen if Fig.3.7. All seven of the misses can be seen in Fig. 3.8. The main reason for incorrect detection was blur, either from poor image quality or possible cataract that covered either the OD vessels or the main arcades from an entire hemisphere of the image. The second reason for misses was bright regions near or around the OD. These non OD bright regions

will have edges that appear in the vessel enhancement. Fig. 3.9 shows examples of the iterative corrective process successfully finding the correct OD after initially being incorrect.

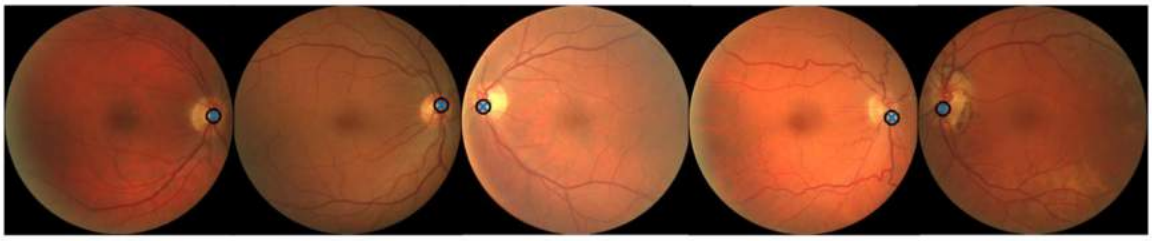

Figure 3.5: Sampling of correctly detected images from the DRIVE database. Estimated OD location is marked with a cross surrounded by a circle.

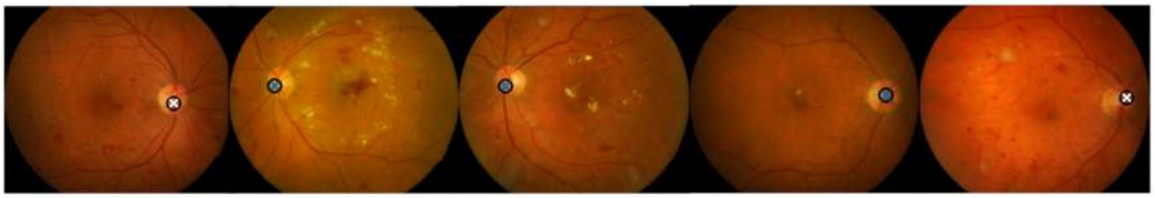

Figure 3.6: Correctly identified OD location in images from the DIARETDB1 database.

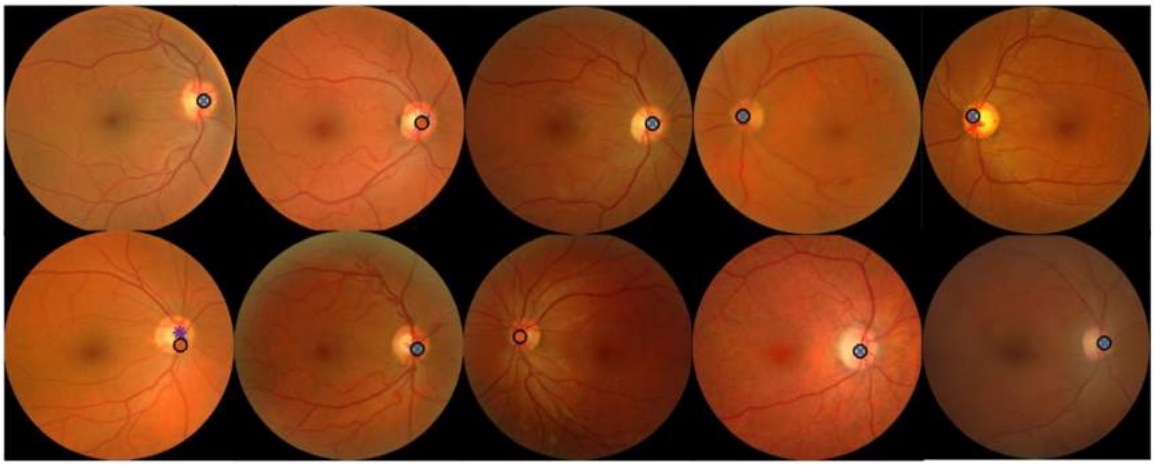

Figure 3.7: Correctly detected OD location in images from the Messidor database.

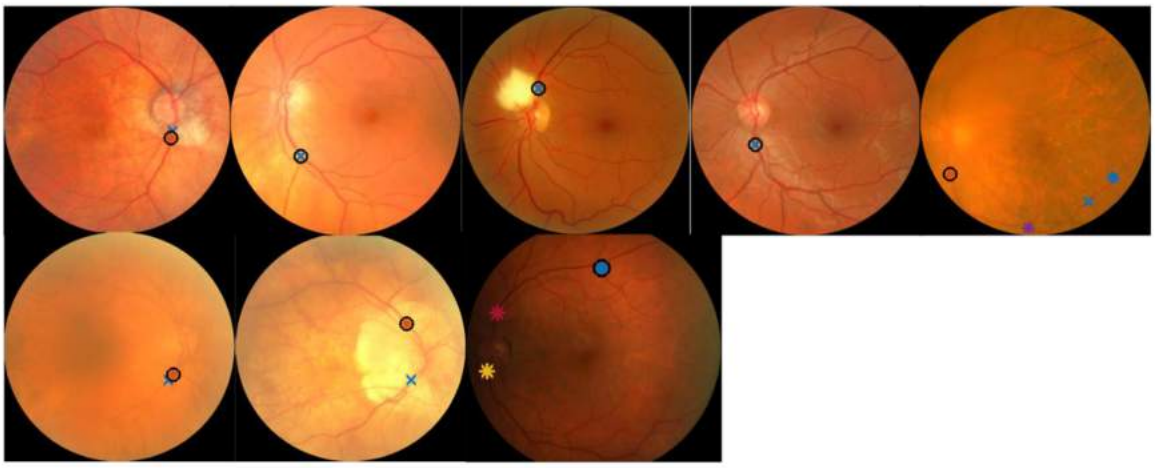

Figure 3.8: All incorrectly detected images. 1-7 Messidor. 8 DIARETDB1. Final estimated OD location is a cross with a circle around it. Attempts at correction can be seen as crosses or stars that have not been circled.

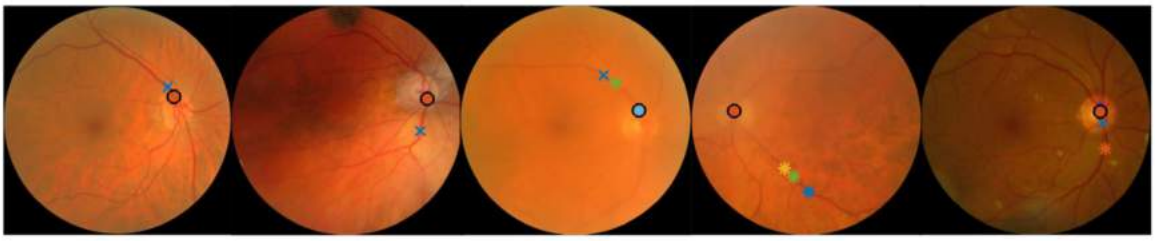

Figure 3.9: Incorrect OD locations that where corrected due to the low likelihood of the original location being the true OD by the iterative correction of the algorithm. Final estimated OD location is a cross with a circle around it. Earlier iterations are shown as colored stars or crosses.

Table 3.1. Comparison of methods that have reported results on one or more of the listed datasets.

OD Location Method	DRIVE dataset (%)	DiaRetDB1 dataset (%)	Messidor dataset (%)
Sinthanayothin et al. 1999	60	-	-
Walter et al. 2002	80	-	-
Youssif et al. 2008	100	-	-
Mahfouz et al. 2010	100	97.75	-
Welfer et al. 2010	100	97.75	-
Aquino et al. 2010	-	-	99
Qureshi et al. 2012	100	94.02	-
Yu et al. 2012	-	-	99.08

Pereira et al. 2013	100	93.25	-
Zubair et al. 2013	-	-	98.65
Saleh et al. 2014	100	-	-
Yu, Ma & Li 2015	100	98.88	99.67
Rahebi & Hardalaç 2016	100	94.38	-
Abdullah et al.[26] 2016	100	100	99.25
Proposed Method	100	98.88	99.42

The algorithm was implemented in Matlab 2016a on a desktop computer (Intel i7 CPU at 3.4 GHz and 16 GB RAM) and average run time was 32 +- 1.2 seconds per image. This time held relatively constant through each dataset due to the up-sampling of the images prior to processing. This could be greatly reduced through code optimization and choice of programming language. Also, 26 of those seconds were spent calculating the Frangi vessel enhanced image to calculate the edge weights for the graph. The Frangi method is not the only one that produces a vessel enhanced image and other methods could replace this one in order to reduce running time or improve results. The number of points used to calculate shortest paths can also affect the results. The number chosen for this study (4 per quadrant) was based on experimentation as a tradeoff between results and processing time. More points could shrink the initial search region for the OD, but placing points too close together will only raise the processing time as these points will likely choose the same shortest path if they are all near the same vessel at the periphery.

This idea presents a global approach to vessel convergence and relies heavily on the presence of the main arcades being present in the image. This usually does not occur in images where the field of view is less than 45 degrees. Older datasets used for testing such as the STARE dataset[15], which was widely used to validate OD detection methods, contains many images at a 30 degree field of view or less. Since there is no convergence of vessels without the main arcades, the

algorithm was not benchmarked on this dataset. However, of the 81 images in the STARE dataset, 46 of the images meet the vessel convergence criteria as either having the main arcades present or were OD centered images, in which vessel convergence is assured. In this subset, the algorithm was unable to detect the OD in 4 images for a 91.3% detection rate.

3.4 Conclusion

This work presents a novel method for OD localization based on the shortest path between points on the periphery of the image using edge weights calculated from a vessel enhanced image to detect the likely convergence of vessels at the OD. The algorithm achieves results comparable or better than results from the state-of-the-art algorithms on the selected databases. The excellent results from the Messidor database show that this method would be useful in an automated screening system or retinal vessel analysis system, where the processing done for vessel enhancement can be used both for OD detection and vessel segmentation, saving overall processing time.

Chapter 4
Arteriovenous Nicking Quantification

AV nicking quantification is important sign in hypertensive retinopathy and can be subdivided into two phenomena, the Gunn sign and the Salus sign. This chapter presents a novel method for the detection and quantification of these two signs based on the following publication:

Wigdahl, J., Guimaraes, P., Leontidis, G., Triantafyllou, A., Ruggeri, A., Automatic Gunn and Salus sign quantification in retinal images, Proceedings of the Annual International Conference of the IEEE Engineering in Medicine and Biology Society, EMBS, 2015.

4.1 Introduction

Hypertension affects nearly 70 million American adults and approximately 970 million adults worldwide [151]. Elevated blood pressure puts stress on the body's blood vessels, often causing damage that can lead to a blockage or rupture. These vascular changes also affect the retina, the sum of which are known as hypertensive retinopathy [152]. The focus of this work is on one specific sign known as arteriovenous (AV) nicking. Thickening of the arteriole wall and/or sclerosis are thought to compress the vein at a crossing point, impeding blood flow, causing a tapering of the vein at the crossing. This tapering is commonly referred to as Gunn's sign. The pressure from the artery can also displace the vein at the crossing, causing the vein to enter and exit the crossing at a 90° angle. This phenomena is commonly referred to as the Salus sign [153]. Fig. 4.1 shows examples of crossing that show one or both signs, highlighting the tapering and displacement.

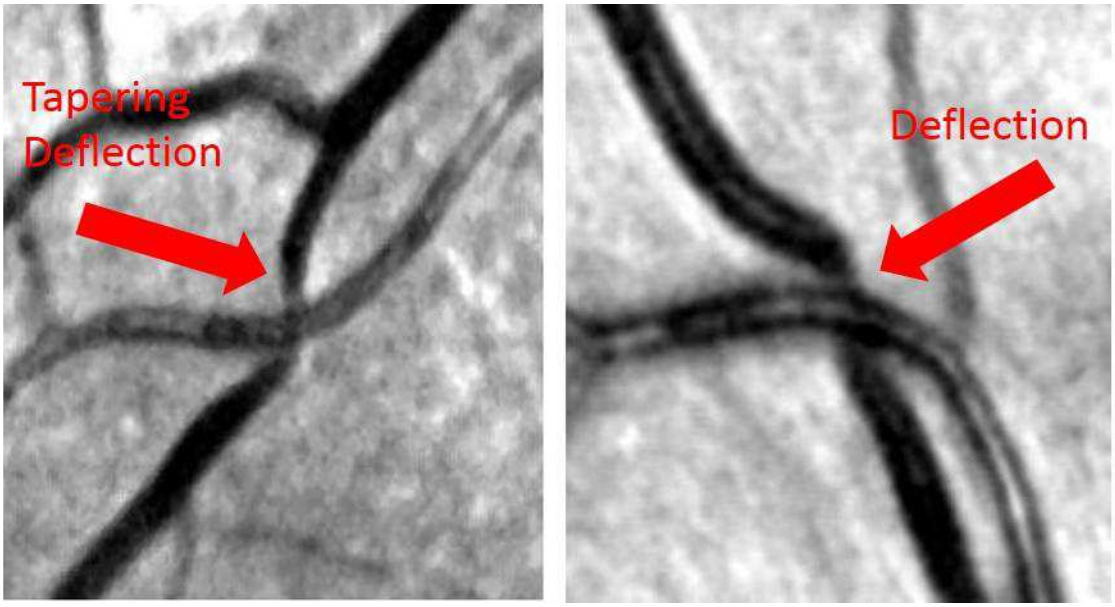

Figure 4.1 Two crossings show signs of AV nicking. Left Image: The crossing is deflected (Salus sign) from the original course and shows tapering as it enters the crossing (Gunn Sign). Right Image: Deflection of the vein (Salus Sign). Image Contrast makes any sign of tapering difficult to visualize.

Crossing abnormalities are a grade 2 sign (1-4 scale) on the Keith-Wegener-Barker hypertensive retinopathy grading scale [76]. To our knowledge, there is no standard for grading the severity of crossing abnormalities. Typically, AV nicking is a binary marker added to the larger hypertensive grading scale. However, AV nicking is a major factor in the development of branch retinal vein occlusions (BRVO) [154]. Quantification of AV nicking may be important to the prediction of development to more serious conditions such as this. Further, as Fig. 4.1 shows, both signs are not always visibly present. Although at this time there is no evidence that quantifying the signs separately holds any clinical value, it may help to identify more abnormal crossings that may be missed due to poor contrast in the region.

In this work, we present a method for the quantification of the Gunn and Salus sign at retinal arteriovenous crossings. After a crossing is found (by automatic or manual means), the vessels in that area are segmented using the method introduced by Frangi [44] which has been previously discussed in chapter 3. The four corners of the crossing are detected by way of distance

transformation and used to create a bounding box to separate the four vessel segments. Color intensity features and vessel profiles are used to determine the artery from the vein. Vessel widths are then measured using a monodimensional matched filtering technique. These widths are used to determine the Gunn sign while the angles created at the corners of the bounding box are used to determine the Salus sign. The results are then compared with the findings of graded crossings from two datasets.

The rest of the chapter is laid out in the following manner: In Section 4.2, the data and methods are described. The results and discussion are presented in Section 4.3. Finally, Section 4.4 concludes the chapter.

4.2 Materials and Methods

4.2.1 Data description

Private Dataset: Images were acquired from the 3rd Department of Internal Medicine, Papageorgiou Hospital, Aristotle University of Thessaloniki, Thessaloniki, Greece. A group of three doctors (two hypertension specialists and one ophthalmologist) chose a set of five crossings that they agreed showed both the Gunn and Salus signs, backed by the analysis of fluorescein angiography images. These five crossing are joined by a set of five normal AV crossings for comparison. Images were captured at a 45° field of view at 2912x2912x3 pixels. Images were then cropped to 250x250 pixels roughly centered on the chosen crossing point. This was meant as a pilot study and proof of concept to show the feasibility of making these measurements.

Public Dataset: The public dataset contains a set of 90 crossovers taken from 47 high resolution images obtained from the Blue Mountain Eye Study [45] and the Singapore Malay Eye Study [46]. The resolution of the images from each study 3888x2592 and 3072x2592 respectively. The crossing were graded on a scale of 0-4. From these 90 crossings, a set of 63 (32 normal 31 abnormal) were chosen based on their image quality and proximity to the border of the image

(these issues can affect the segmentation at the crossing). This left only images graded on a scale of 0 – 3 (only one crossing in the entire dataset was graded a 4).

4.2.2 Methods

This section describes the steps in the Gunn and Salus sign quantification algorithm. The Gunn sign, a unitless quantity, is calculated as a ratio between the vein width near a crossing and the width farther away from the crossing. The Salus sign is measured as an angle difference of the vein going into and coming out of a crossing. To measure these signs, several steps are followed and expanded upon in the following sections. The assumption made is that a crossing point has already been found either manually or through previous automatic steps.

4.2.2.1 Preprocessing

From the selected crossing point, a 250x250pixel area of interest is cropped from the image. This cropped area is preprocessed by contrast enhancement (CLAHE chapter 3) and illumination correction. For illumination correction, a standard morphological top-hat procedure is used on the inverse of the green channel image patch, which subtracts the morphological opening of image from the original [155]. Formula 4.1 shows the procedure:

$$T(g) = g - g \circ b \tag{4.1}$$

Where g is the green channel image, b is a grayscale structuring element and $\circ$ is the opening operation. The opening operation itself is shown in formula 4.2:

$$g \circ b = (g \ominus b) \oplus b \tag{4.2}$$

Where the opening operation, $g \circ b$, is the erosion, $\ominus$, of grayscale image g by structuring element b followed by the dilation, $\oplus$, by that same element. The top-hat transform of g, T(g), is then the image minus the morphological opening of the image. For this algorithm, a disk shaped structuring element with a diameter of 15 pixels is used. This will enhance bright structures that are smaller than the structuring element, of which the vessels qualify. Finally,

the image patches are also slightly blurred using a small Gaussian low-pass filter of size 3x3 and standard deviation of 1. It should be noted that the size of the structuring element and low-pass filter are dependent on the image resolution and would need to be scaled up to accommodate higher resolution images.

4.2.2.2 Vessel segmentation

The well-known multi-scale vessel enhancement method proposed by Frangi [44] is used to segment the vasculature. The process is the same as in chapter 3 but will be briefly summarized. The eigenvalue decomposition of the Hessian is computed at different scales (convolution with a Gaussian of varying sigma values). These scales should cover the width of the structure one is looking to enhance. For this work, the sigma range was from 4-10. The 'vesselness' of a pixel is determined by two metrics known as 'blobness' and 'second order structureness' (formula 3.3,3.4). The blobness metric is the ratio of the 1^{st} eigenvalue to the 2^{nd}. The second order structureness is the square root of the sum of the squared eigenvalues. Vesselness is then determined by a combination of these metrics as shown in formula 3.5. The maximum value is found across all scales, forming a vesselness image. A threshold is applied to the image to create the segmented vessel image after small morphological corrections to fill small holes and omit small disconnected segments. The vessel segmentation is used to remove the vessel crossing section and is described in the next section.

4.2.2.3 Crossing segmentation

Once the vessel segmentation is found, a distance transformation is applied to the binary image with respect to the coordinates of the found crossing point. A search is then performed to find the corners of a bounding box that covers the entire crossing. The distance transform assigns a value to each pixel based on its distance to the origin. The vessel pixels are assigned a value of 255 (higher than the maximum distance). A search is then performed to find the closest nonzero valued distance pixel in each direction starting from the crossing coordinates. Lines are projected

out from the origin at different angles, the lowest nonzero value for each angle is recorded, and a plot is made of these values. The centers of the four troughs represent the coordinates of the corners of a bounding box covering the crossing. Fig. 4.2 shows an example of this process from vessel segmentation to crossover identification. In order to accurately determine the troughs in the graph, line segments must be projected to represent as many angles as possible. This is to insure that a trough is not missed between vessel segments that are very close together. We found that using a projection every 5 degrees was adequate to capture the troughs without overly redundant information being calculated.

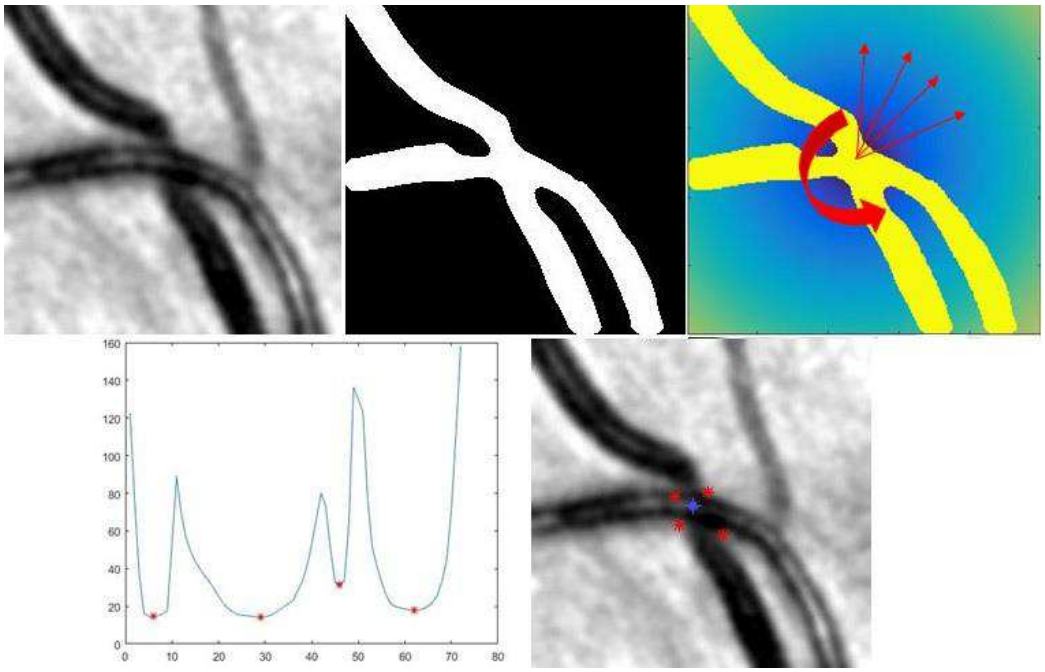

Figure 4.2 The process for determining the bounding box for the crossover. A vessel segmentation is performed. A distance transform is applied to the image and a search is performed for the four corners, which will appear as low points on the graph.

4.2.2.4 Artery/vein classification

Removing the crossover from the vessel segmentation separates the four segments coming in and out of the crossover. With the lack of global information to inform the process, to differentiate the artery from the vein, the mean RGB intensity values are calculated for each segment as well as average cross sectional profiles. In general, the arteries are lighter in color (difference between

visualization of oxygenated and deoxygenated blood) and often display a bright central reflex, both of which can be seen in the example in Fig. 4.2. Since we know that this is a crossing point, segment pairs across from each other will be of the same class so the information can be combined leaving only two possibilities for classification. We have only two main features, so a rule-based approach is employed. Since the bright central reflex is not always present (or can be present in the vein as well), the first is based on the mean intensities. If a clear distinction can be made, there is no need for a further check. If the intensities are close, the intensity profile is checked to make the final determination.

4.2.2.5 Vessel width measurement and angle detection

We are now working only with the vein segments. These segments are skeletonized and converted to a graph representation. From the points on the skeleton, beams are sent from the origin to the edges of the skeleton. This is done at 12 degree increments counterclockwise to capture the distance information to the edge at each interval. The crossing is put back into the segmentation so not to bias measurements near the crossing. The beam with the shortest path is considered the line perpendicular to the vessel centerline. The centerline point is then updated as the midpoint between the edges of the beam and the angle is recorded for use in Salus sign quantification. The length of the beam also provides a starting point for vessel width estimation. To estimate the widths, a monodimensional matched filter is applied perpendicularly (based on the local directional information) to the profiles along the vessel axis [156]. The starting filter size is based on the beam length previously recorded at each point. The one dimensional matched filter then begins inside the vessel profile, where the response will be maximum and moves outward. The border points are extracted when the filter response reaches a previously determined set threshold. Formula 4.3 shows the matched filter response (MFP) as a function of the profile, *FP* with caliber *c*, convolved with the filter kernel at scale *EC,* the estimated caliber.

$$MFP_{c(i)}(x) = FP_{c(i)} \otimes kernel_{EC(i)}(x) \tag{4.3}$$

If the responses do not meet the threshold or begin below the threshold, the estimate the starting caliber is adjusted to compensate. The process is visualized in Fig. 4.3. With the vessel width and angle information at our disposal, we can now calculate the Gunn and Salus signs.

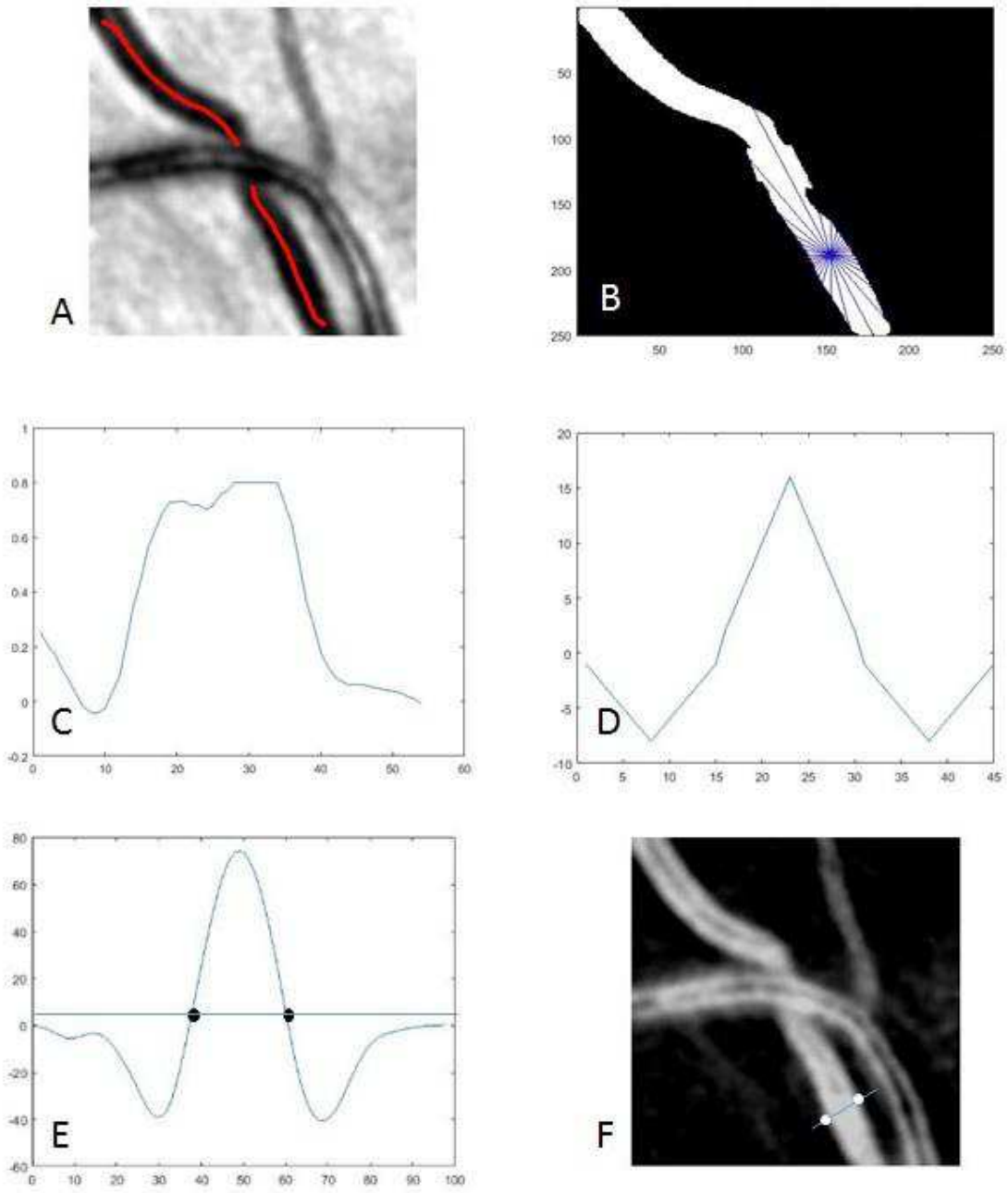

Figure 4.3 The vessel width and angle detection approach. (A) The vessel centerline is approximated from the vessel segmentation. (B) Beams search for the shortest distance to the vessel edge to determine initial an initial width estimate and correct centerline. (C) The vessel profile along the blue line in F. (D) The matched filter and (E) filter response. (F) Image with selected profile and found edge points.

Gunn and Salus calculation

The Gunn sign is a measure of the tapering of the vein at a crossing point. Fig. 4.4 shows an idealized example with measurement points associated with formula 4.4. To measure this tapering, an average vessel width value near the crossing and an average value farther from the crossing must be determined.

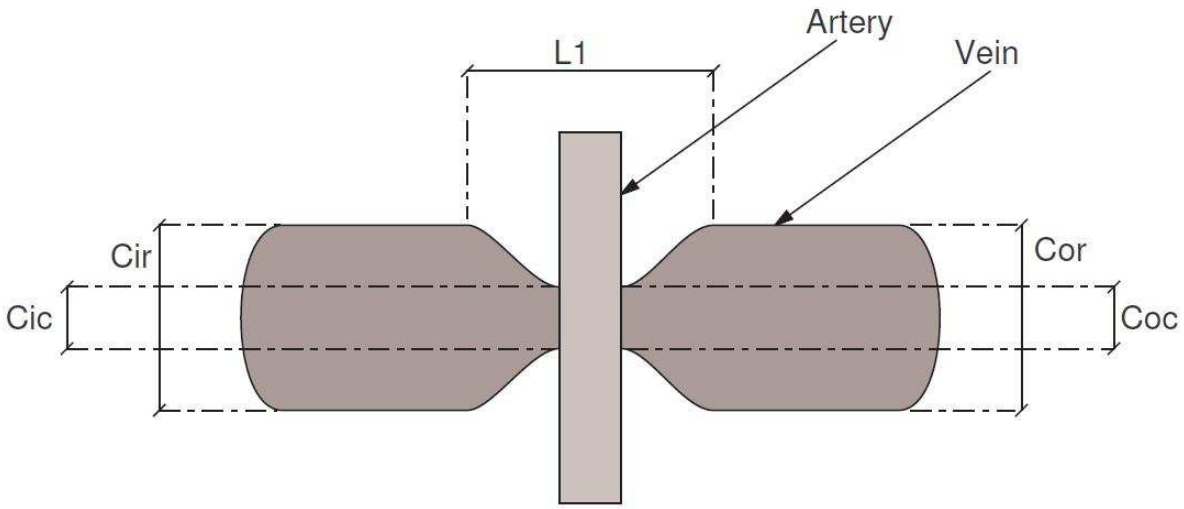

Figure 4.4 Idealized example of the Gunn sign. To determine, the caliber near the crossing and away from the crossing must be calculated. The value L1 is the distance from the beginning to the end of the tapering, but does not factor into the equation except as cutoff points between the near and far width measurement. Image from [157].

$$g_i = \frac{C_{ic}+C_{oc}}{C_{ir}+C_{or}} \tag{4.4}$$

Where C_{ic} and C_{oc} are the vessel calibers near to the crossing and C_{ir} and C_{or} are the vessel calibers farther away from the crossing. The length, L1, for Fig. 4.4 represents the length of the tapered section. This is different for each crossing, but for standardization, the mean of the five

closest points from the graph representation of the vessel on each side of the crossing are used for the close caliber calculation, while the rest of the points are used for the far caliber calculation.

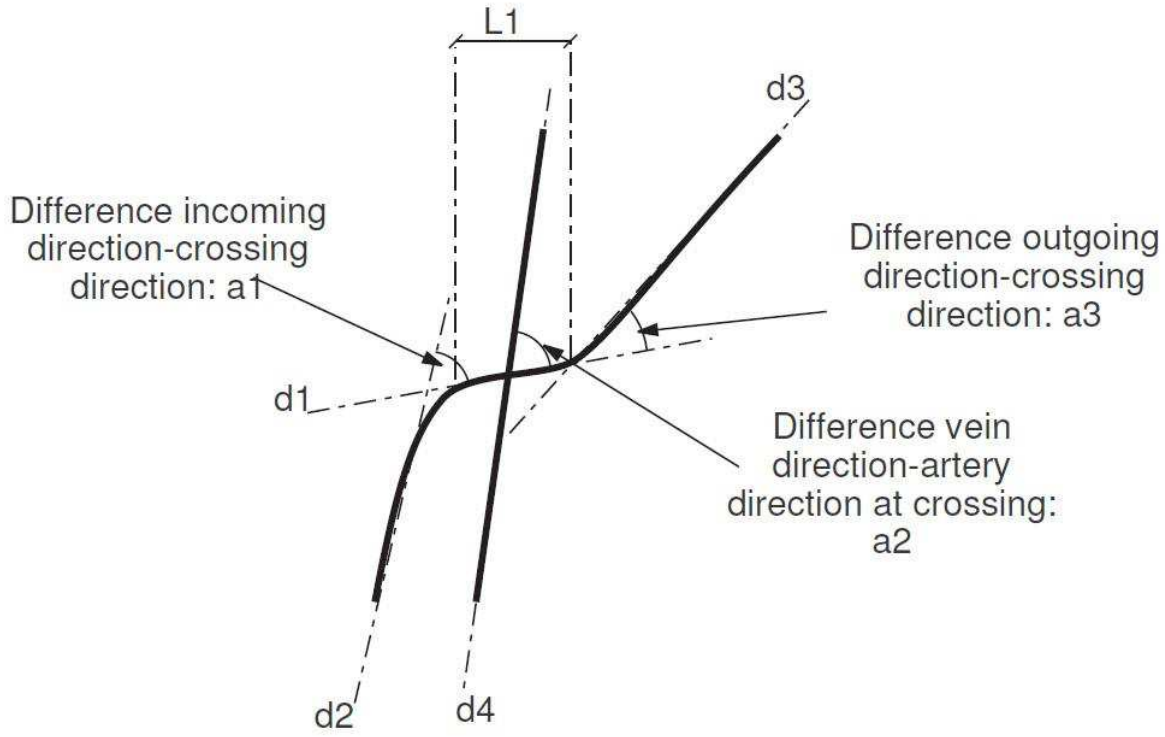

Figure 4.5 The Salus sign quantification. The difference between the angle into and out of the crossing is summed and averaged to give the score. Image from [157].

The S shape of the Salus sign can be represented by three angle values. These are the average direction of the two vein segments going in and out of the crossing, and the direction at the crossing. This is visually shown in Fig. 4.5 and mathematically shown in formula 4.5.

$$s_i = .5 * (a_1 + a_3) \tag{4.5}$$

Where a_1 represents the difference between the angle at the crossing of the vessel with the average angle along the vessel going into the crossing. a_3 represents these same values leaving the crossing. This average difference is then computed from these values.

The vessel widths necessary for the calculation of the Gunn sign as well as the average direction of each vessel segment have already been calculated in the vessel width and angle detection step. The direction at the crossing is calculated by averaging the points closest to the crossing. For this work, both for the angles and widths of the vein, five points close to the crossing are averaged while 20 points along the remaining length of the vessel are averaged. This is done on both sides of the crossing. Fig. 4.6 shows calculated widths and angles at points along the found vessel.

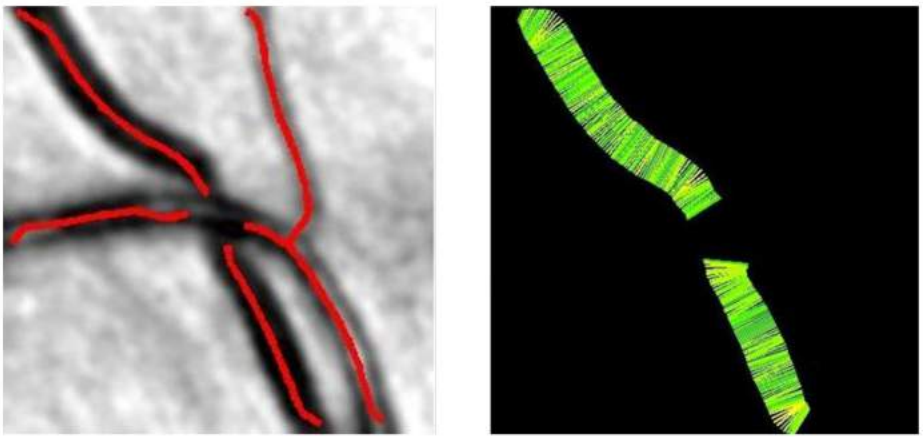

Figure 4.6 An image with vessel centerlines converted to width and angle estimations. The angle estimation is visualized by the color of each line segment.

4.3 Results and Discussion

To evaluate the algorithm, the proposed method was run on both datasets. In the smaller dataset, three graders classified the ten crossings as normal, or showing Gunn/Salus signs. These graders were in agreement on all crossings, removing intergrader variability. The Gunn and Salus sign were then calculated with the proposed algorithm and the results were compared. Table 4.1 shows the results for each of the ten crossings. The Abnormal crossings had a mean and standard deviation Salus sign of .29rad+-.06 and a Gunn sign of .78 +- .11. The normal crossings had a mean/standard deviation Salus sign of .19+-.07 and mean Gunn sign of .94 +- .08 (Table 4.2). The ideal normal crossing would have a Salus sign of 0 and Gunn sign of 1, with the Salus sign moving higher and the Gunn sign moving lower in the abnormal case. The results show separation

between the two groups on this limited data set. However, it is uncertain as to the importance of each individual sign. Whether they can be combined in some manner or thresholded separately. Since the gradings are binary, thresholds should be set for classification purposes. Setting a threshold of .89 for the Gunn sign and .22 for the Salus sign would yield one false positive and one false negative. Fig. 4.7 shows both of these misclassified images along with the most 'abnormal' and 'normal' cases. Even in high quality images, the area around the crossing can have low contrast, leading generally to overestimations of the vessel width at the crossing. This overestimation can also affect the calculated angle into the crossing as well. For this reason, a small buffer is used to avoid the closest points to the crossing. For these calculations, the first 3 points closest to the crossing are discarded. However, it is still likely that the misclassified images suffered from an overestimation of the width at the crossing.

Table 4.1 Gunn and Salus sign results for the 10 crossing under investigation. Gunn sign is unitless and the Salus sign is in radians.

Crossing	*Gunn Sign*	*Salus Sign*
NormalCrossing1	0.89	0.17
NormalCrossing2	1.08	0.14
NormalCrossing3	0.90	0.18
NormalCrossing4	0.91	0.32
NormalCrossing5	0.94	0.15
AbnormalCrossing1	0.71	0.39
AbnormalCrossing2	0.92	0.23
AbnormalCrossing3	0.67	0.29
AbnormalCrossing4	0.88	0.27
AbnormalCrossing5	0.70	0.28

The second dataset was graded differently than the first. While crossing signs are normally binary, the dataset proposed grading on a severity scale from 0 - 3. It is unclear where this severity scale came from, but it should be noted that the authors were only interested in the Gunn sign when it was proposed. Rather than attempting to classify the crossing, we instead looked to see if there was any separation between the nicking signs and the grades. Fig. 4.8 shows a series of

box plots looking at only the Gunn sign with respect to the ground truth grades. The boxplots were split by the grouping the grades. The first boxplot shows each grade separately. Normal crossings had a mean Gunn sign of .956 with a standard deviation of +- .071. The difference between the grade 0 crossings and between each abnormal grade was significant ($p < .05$). This could not be said for the three abnormal grades. Although grade 1 crossings had a higher Gunn sign than grade 2 and 3 crossings, the difference was not significant. We then grouped the grade levels in two ways. First we grouped grade 0 and grade 1 crossings and compared against the grouped grade 3 and 4 crossings. These two groups (.94 +- .07, .83 +- .09) were found to be significantly different ($p < .001$). This can also be said when grouping all abnormal grades against normal crossings ($p < .001$). These significant differences did not show up in the Salus sign however. There was no statistical difference between the grade levels. This isn't to say that the sign is not important. It likely shows that the ground truth did not take this sign into account as well as the difficulty of properly measuring the sign, since some normal vessel direction changes can be picked up in the calculation. It may also be that the Salus sign should be used more as a baseline measurement and compared against in subsequent imaging sessions to see the changes. All results are summarized in Table 4.3.

There are other factors that can contribute to errors in the calculations. The most important and likely is an error in the vessel segmentation. Generally this is attributed to the quality of the image. Another factor is the angle at which the crossing takes place. If the vein and artery are nearly parallel, it is difficult for segmentation algorithms to differentiate between the vessels, which can also lead to segmentation errors. One other likely segmentation error can come from a strong central reflex on the artery.

Table 4.2 Average and standard deviation for normal and abnormal crossings for both the Gunn and Salus sign. Gunn sign is unitless and the Salus sign is in radians.

Gunn Sign	Average	St. Dev.
Normal Crossings	.94	.08
Abnormal Crossings	.78	.11
Salus Sign	**Average**	**St. Dev.**
Normal Crossings	.19	.07
Abnormal Crossings	.29	.06

The algorithm runs a single image using a single core MATLAB (The Mathworks Inc., Natick, MA) implementation in 3.4 +- .3s on an Intel Core i7-4770 CPU (Intel Corporation, Santa Clara, CA) at 3.4 GHz.

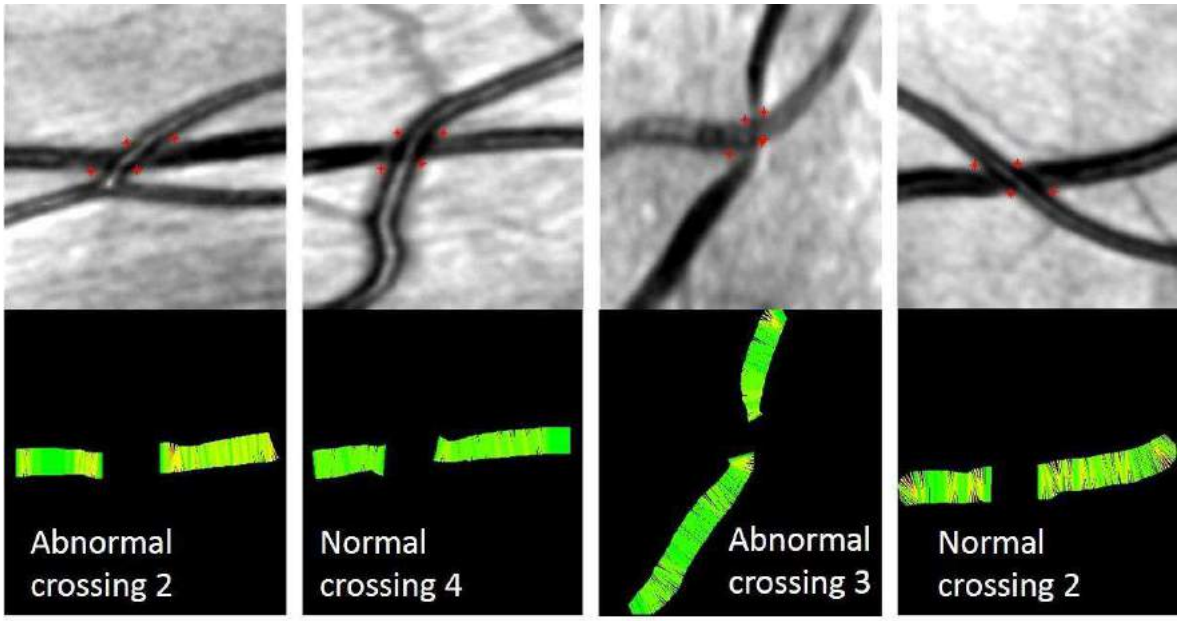

Figure 4.7 A sampling of the crossing and visual results using the algorithm. Abnormal Crossing 2 appears to be a normal crossing from the fundus image. However, the graders were presented with the fluorescein angiography images as well.

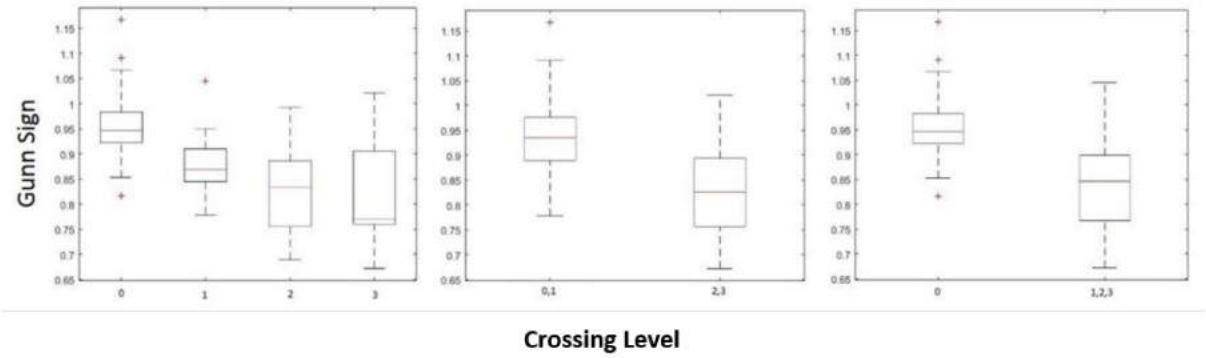

Figure 4.8 Boxplots showing the mean, standard deviations, percentiles and outliers of the Gunn sign for the different grades and groupings of grades. Significant differences ($p < .05$) were found between the normal crossings and all other grades. The same was found when grouping crossings grade 0 and 1 (against grades 2 and 3) and grades 1, 2 and 3.

Table 4.3 Mean and standard deviation results for the Gunn and Salus sign for the 63 crossings. The Gunn sign showed significant difference between normal crossings and all other grades ($p < .05$). This held true when grouping the grades. The Salus sin did not show significant differences between the grades. Gunn sign is unitless and the Salus sign is in radians.

	Grade 0	**Grade 1**	**Grade 2**	**Grade 3**
Gunn	.96 +- .07	.88 +- .08	.83 +- .09	.83 +- .11
	.94 +- .07		.83 +- .09	
	.96 +- .07	.84 +- .09		
Salus	.22 +- .10	.21 +- .08	.28 +- .16	.15 +- .10
	.22 +- .10		.23 +- .15	
	.22 +- .10	.22 +- .13		

4.4 Conclusion

This work presents a method for the automatic quantification of the Gunn and Salus sign in retinal images. Results on two datasets were presented. A set of ten crossings showed separation between the two classes and agreement with the manual graders. Despite the small sample size, the results were promising that both signs could be accurately measured. The second dataset of 63 crossings were broken down into grades of 0 – 3, although the significance of this grading scale is unknown. This dataset showed significant differences between normal crossings and abnormal

crossing as well as groupings of classes for the Gunn sign. The Salus sign did not shows these differences, but this could be for a number of the reasons previously stated. There is still a lack of knowledge as to the importance of the degree or severity of these signs. As of now, they are generally considered binary classification for an ophthalmologist, but future studies may reveal the importance of Gunn/Salus scale, or whether one sign is a better predictor for BRVO and other advance hypertensive retinopathy signs. The quality and resolution of the retinal images used has made this analysis possible. Although no test was done, it is very likely that this method would fail under lesser conditions.

Improvements to the algorithm could be seen by automatically detecting the crossovers. There are many methods to do this [119], [158], but this would have added another layer of error to deal with, while the accuracy of the Gunn and Salus sign calculation was the main goal of this work. Another improvement would be to add an image quality module to ensure the crossover is of sufficient quality before quantification is attempted.

Chapter 5

Tortuosity Measurement

Retinal vessel tortuosity can be an early indicator in diseases such as diabetes and hypertension as well as an important feature for determining the presence of plus disease in retinopathy of prematurity. We present a comparison of many of the popular methods for tortuosity estimation on a new dataset and propose a new method for enhancing retina vessel curvature based on the following publications:

Wigdahl, J., Annunziata, R., Hughes, L., Borooah, S., Trucco, E., Ruggeri, A., Retinal Image Database for Tortuosity Estimation, ARVO 2016

Wigdahl, J., Guimaraes, P., Ruggeri, A., Difference of Gabor Filters as a Curvature Feature in Tortuosity Estimation, Proceedings of the Annual International Conference of the IEEE Engineering in Medicine and Biology Society, EMBS, 2016.

5.1 Introduction

Retinal vessel tortuosity can be used as a biomarker for several eye and systemic vascular diseases including hypertension [159], diabetes type-1 [160], and retinopathy of prematurity [161]. Biologically, tortuosity is an adaptation of the vessels to manage a state of elevated blood pressure. This results in curvature of the vessels that can be measured. There is no globally accepted definition for tortuosity, but many algorithms have been proposed to evaluate tortuosity quantitatively [137], [138], [143], [162], which can be important for classification and progression of disease [163]. Clinicians grade tortuosity qualitatively, usually on a scale of 3-5 points. While more than one algorithm may score particular curves accurately, there may be a single or combination of algorithms that correlates better with the human grader perception of tortuosity, who may be processing more image information than just the vessel segment under analysis, or may deem some curves more important than others. This makes the performance of these tortuosity methods highly dependent on the clinician's opinion, which will inherently vary. Learning or feature-based methods attempt to incorporate the clinician's opinion into the metric and thus have the ability to adapt to the clinician, with the added requirement of a training or tuning phase. Some comparative studies have been performed on tortuosity metrics [134], [140]. To our knowledge, the only freely available dataset specifically for tortuosity is the RET-TORT dataset provided by the University of Padova BioImaging Lab [135]. The addition of new datasets as well as new graders would help determine the robustness of the tortuosity metrics that have been previously proposed.

In this work, we present the tortuosity results from the most widely used metrics on a new dataset, gathered in conjunction with Dundee University in Scotland. We then present a new method for enhancing tortuosity in segmented vessels based on the difference of Gabor filters. Varying only the aspect ratio between a set of Gabor filters and subtracting the responses enhances curvature points along the vessel. The combination of the variables that make up a Gabor filter can also enhance curvature differently, depending on the frequency and amplitude. Combining the curvature enhanced image with well-known methods for tortuosity quantification

creates new metrics that are adaptable to clinician opinion on tortuosity. Results on the RET-TORT dataset and the newly developed dataset confirm the usefulness of the enhancement method.

The rest of the chapter is laid out in the following manner: In Section 5.2, the new dataset is presented and common tortuosity metrics are described and evaluated. Section 5.3 presents the methods for the curvature enhancement. Section 5.4 presents the results and discussion for the enhancement method. Finally, Section 5.5 concludes the chapter.

5.2 Data and Metrics

Images for the new dataset were acquired at the University of Edinburgh, Edinburgh, Scotland using a Canon non-mydriatic camera at 45 degree field of view with 2048x3072 pixels and 3 color channels. One macula centered image was taken for each eye in 37 patients for a total of 74 images. From this set of images, two clinical specialists used semi-automated software to help select and grade individual vessel segments [164]. The first specialist, L.H., selected the start and end points for each vessel segment, chose whether the vessel was an artery or a vein, and assigned a tortuosity value of absent, low, or high. The second specialist, S.B., used the previously marked segments to provide a second, independent tortuosity grade. Fig. 5.1 provides examples of each grade level where there was agreement from both graders. The number of segments per image ranged from 12 to 21. For this work, a subsample of 25 arteries and 25 veins were chosen randomly from each class based on the grades provided by L.H. These vessels were then traced using ImageJ [165] according to the start and end points given. The traces were then converted to a Matlab structure of coordinates from which the vessel can be reproduced. The number of sample points per vessel range from 71 to 383.

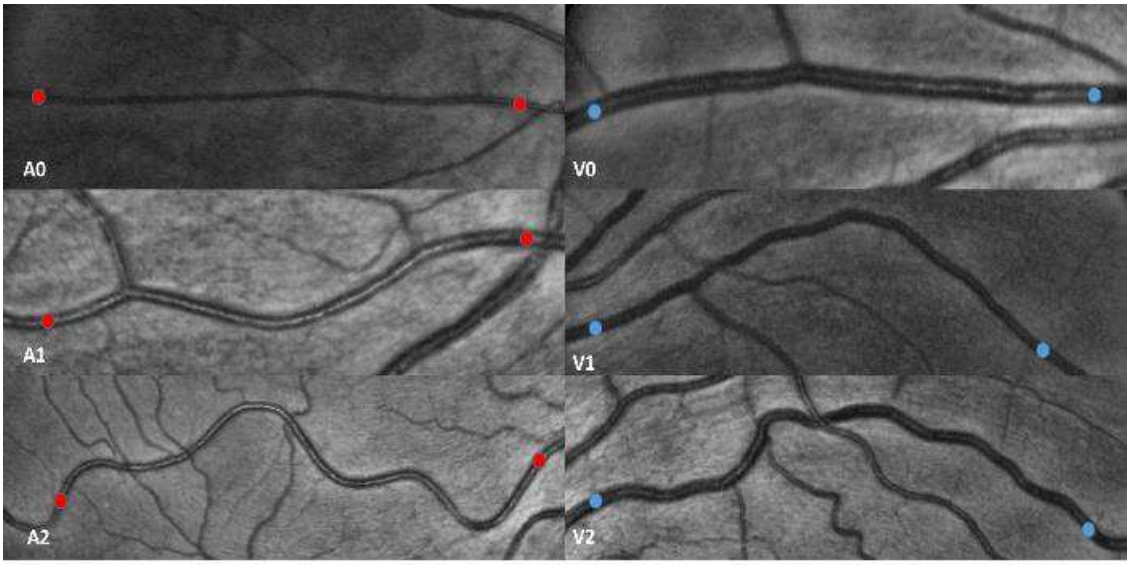

Figure 5.1 Examples of vessels with different grades where the two graders were in agreement. The left column contains arteries and the right veins. A0 - A2 represent grades 0-2 for arteries, with V0-V2 for the veins.

The clinical specialist agreement (Cohen's kappa and linear weighted kappa) was measured for both arteries and veins. Table 1 shows the confusion matrix for both arteries and veins. Agreement was higher for veins (kappa = .73, weighted kappa = .77) in this dataset and the overall agreement for both arteries (kappa = .61, weighted kappa = .67) and veins is considered 'good'. In general, grader S.B. had a tendency towards higher tortuosity grades.

Table 5.1 Confusion matrix between Clinical Specialists for arteries and veins where S is grader S.B. and L is grader L.H. There were minor disagreements between the specialists, generally between the two lowest grades of tortuosity.

Vein Grades	0 (S)	1 (S)	2 (S)	Total
0 (L)	3	1	0	4
1 (L)	0	11	2	13
2 (L)	0	1	7	8
Total	3	13	9	25
Artery	**0 (S)**	**1 (S)**	**2 (S)**	**Total**
0 (L)	2	4	0	6
1 (L)	0	10	2	12
2 (L)	0	0	7	7
Total	2	14	9	25

5.2.1 Tortuosity metrics

A set of 5 methods for calculating tortuosity were chosen to mirror the methods analyzed in a previous study by Lisowska et al. [134]. This section provides a brief overview of these methods.

5.2.1.1 Distance measure (DM)

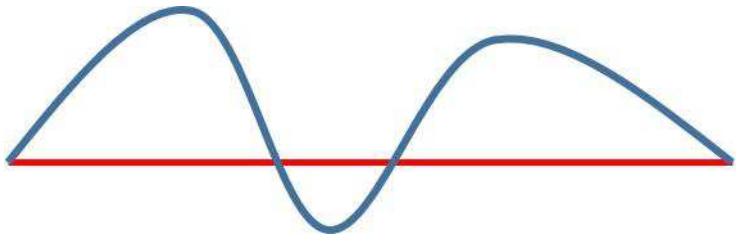

Figure 5.2 Synthetic example of the arch to chord ratio metric. The red line is the chord length from the starting point to the end point of the vessel. The arch length (blue line) is the distance following the path of the vessel.

One of the first metrics to be used to measure tortuosity [133], also known as arch to chord ratio, the DM is described by the following equation and can be visualized in Fig. 5.2:

$$DM = \frac{L_c}{L_x} \tag{5.1}$$

$$L_c = \sqrt{\left(x(t_1) - x(t_0)\right)^2 + \left(y(t_0) - y(t_1)\right)^2} \tag{5.2}$$

$$L_x = \int_{t_0}^{t_1} \sqrt{x'(t)^2 + y'(t)^2 dt} \tag{5.3}$$

Where L_c is the chord length and L_x is the length of the entire vessel. L_C is simply the distance measured from the start of the vessel ($x(t_0)$,$y(t_0)$) to the vessel endpoint ($x(t_1)$,$y(t_1)$). L_x measures the distance along the vessel by summing the changes along the vessel. A completely straight vessel will have a DM of 1. This method is popular due to its simplicity, but has been shown to have shortcomings in previous studies [135]. The metric does not take into account the number of twists. A vessel with one large arching curve will have the same tortuosity value as a vessel with many smaller curves that the clinician is likely to deem more tortuous.

5.2.1.2 Tortuosity density (TD)

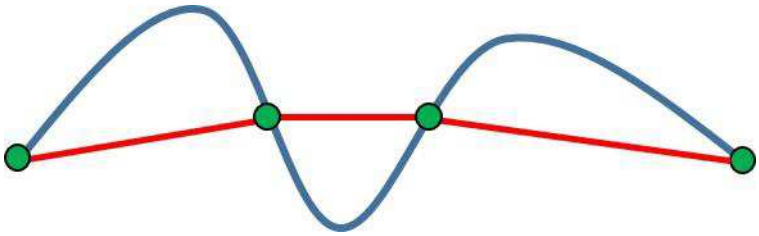

Figure 5.3 The tortuosity density metric incorporates the number of twists along with the arch to chord ratio between each set of inflection points. This is normalized over the length of the vessel.

To build upon the DM (there were intermediary methods as well), a new method was developed by Grisan et al. [135]. This method added a local element to the equation of the DM:

$$TD = \frac{n-1}{n} \frac{1}{L_c} \sum_{i=1}^{n} \left[\frac{L_{csi}}{L_{xsi}} - 1\right] \tag{5.4}$$

Where *n* is the number of inflection points (zero crossings of the second derivative), L_{csi} is the arc length of segment *i,* L_{xsi} is the chord length of segment I, and L_c is the vessel length. This can be visualized in Fig. 5.3. The TD formula considers the local contributions of each convex or concave vessel segment to the overall tortuosity of the segment as well as the number of inflections present. The metric is normalized by vessel length ($1/L_c$). The features of this formula insure that the value of tortuosity increases as frequency, amplitude, and number of turns increase in the vessel. This metric has been shown to be accurate, but performance can suffer under non-ideal sampling conditions [134].

5.2.1.3 Slope chain coding (SCC)

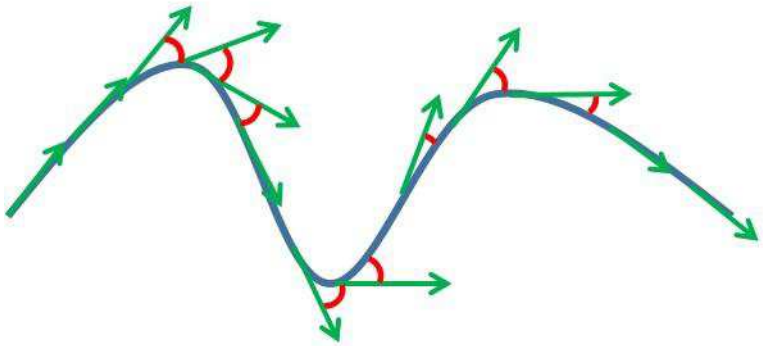

Figure 5.4 Slope chain coding sums the absolute value of slope changes between adjacent line segments. The green arrows represent the vessel broken into line segments with the red angles showing slope differences.

Slope chain coding was proposed by Bribiesca in 2013 [143]. The method approximates a vessel centerline as a piecewise linear curve and calculates the slope change between adjacent line segments (visualized in Fig. 5.4):

$$SCC = \sum_{i=1}^{n} |a_i| \tag{5.5}$$

Where *n* is the number of slope changes and a_i is slope change of the *i*th segment. Variations of this metric will only sum angle changes over a certain threshold such as in formula 5.4.

$$SCC = \sum_{i=1}^{n}(|a_i| \geq \frac{\pi}{6}) \tag{5.6}$$

In this case, the absolute value angle change must be greater than pi/6 to be included in the output. This is done so that small changes and noise (things a clinician would not take into account) do not affect the metric. It has also been shown previously that varying *n* can have a large impact on the output [134] and must be carefully chosen. This metric also does not necessarily increase as sinusoidal frequency increases.

5.2.1.4 Integral curvature measures (τ_3 and τ_5)

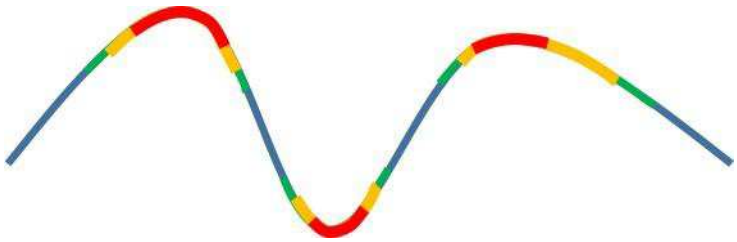

Figure 5.5 Integral measurement sums the total curvature along the vessel. Metrics have looked at the summation of absolute curvature/ total squared curvature and normalization by arch or chord length.

The two best performing measures integrating curvature from Hart et al. [138] were also chosen for testing. The methods are defined below as and visualized in Fig. 5.5:

$$\tau_3 = tsc \tag{5.7}$$

$$\tau_5 = \frac{tsc}{L_x} \tag{5.8}$$

$$tsc = \int_{t_0}^{t_1} k(t)^2 \, dt \tag{5.9}$$

$$k(t) = \frac{x'(t)y''(t) - x''(t)y'(t)}{[y'(t)^2 + x'(t)^2]^{\frac{3}{2}}} \tag{5.10}$$

Where k(t) is the curvature of the vessel segment at *t.* τ_3 (tsc) is the total squared curvature of the vessel described by k(t). τ_5 is this same value normalized by the arch length, L_c, described in formula 5.2. These curvature metrics have also been widely used for tortuosity estimation but don't necessarily follow some of the rules expected of a tortuosity metric (increasing with number of turns and amplitude of turns).

5.2.2 Results

Table 5.2 and Table 5.3 summarize results for each method. For each tortuosity metric, optimal thresholds were chosen to split the data into the 3 groups. This was done after the calculation, as there was no training step to determine thresholds beforehand. This was done separately for each grader and for arteries and veins. This may lead to an overestimation of the agreement, and it is recommended for future studies to perform cross validation to obtain the thresholds. The data could then be compared using Cohen's kappa and linear weighted kappa statistic. The highlighted results show the best outcome per column. The results show that several metrics are joint best for performance in each category. The tortuosity density metric is the most consistent individual metric across both arteries and veins and both graders. The Tau3 metric had the lowest agreement with the graders. This is probably due to the varying lengths of the vessels in this dataset. The Tau5 metric, which is the Tau3 metric normalized over the length the vessel, has better agreement across all categories. The combination of metrics provided good results across all categories. This shows that the different information being captured by these metrics can help to create a more robust metric.

Table 5.2 Agreement between metrics and Graders. Values represent Cohen's kappa and linear weighted kappa statistic.

	Grader 1 (L.H.)				*Grader 2 (S.B.)*			
	Artery		Vein		Artery		Vein	
Metric	k	kw	k	kw	k	kw	k	kw
DM	**0.80**	**0.83**	0.49	0.57	0.66	0.71	0.57	0.65
SCC	0.68	0.73	0.41	0.5	**0.71**	**0.74**	0.41	0.5
TD	0.66	0.7	**0.80**	**0.83**	0.62	0.65	**0.6**	**0.65**
Tau3	0.38	0.44	0.32	0.38	0.53	0.56	0.41	0.46
Tau5	0.65	0.7	0.41	0.46	0.59	0.61	0.49	0.53

Table 5.3 Confusion matrices for all methods, graders and vessel types.

		Grader 1 (L.H.)						**Grader 2 (S.B.)**					
		Artery			**Vein**			**Artery**			**Vein**		
		0	**1**	**2**	**0**	**1**	**2**	**0**	**1**	**2**	**0**	**1**	**2**
DM	**0**	5	1	0	4	0	0	2	0	0	3	0	0
	1	2	10	0	1	8	4	3	11	0	2	6	5
	2	0	0	7	0	3	5	0	2	7	0	0	9
SCC	**0**	4	2	0	4	0	0	2	0	0	3	0	0
	1	2	8	2	2	9	2	0	12	2	3	9	1
	2	0	1	6	0	5	3	0	2	7	0	5	4
TD	**0**	2	4	0	3	1	0	1	1	0	2	1	0
	1	0	12	0	1	12	0	1	13	0	2	10	1
	2	0	1	6	0	1	7	0	3	6	0	2	7
Tau3	**0**	3	3	0	2	2	0	0	2	0	1	2	0
	1	3	7	2	0	12	1	0	12	2	0	11	2
	2	1	1	5	0	6	2	0	2	7	0	4	5
Tau5	**0**	3	2	0	2	2	0	0	2	0	1	2	0
	1	1	11	0	0	12	1	0	14	0	0	11	2
	2	0	2	5	0	5	3	0	3	6	0	3	6

In general, agreement was lower between the metrics and the graders for veins. This is interesting because the agreement between the graders was higher in this category. One difference that may explain this is the global nature of the grading. For comparison, ground truth from the RET-TORT dataset is an ordering of 30 vessels. The graders were given two vessels cropped from their image to compare side by side. This shielded the graders from using more information while choosing their order. In this study, the vessels were graded as part of the entire image. Graders may be influenced by other tortuous vessels in the image as well as other signs, such as vessel thickness. In the hospital setting, the clinician would be combining the vessel

information to give an image-level tortuosity grade, or may have a certain task in mind, which may skew the grades given to individual vessels. Figure 3 shows examples of some commonly misclassified vessels from the dataset where algorithms give lower scores than the graders.

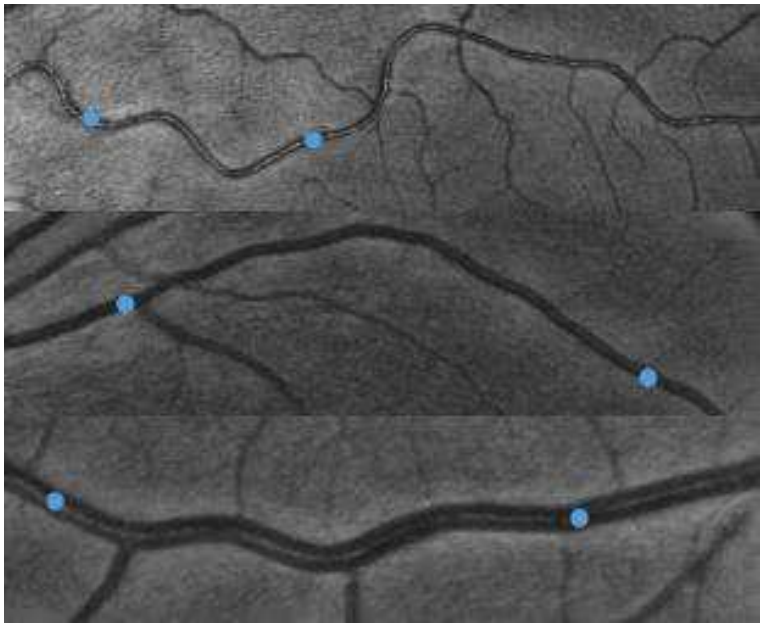

Figure 5.6 Examples of commonly misclassified vessel segments. Algorithms generally gave lower scores than graders.

5.3 Methods

The results from the previous section show that while some metrics performed better than others, results varied heavily between grader and the type of vessel (artery or vein). In order to address these points, this section describes an adaptive method for enhancing curvature that can be paired with the some of the standard methods for tortuosity estimation to create metrics that can change based on grader input to the filters. The method can be applied to the vessel segmentation after separation at key points or to simulated vessel paths built from vessel centerline points connected through interpolation.

5.3.1 Curvature enhancement

The main idea of this method is to transform a binary vessel segment into one that has higher values at points of curvature and lower values along straight segments. To do this, we employ the following family of 2D Gabor functions:

$$g(x, y; \lambda, \theta, \psi, \sigma, \gamma) = \exp\left(-\frac{x'^2+\gamma^2 y'^2}{2\sigma^2}\right)\cos\left(2\pi\frac{x'}{\lambda} + \psi\right) \tag{5.11}$$

$$x' = xcos\theta + ysin\theta \tag{5.12}$$

$$y' = -xcos\theta + ycos\theta \tag{5.13}$$

Where arguments *x* and *y* are the image coordinates, λ represents the wavelength of the sinusoid, θ is the orientation of the normal to the parallel bands in the Gabor function, ψ is a phase offset, σ is the standard deviation of the Gaussian envelope, and γ is the spatial aspect ratio. Formula 5.11 can be broken down into two parts. As noted, the exponential is the Gaussian envelope that is controlled by the standard deviation and the aspect ratio. The cosine represents modulation by a plane wave and controls the angle and wavelength of the Gabor filter. A sample Gabor filter bank is shown in Fig. 5.7.

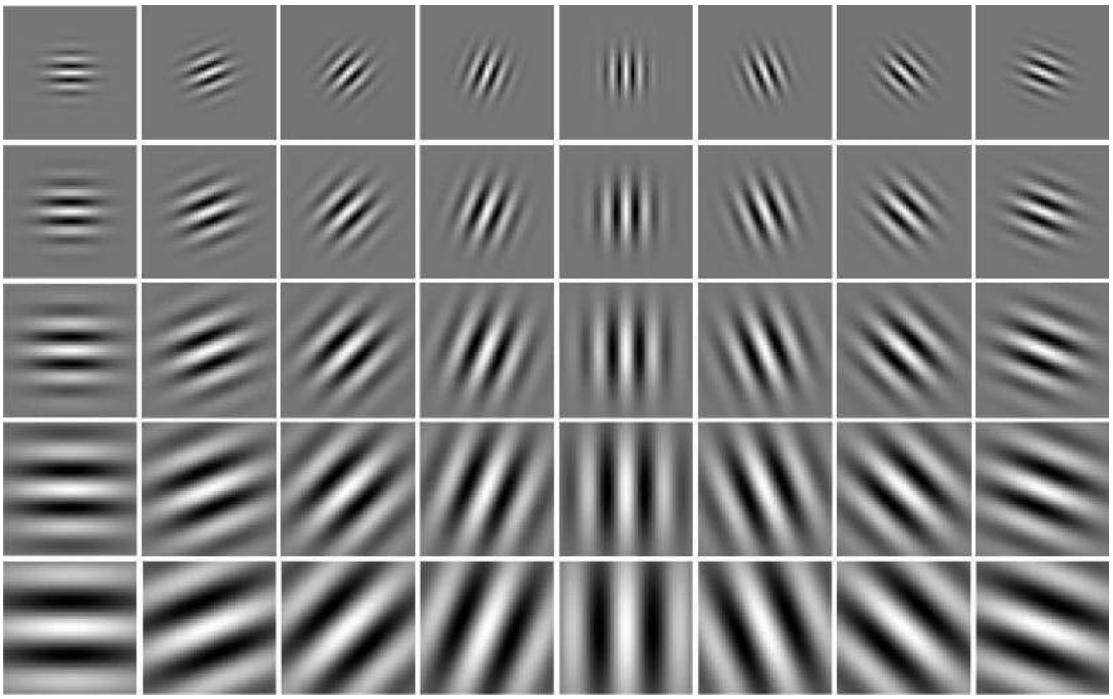

Figure 5.7 A sample Gabor filter array showing changes in angle and wavelength.

The interesting parameter for this work is the aspect ratio which sets the ratio of the semi-major and semi-minor axis of the Gaussian envelope ellipse. The feature of interest is the difference between a relatively typical aspect ratio used for vessel segmentation (typical value around .5) and a more extreme ratio (around .4) which can be seen in Fig. 5.8. In a binary image, with all other parameters being fixed, the difference between the responses will be low in pixels that are part of long straight portions of a vessel and will be higher at curves. This creates a curvature enhanced image that can be used in many different ways to create a single tortuosity value. To show that this is viable, as set of tests were run using synthetic data with Gabor filter banks that only differed in their aspect ratios.. For a fixed width vessel, there is no need to modulate the wavelength of the Gabor filters. Also, the frequency band of the filters is set to two to better model the appearance of vessels.

Figure 5.8 Two Gabor filters. The first shows an elongated Gaussian envelope compared with the second. The width of the profile is constant in both.

The first test was on a simulated straight vessel. Normally, the vessel profile could be modelled with a Gaussian distribution across the vessel profile. However, since we will be working with vessel segmentations, a solid binary profile will show the adequate information. Fig. 5.9 shows

the results. There is no difference between the responses except at the endpoints. This is a byproduct of the process and can be negated by artificially lengthening the vessels and not factoring the response in that region as shown in the third image (where there is still a small difference, but this is due to scaling of the values).

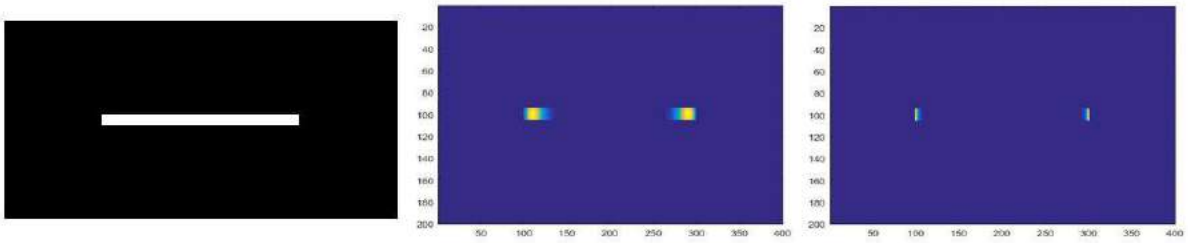

Figure 5.9 Test on synthetic straight vessel. Response shows no difference in the body of the vessel with small differences at the endpoints. This can be negated by knowing the length of the filters used and padding the vessels at the end points. The middle figure shows the typical response without correction. The third figure shows the response after correction by artificially lengthening the vessel.

This shows that the enhancement has the desired effect in straight vessel regions. We now want to look at the response in curves. To do this, a synthetic sinusoidal curve was created as shown in Fig. 5.10. Two different responses were calculated with different aspect ratios. The first response shows increases at the curves that gets larger and peaks at the top of the curve. The second response has lower responses leading up to the curve, but still peaks at the top of the curve. This simulates how the enhancement can be used to adapt to different gradings. The choice of Gabor filter banks can put emphasis on vessels differently, depending on the filter arguments chosen. For the second image Fig. 5.10, an aspect ratio of .4 and .5 were chosen. In the third image aspect ratios of .9 and .95 were chosen. The power of this can be seen well in lower amplitude and/or lower frequency curves (Fig. 5.11) that this method is able to ignore or highlight, depending on grading results.

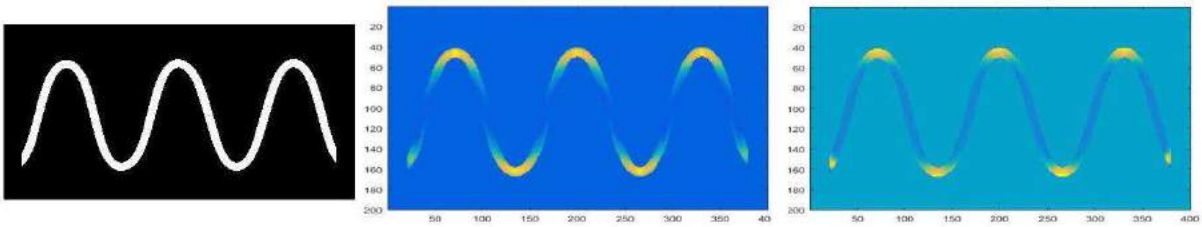

Figure 5.10 Responses to a synthetic sine curve. The first response shows the difference between an aspect ratio of .4 and .5. The second response shows the difference between an aspect ratio of .9 and .95. The second response has lower values leading up to the curve, but still peaks at the tip of the curve.

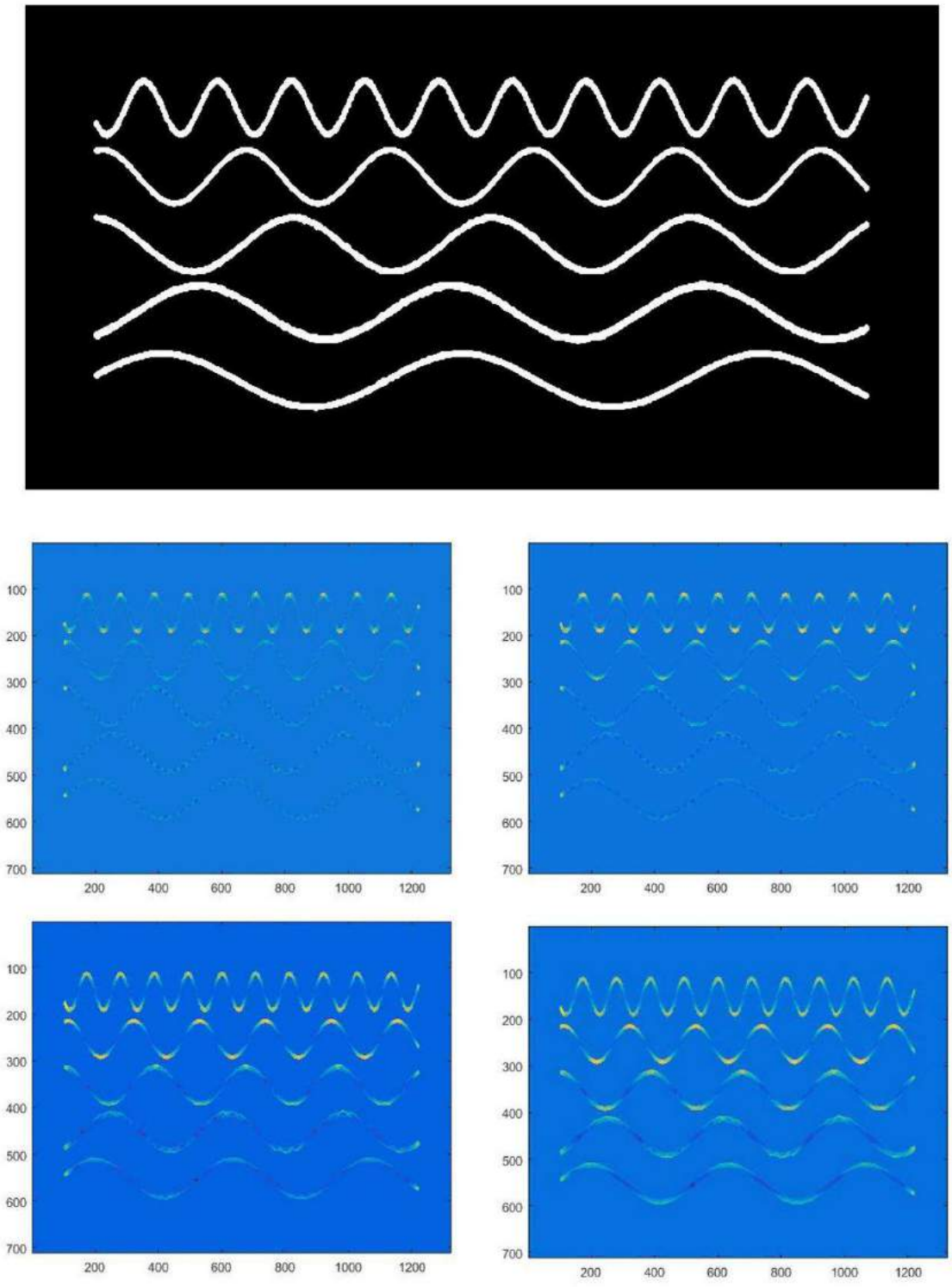

Figure 5.11 Sine waves with different amplitudes. The choice of aspect ratio and difference of aspect ratios is able to highlight the curves differently. Middle Left – aspect ratio .9 and .95. Middle Right – aspect ratio .6 and .7 Bottom Left – aspect ratio .3 and .5 Bottom left – aspect ratio .3 and .8.

5.4 Results and Discussion

5.4.1 Datasets

Testing was performed on the RET-TORT dataset which contains vessel centerline coordinates for 30 arteries and 30 veins [135]. The arteries and veins have been graded by a specialist that was asked to rank the vessel tortuosity from 1-30. Vessel centerline points are provided and bicubic interpolation was used to recreate the vessel paths. The vessel was then dilated using a spherical structuring element with a radius of 3 pixels. We also performed tests using the dataset described earlier in this chapter. That dataset consists of 25 arteries and 25 veins and was graded on a scale of 0 – 2 by two ophthalmic specialists. The same procedure for recreating the vessel centerlines was used for this dataset as well.

5.4.2 Results

By itself, the enhancement method does not give us a tortuosity metric. To create a score, we must combine the curvature enhanced image information. This can be done in a number of ways. We chose to use three as examples, but it should be noted that these are not the only methods that can be used:

(1) - A simple sum of the responses along the vessel. The enhanced image contains information about the curvature. Summing this information up is similar to summing the difference of angles along the curve or calculating the curvature based on integration as we have seen previously in the chapter (Eqs. 5.6, 5.7). This method is labelled the '*Sum'* method.

(2) – The sum the response over the number of vessel pixels. Previously, we have seen many of the metrics normalize based on the length of the vessel. This is similar except we are normalizing of the density of the vessel. This is labelled the '*Density*' method.

(3) Metric two augmented by the number of turns. In previous sections we saw the use of turns as part of tortuosity metrics as a multiply factor, ensuring that the metric would increase as the number of turns increased. Inflection points were used to determine the number of turns. In our method, turns are found as local maxima along the curvature enhanced image. One of the advantages of this method is being able to change the number of turns based on the filter banks used. This is labelled the '*Turn-Curves*' method or '*TC Gabor*'.

Parameters for the Gabor filters were chosen ad-hoc based on performance. The best results for the three methods were found using the difference of aspect ratios of .4 and .5. The wavelength, frequency band, and orientation remained constant between the two filter banks, with values of 15,2 and 0:2:180° (A high amount of angles were used to better represent the vessel paths and insure differences were due to curvature) respectively. Table 5.4 shows the rank correlation for arteries and veins for the different methods proposed on the RET-TORT dataset. The first three entries show the rank correlation using the same filter banks for both arteries and veins. The highest correlation was obtained at .94 for arteries and .88 for veins using a different set of parameters for each type of vessel (arteries – aspect ratios of .4 and .6, veins – aspect ratios of .7 and .9). This compares favorably with Grisan et al. [135], who have produced the highest rank-correlation results on this dataset with their tortuosity density metric described previously. Their results showed correlation values of .949 for arteries and .853 for veins. Examples vessel paths from the RET-TORT dataset along with curvature enhancement results are shown in Fig. 5.12, including alternate results using different aspect ratios.

For the newly developed dataset, we once again found that different filter banks had higher correlation values depending on the type of vessel, and between the different graders. Although we could achieve different and sometimes better results using different filter banks for each of the graders, we felt this would not strengthen the results and would not be consistent with the RET-TORT analysis. In a real world setting, there would be only one ground truth which would

arise from some sort of adjudication between the two graders. Different filter banks were still used for arteries (aspect ratios of .4 and .5) and veins (.5 and .6) to achieve the best results. Table 5.5 shows the breakdown of correlation results between grader and vessel type. The results from other methods, shown earlier in the chapter are also listed. The TC Gabor metric produced the highest correlation values among the proposed metrics. It also outperformed the standard metrics across vessel type and grader. The proposed metric had highest correlation value of .87 with grader 1 on the veins. On average, the method had a higher correlation of .04 with the closest standard tortuosity metric.

Table 5.4 Feature correlation with manual ordering on the RET-TORT dataset using several metric calculations. The best results were achieved by using a different set of filter banks for arteries and vein as well as adapting the arch to chord ratio to include the number of turn curves.

Gabor *Metrics*	*Arteries*	*Veins*
Sum	0.910	0.783
Density	0.901	0.819
Turn-Curves	0.905	0.817
Different filter banks(TC Gabor)	**0.940**	**0.880**

Table 5.5 Correlation results for the proposed dataset. The TC Gabor metric had higher correlation values across both graders and vessel types. Values shown are Pearson's linear correlation coefficients (different from Table 5.2 - treating the ordinal grades in a continuous fashion).

	Grader 1 (L.H.)		Grader 2 (S.B.)	
Metric	***Artery***	***Vein***	***Artery***	***Vein***
DM	0.74	0.62	0.68	0.62
SCC	0.58	0.46	0.53	0.55
TD	0.66	0.56	0.67	0.43
Tau3	0.49	0.33	0.45	0.48
Tau5	0.47	0.48	0.43	0.48
TC Gabor	**0.82**	**0.87**	**0.73**	**0.63**

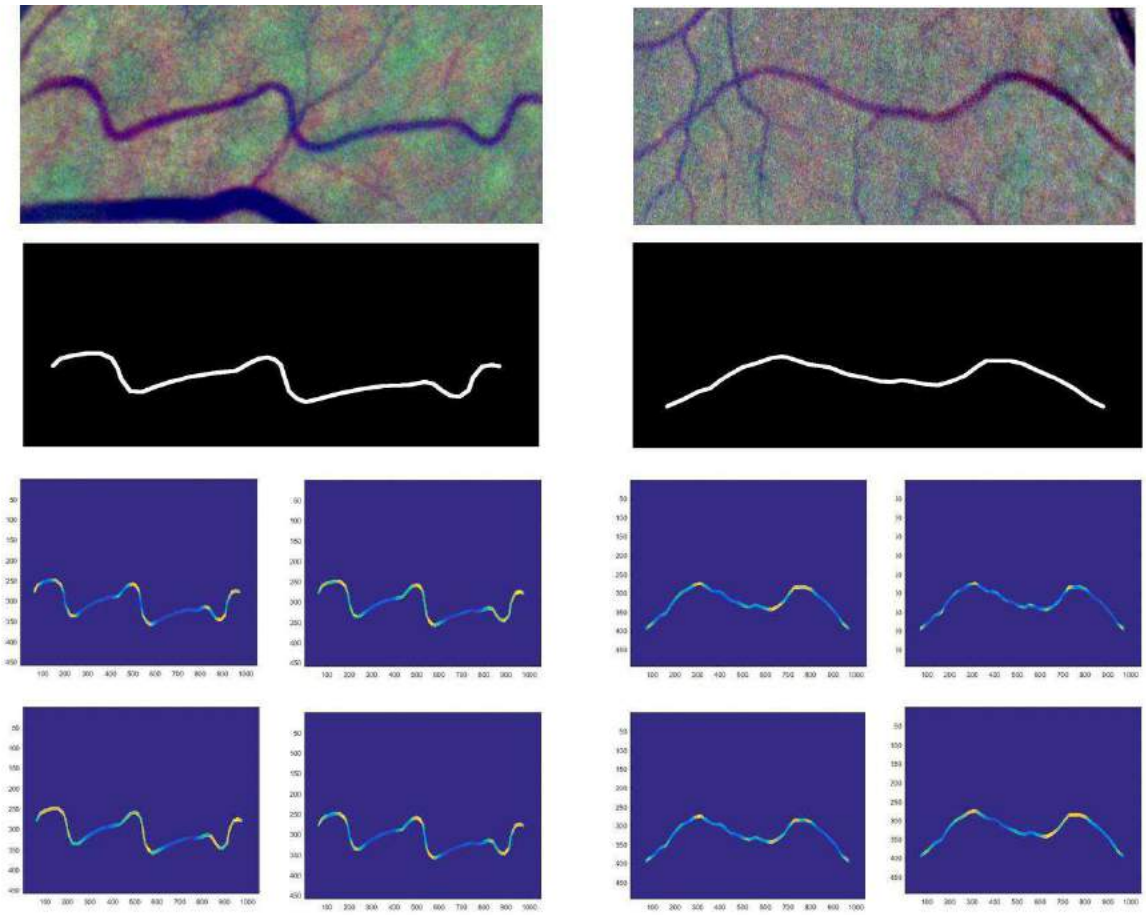

Figure 5.12 Curvature enhancement results for two of the vessels from the RET-TORT dataset. The top left vessel enhancement for each vessel was used in the final scoring. The choice of filter banks in the left vessel made little difference as the curves in this vessel are very sharp. The right vessel has subtle curves that the different filter banks were either able to enhance or ignore.

5.5 Conclusion

This work presented results from part of a new dataset for testing tortuosity metrics. A subset of 50 vessels were chosen and results from popular tortuosity metrics were presented, separated by grader and vessel type. The most stable performance across all categories for this dataset was the tortuosity density metric presented by Grisan et al. [135]. However, results varied widely between the results and the type of vessel and grader. All metrics except Tau3 showed at least good agreement (k>.6) in more than one category. The 3 point grading system, while clinically

relevant, makes direct comparison to studies on the RET-TORT dataset difficult. The findings broadly confirmed those by Lisowska et al. [134] on an independent data set. This work also presented a new feature for curvature enhancement to be used in tortuosity estimation in retinal vessels. The enhancement is based on the difference of aspect ratios between Gabor filter banks. Results on several proposed quantification methods show good agreement with a clinical ordering of retinal vessels on the RET-TORT dataset and performance that outmatches the standard single approaches to tortuosity quantification. The method was also tested using the proposed dataset. Results fell largely in line with those from the RET-TORT dataset, with correlation values slightly above those of the standard metrics across vessel type and grader.

Chapter 6

Retinal Vessel Measurement Framework

This chapter presents the combination of the methods from the previous chapters into a framework for vessel analysis. Previously developed tools at the University of Padova are combined and updated to include this new work. Frameworks such as this can help clinicians add a quantitative analysis to their qualitative findings and can be used to track retinal vascular changes over time. While the system as a whole has not been tested, many of the tools have been available to the public for quite some time and the semiautomatic system allows for corrections in the process. This chapter is loosely based on the following:

Wigdahl, J., Guimaraes, P., Poletti, E., Ruggeri, A., ReVMS (Retinal Vessel Measurement System), ARVO 2015

6.1 Introduction

Continued increases in computer processing power and memory capabilities have led to sophisticated systems for fundus analysis. Algorithms can be combined to perform all the necessary tasks of measuring the vasculature, detecting lesions and/or predicting diseases. This, combined with the ability to store large amounts of medical data, has led to previously unavailable research and business opportunities. Large amounts of publicly available annotated data has been

made available thanks to these advances [10]. Telemedicine screening feasibility has been tested in rural and remote parts of the world [166]–[168]. Countries have started to turn to automatic screening systems to replace parts of the screening pipeline to enhance their medical care and save money [169]. While disease screening generally focuses on lesion detection and/or machine learning, vessel analysis focuses on precise measurement. This usually means semi-automated methods are employed. This combines the ability of the computer (algorithms) to make precise measurements, and the ability of the human to visualize when the computer has made a mistake. This has led to more precise measurements, better ground truth and better monitoring of vascular changes. Better ground truth can lead to better algorithms, and better monitoring can lead to better outcomes for the patient.

This work presents the combination of the algorithms presented in the previous chapters with previously developed algorithms and tools at the University of Padova. The methods allow for user intervention at several stages of the process. The system includes algorithms for optic disc detection, vessel segmentation, key point detection, vessel width measurement, tortuosity estimation, vessel crossover analysis and AV ratio calculation. A sample analysis is presented step by step to show the entire process and a discussion of future additions is discussed. As the system is a collection of algorithms (modular), the addition of new algorithms can be easily achieved for their testing within the system. This will lead to an evolving system that will continually perform faster, more accurate analysis as more modules are developed.

The rest of the chapter is organized in the following manner. In section 6.2, other retinal vascular measurement systems are discussed. Section 6.3 presents the methods for our system with examples. Section 6.4 presents a discussion on the system and section 6.5 concludes the chapter.

6.2 Available Systems

Retinal vessel analysis frameworks have been developed by several groups and companies over the years. There are several systems available for semiautomatic vessel analysis either publicly, for research purposes or for licensing and purchase. Many have been developed over several years, combining algorithms developed at certain institutions into software packages that can be used for measurement by clinicians, or for data collection and ground truth. Some specialize in certain types of images while other have broader use.

The IVAN software system was developed at the University of Wisconsin, department of ophthalmology and visual science and has been used to measure vessel width and AV ratio around the optic disc [170]. The system has been validated in many studies [131], [171] and shown to good agreement with manual measurement, even if these measurements can be a laborious process. The computer-aided image analysis of the retina system (CAIAR) was developed at the department of physics and the department of ophthalmology and visual sciences at Imperial College London [172]. This system is also able to take width measurements as well as provide tortuosity scores for the vessels. The Singapore I vessel analysis system (SiVA) was developed as the combination of many years of research by the Singapore Eye Research Institute (SERI) and the National University of Singapore [173]. This is one of the most complete systems available with modules covering all measurements discussed in chapter 2 as well as fractal analysis and branching angles. The system is available for licensing depending on the use and has training courses available as well. The ARIA system was developed by Peter Bankhead at the Centre for Vision and Vascular Science, Queen's University Belfast [45]. The software consist of freely available Matlab functions based on his work and can be manipulated (with some knowledge) to fit the needs of the user. The system performs a fast vessel segmentation and allows the users to choose vessel segments to analyze. The VAMPIRE system, developed by the University of Dundee and the University of Edinburgh, is a growing set of vascular measurement algorithms with user correction capabilities [164]. The Sirius framework is a web based system which not only

measures tortuosity and AVR, it also quantifies lesion changes. The system also manages medical records and issues reports [174]. The RetinaCAD system, developed at the University of Porto, provides a user interface with the ability to automatically calculate AV ratio, bifurcation geometry and vessel caliber among other features. The user also has the ability to run each step individually or all at once [175]. A few systems have been developed with the main intention of working with retinopathy of prematurity (ROP). Systems such as ROPNet [135], (developed for vessel tracking and tortuosity estimation in narrow field images) and ROPtool [176] (developed by Clarity Medical Systems for vessel width and tortuosity) were developed with these types of images in mind.

6.3 The System

Like many of the other systems available, ours is collection of algorithms and tools developed over many years at the University of Padova. The code was written in Matlab and is not all available publicly yet. The system consists of automatic optic disc detection, which can be manually adjusted, followed by vessel segmentation. The vessels are then skeletonized and broken down into segments based on key point detection and then vessel widths and tortuosity are then estimated. From here, users have the ability to choose cross over points to analyze and choose the vessels for AV ratio calculation. Fig. 6.1 shows a visualization of these steps.

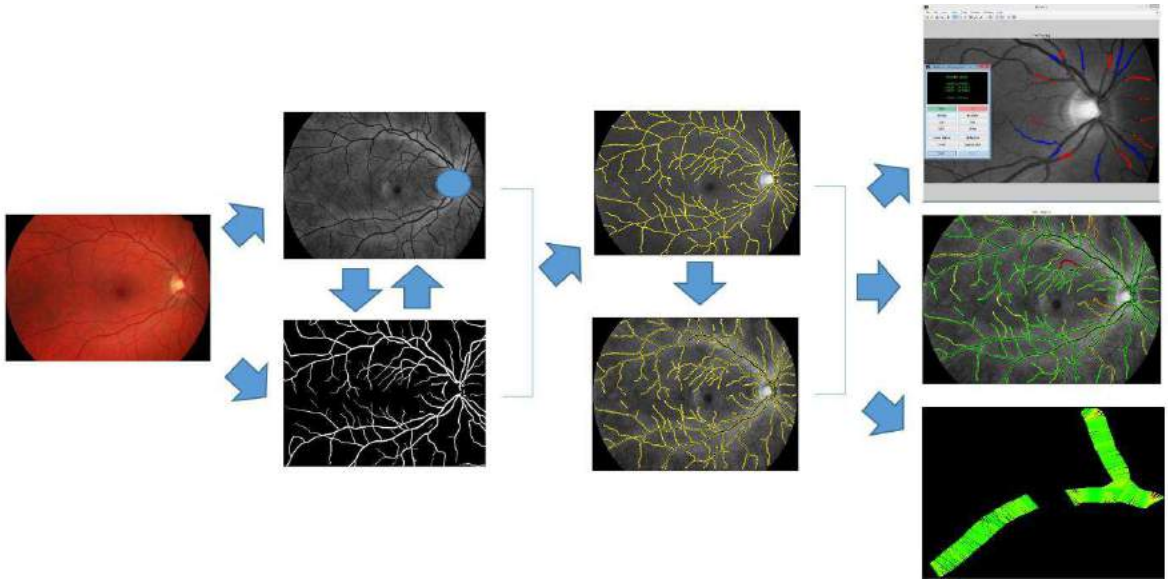

Figure 6.1 A model of the retinal vessel measurement system. The input image is preprocessed and the optic disc and a vessel segmentation is found. The image is skeletonized to and broken into segments based on key points. Vessel widths are calculated as well as tortuosity for each segment. Users then have the ability to pick crossover points to analyze as well as the vessels to use for AV ratio.

6.3.1 Preprocessing

The preprocessing steps are the same mentioned for optic disc detection in Chapter 3. The green channel image is used based on its contrast between vessels and background. The image is first cropped to remove the black background outside the circular field of view. The rest of the background is then mirrored to remove the sharp contrast at the borders. Illumination correction then removes non-uniform background lighting and then contrast enhancement is performed through adaptive histogram equalization. Fig. 6.2 shows these steps in succession.

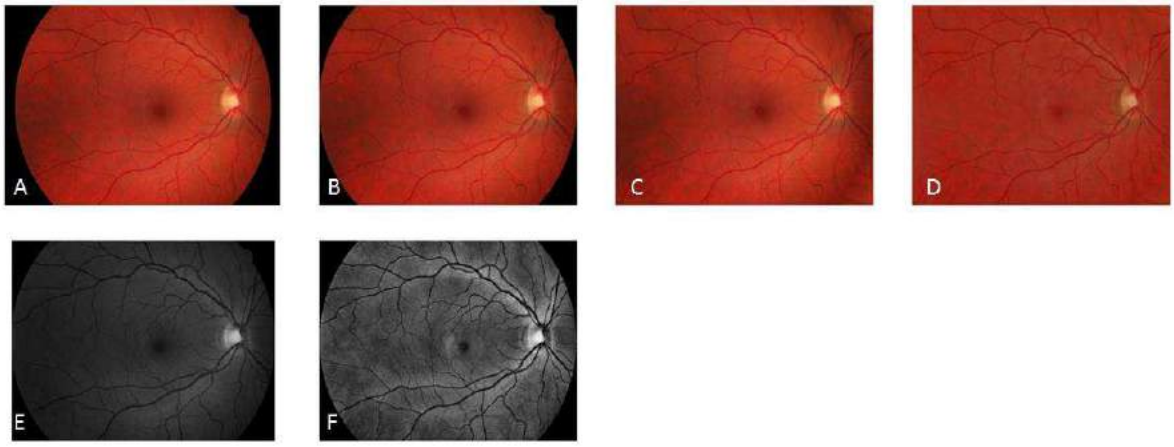

Figure 6.2 Preprocessing steps for the system. The original image (A) is cropped (B) to remove the excess background. The remaining background is then mirrored (C). Background illumination correction is performed (D). Image (E) shows the cropped green channel image and image (F) shows the contrast adjusted image used for optic disc detection and vessel segmentation.

6.3.2 Optic disc detection and vessel segmentation

Previously, the University of Padova had methods for detecting the optic disc and for vessel segmentation. The optic disc detection method developed by Foracchia et al. [81], which used a geometric model of the vasculature, is highly accurate and can even detect the optic disc when it is not present in the image (with enough vessel information). The method looks at vessel direction information and fits a parabola to that information. A vessel segmentation approach was also developed at the university by Grisan et al. [13]. This method is a tracking approach that is initiated by spreading seed points across the image and measuring cross-sectional information to determine centerline pixels on the vessel. This method has the ability to determine vessel key points through a bubble technique that scans circular regions around a pint of interest. While both of these techniques perform well, they are both expensive and take more time than a semi-automated tool should spend on automated portions that can be corrected. Since the algorithm provided in chapter 3 for optic disc detection provides the necessary vessel information to perform a vessel segmentation with little added processing time, it is better suited for this semi-automated tool.

The method for optic disc detection is explained in depth in chapter 3. To get a vessel segmentation from this, we need to look back to the vessel enhanced image. The vessel enhanced image is composed of the maximum responses from the Frangi filters applied to the eigenvalues of the Hessian 2D matrix. A threshold can be derived via Otsu's method [177] or through some form of adaptive thresholding(applying a different threshold to different image patches). Otsu's method performs clustering-based thresholding. The method assume a bimodal histogram and separates the classes by minimizing intra-class variance. After thresholding, we have a binary image of vessel candidates that can be cleaned up through morphological operations. The main difference between the optic disc detection and the vessel segmentation is the information used to create the vessel enhanced image. For vessel segmentation, we want to enhance all vessels in the image. For optic disc detection, we were only interested in the main arcades and secondary vessels. It was previously noted that the Gaussian standard deviations chosen make this a multiscale approach. The standard deviation is directly related to the vessel size being enhanced. To enhance all the vessels in the image, standard deviations covering all sizes of vessels should be chosen. For optic disc detection, only larger values were chosen in an effort to ignore the tertiary vessels. The process for optic disc detection and vessel segmentation are shown in Fig. 6.3.

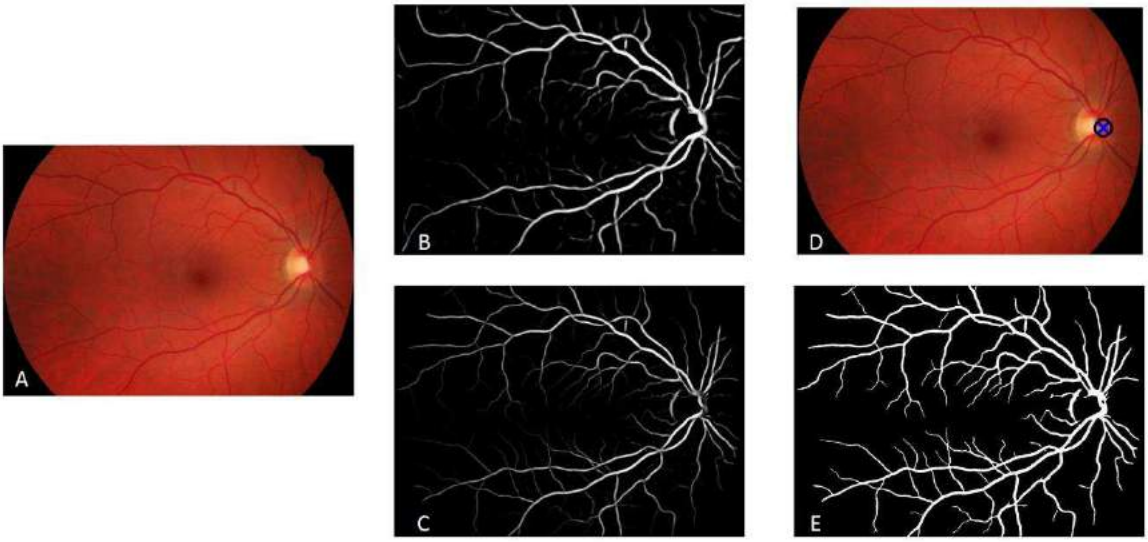

Figure 6.3 The difference between the vessel enhanced information used for optic disc detection and vessel segmentation. The original image (A) is filtered using the Frangi method at larger scales (B) and over the range of vessel sizes (C). (D) The information in B is used to detect the optic disc and the information in C is used to create the vessel segmentation.

Users are then shown the optic disc location along with a circle representing the average optic disc size. The user then has the option to move the optic disc location and adjust the circular boundary to better fit the optic disc (Fig. 6.4). The optic disc mask is used for AV ratio calculation and remove the vessel information in the vessel segmentation.

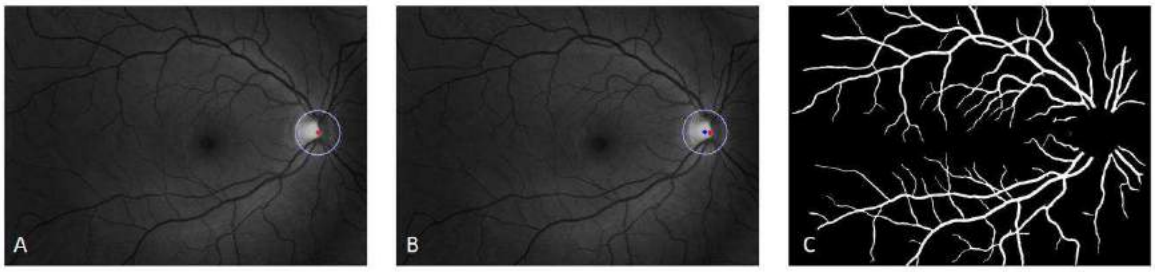

Figure 6.4 After the optic disc is found (A), the location and border can be adjusted by manipulating the ellipse markers (B). The area is then used to remove vessels from the segmentation(C) and for AV ratio calculation (seen later).

6.3.3 Vessel segments and key points

The vessel segmentation is skeletonized by thinning the vessels to a width of one pixel. From the skeleton all key points are found based on the number of nearest neighbors (8 connected) the pixel has. End points will only have one nearest neighbor. Branching points will have at least 3 nearest neighbors and crossover points will have 4. A deeper analysis of the points is needed to determine actual branching and crossover points which is performed as a correction step after the initial segment breakdown. Starting at the key points found, an algorithm walks back through the skeleton, recording locations of the pixels and local directional information until another key point is reached. Each segment then undergoes spline interpolation to produce a smooth path. Since each segment now has its own structure, it is easy to add new fields and keep track of all the information. From Fig. 6.5, it can be seen that the vessels are not always broken down into the segments we would like. For instance, a main arcade should be a single segment until a bifurcation point is reached. To fix this, an algorithm that uses the local directional and contrast information attempts to change vessel segments that may be improperly connected/disconnected due to branches or small irregularities in the vessel skeleton. This procedure was developed by Poletti et al. [178]. The method employs functions for removing, splitting, linking, and extending vessel segments to better fit the vessel information provided. This gives the user an initial set of vessel segments that vessel metrics, such as tortuosity and vessel with, can be run on.

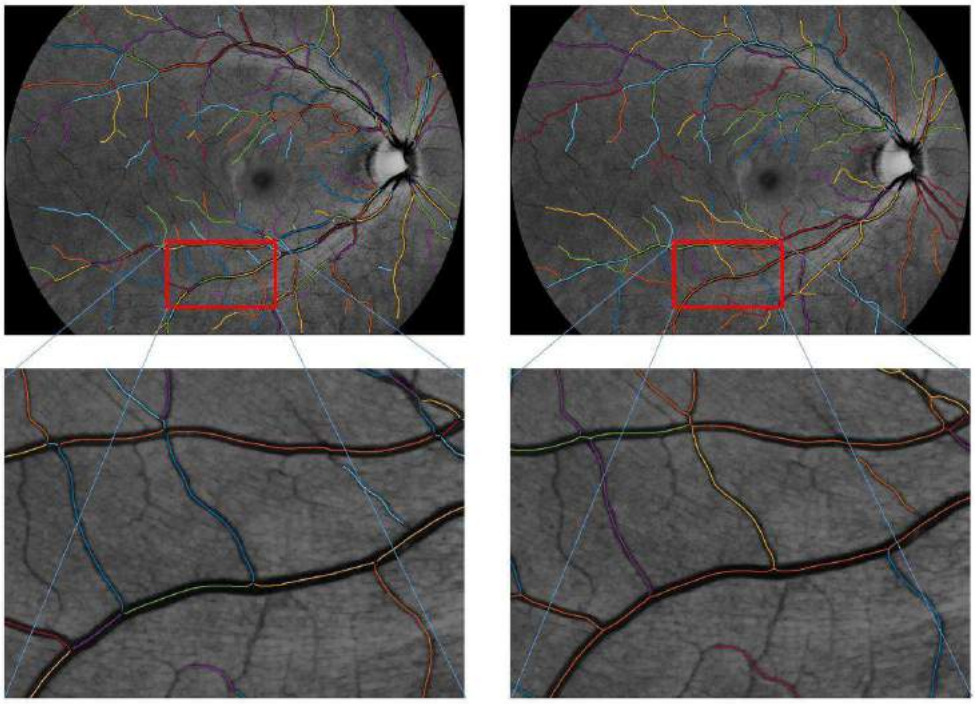

Figure 6.5 Example of the process to break the image into vessel segments. (Top Left) The vessel segments after skeletonization and preliminary key point detection through morphology. (Top Right) Vessel segments interpolated and corrected based on local directional information. (Bottom Left and Right) A zoomed region showing the differences before and after vessel reconnection and correction respectively.

6.3.4 Vessel measurement

To perform many of the semiautomated tasks, such as vessel selection and correction, this system turns to code from a set of web-based tools developed at the University of Padova [31]. The main tools used were Tortnet and AVRnet. While the information for calculating tortuosity, vessel width and AV ratio is already present, these tools provide a user interface for choosing, fixing, adding and deleting vessels. Fig. 6.6 shows examples of the user interfaces for each of these tools. The AVRnet systems uses the initial vessel segments provided and allows the user to manually edit the vessels. It then has a module for calculating the clinical indexes for AV ratio (CRAE, CRVE) [179]. The Tortnet system uses many of the same tools developed for the AVRnet system including the vessel editing. This system displays several tortuosity metrics (now including the proposed method) as well as vessel length, vessel width and distance to the optic disc. The final

metric we calculate is for AV nicking, based on the work in chapter 4. The user is able to click on a crossover of interest and the analysis is performed automatically, providing scores for both the Gunn and Salus sign.

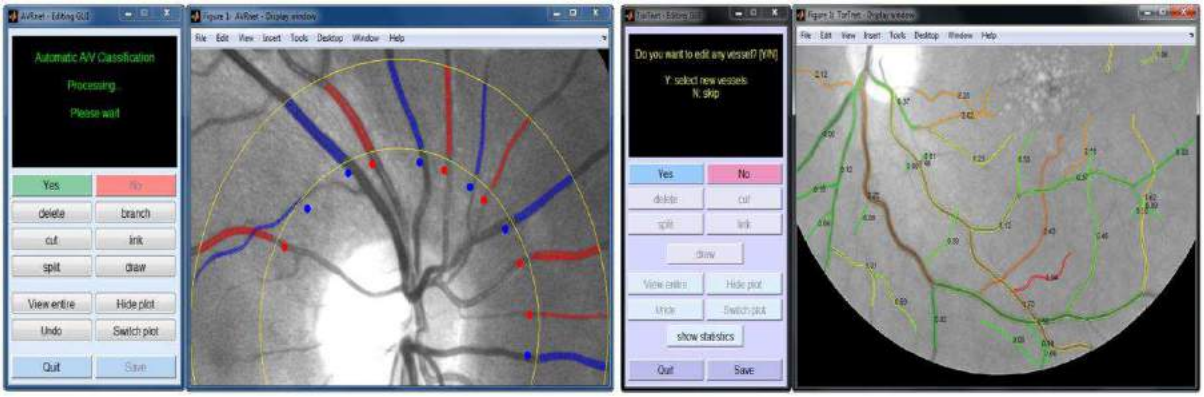

Figure 6.6 Example interfaces from the AVRnet (Right) system and the Tortnet (Left) system. Both of these systems use similar editing interfaces. Images from [31].

6.4 Discussion

The system has been combined so that all vessel metrics can be calculated and includes the algorithms developed in this work. However, the code has many redundancies and is not housed under a single graphical user interface. At this stage, the system is still an in-house tool that will require more work before it is ready to be publicly released. The output is based on a series of figures that the user can interact with depending on the stage of analysis. All of the code was written in Matlab and requires version 2016a or higher as well as the image processing toolbox. The contributions from this thesis have helped to fill out the toolbox for the system by adding highly accurate algorithms for OD detection and tortuosity estimation as well as a new block for measuring AV nicking. There are still other metrics that should also be calculated to add to this system (branching angles, fractal dimension, copper/silver wiring) in the future.

6.5 Conclusion

This chapter presented the combination of the methods developed in the previous chapters with other methods developed at the University of Padova into a retinal vascular measurement

framework. The framework consists of modules for OD detection, vessel segmentation, segment/key point analysis, width estimation, tortuosity estimation, AV ratio and cross over analysis. These are mixed with tools to help the user edit OD location and vessel segments. While not ready for public availability, the tool shows promise in helping clinicians evaluate the retinal vasculature in the near future.

Chapter 7

Conclusions

7.1 Summary of Contributions

To summarize, this thesis has proposed and tested a set of algorithms as part of a retinal vessel analysis framework. New state of the art algorithms for optic disc detection, AV nicking quantification and tortuosity estimation have been added to tool developed previously at the University of Padova into a semiautomatic retinal vessel analysis framework. Fig. 7.1 shows an updated flow diagram of the retinal vessel framework with highlighted contributions from this thesis.

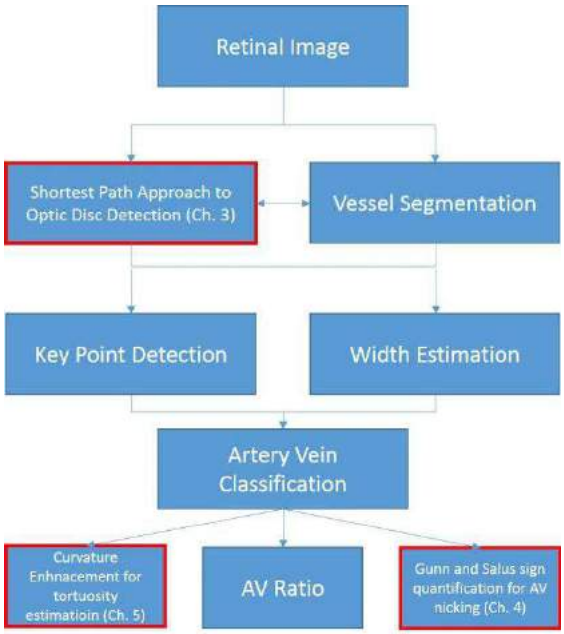

Figure 7.1 A retinal vessel analysis framework with highlighted contributions from this thesis in OD detection, tortuosity estimation and AV nicking quantification.

The first contribution of this thesis is a novel method for optic disc detection in retinal images. We proposed a method that calculates the shortest path between points on the periphery of the image to points on the periphery in the opposite quadrant. Using the values from a vessel-enhanced image as edge weights in our graph, the shortest paths will run along the major vessel paths and through the optic disc location. Doing this multiple times with different sets of points will narrow the region to a small segment. Combining the information from template matching and vessel direction information provides the final optic disc location point. The algorithm was tested on several publicly available datasets (and one in-house dataset) and compared with other methods for optic disc location. In total, the method was tested on 1456 images and had an average detection rate of 99.4%. The method also calculates information that can be used for vessel segmentation (vessel enhancement of which the method is interchangeable). Used in the realm of a retinal vessel measurement framework, this can save overall processing time by performing both steps simultaneously.

The second contribution is a new method for evaluating vessel crossover points for the presence of AV nicking. The method calculates both the Gunn and Salus signs as contributions to nicking. The method takes in a center location of a crossover as input and determines a bounding box for the crossover via vessel segmentation and a distance transform. Vessels widths are calculated using monodimensional matched filters across the profile of vessel. Angles are determined by projecting beams to the edges of vessel segmentation at vessel centerline pixels. The beam with the shortest path is deemed orthogonal to the vessel centerline at that point. The Gunn sign requires measuring vessel widths near and far from the crossing, producing a ratio of these values. The Salus sign sums the difference of the angle entering and exiting the crossover with the average of the rest of the vessel path. Testing was performed on a small set of crossovers showing good correlation with the expert findings and the ability to accurately quantify crossovers for both signs. This was then expanded upon on a larger publicly available dataset which showed

significant ($p < .05$) differences between the Gunn sign of normal crossings and all classes of abnormal crossings.

The third contribution combined a new dataset for tortuosity measurement and a new method for tortuosity estimation based on a curvature enhanced image. The new dataset consists of 50 vessels graded on a scale of 0-2 by two graders. The dataset was tested on many of the popular methods for tortuosity estimation. There was no clearly best method across graders and types of vessel (artery vein), although the method by Grisan et al. [135] had the highest average correlation. This led to the development of new methods for tortuosity estimation that were adaptable to the grader/vessel type. We used a difference of Gabor filters to enhance curvature in the vessel paths. The curvature enhancement is based on the aspect ratio of the Gaussian envelope in the Gabor filter. Different methods for compiling the information were used to create new metrics. They included the sum of the response, the sum divided by the number of vessel pixels, and the sum divided by the number of pixels augmented by the number of curves detected. The curvature enhancement has the ability to put emphasis on certain types of curves, such as a clinician might when grading tortuosity. The method was tested on the RET-TORT dataset and the proposed dataset and compared with individual methods for tortuosity estimation. The method found results that exceeded all individual methods when different filter banks were used for arteries and veins (.94 and .88 correlation respectively) on the RET-TORT dataset. This held true on the proposed dataset, having higher correlation values (on average +.04) for both graders and both vessel types.

The fourth and final contribution is the combination of these methods with previously developed methods at the University of Padova into a vessel analyzer. The system takes parts from the AVRnet and TORTnet systems [31] as well as other works from the past to semi-automatically calculate vessels metrics such as vessel width, tortuosity, AV nicking and AV ratio. While the system is still in the prototype phase, the new algorithms have added needed pieces to

what can eventually become a valuable tool for creating ground truth measurements or helping clinicians monitor vessel abnormalities.

7.2 Future Research

This section briefly describes possible future research based on the work in previous chapters. This mainly includes updates to the retinal vessel analyzer in terms of metrics as well as finishing the prototype:

7.2.1 Other metrics

The metrics presented in the previous chapters are not the only vessel metrics that can be measured and correlate with vascular disease. These include bifurcation angles, copper/silver wiring and fractal analysis. Bifurcation angles would not be difficult to measure with the information we have already gathered in the vessel analyzer. Further, methods have already been developed at the University of Padova to determine bifurcation points when walking through the vessel skeleton [13]. The 'bubbling systems', which looks at concentric circles around vessel centerline pixels, can be augmented to not only track both segments from the bifurcation, but also measure the angle between them. Fig. 7.2 shows an example from the bubble tracking system at a bifurcation point.

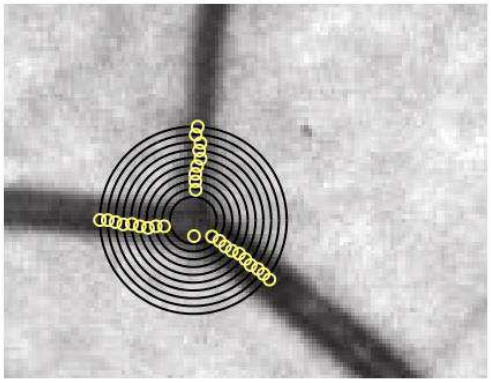

Figure 7.2 Example of the bubble analysis Grisan et al. [13]*, showing tracking of both segments after the bifurcation.*

Copper and silver wiring occur due to an increase in light reflection from the vessel wall due to chronic hypertension. The vessel wall thickens and the blood column thins. This manifests as a change in color along the vessel from bronze (copper wiring) to gray (silver wiring). For copper/silver wiring, vessel profiles are already being analyzed when we measure vessel widths using the monodimensional matched filters. Since both of these would have vessel profiles much different (opposite) than normal vessels, the filters could be trained to detect this along a vessel path. The difficulty is in including the vessels in the vessel segmentation. Their opposite profile usually excludes them from automatic segmentations. This would have to be corrected with semi-automated tools or a 'smarter' vessel segmentation. Fig. 7.3 shows examples of copper and silver wiring.

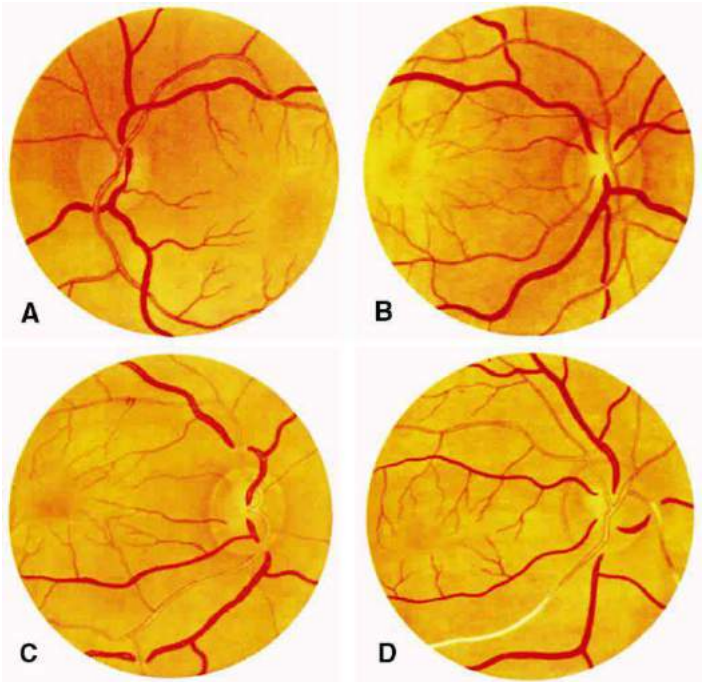

Figure 7.3 (A) Earliest signs of increased arteriolar light reflex. The reflex broadens (B-C) before becoming completely gray in image D (silver wire). From Duane's Ophthalmology [14].

Fractal dimension would also not be a difficult addition as the simpler methods just require a vessel segmentation. Others can be run on the gray-scale image itself. The simplest method that we could deploy is the box counting method, which can be run on the vessel skeleton. To calculate, boxes of size *E,* are overlaid over the image and the number of boxes with a piece of skeleton in them are counted. This is done for increasingly smaller size boxes. The fractal dimension simply the slope of line when plotting the log of the number of boxes with segments and the log of the resolution of those boxes. Fig. 7.4 shows and example of the box counting method.

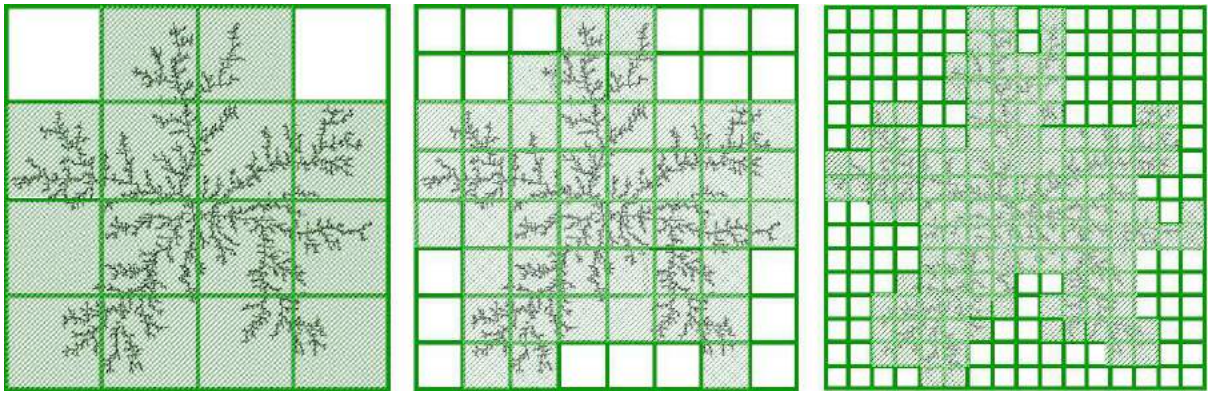

Figure 7.4 Fractal box-counting method using increasingly smaller boxes.

7.2.2 Completing and testing the vessel analyzer

As of now, the vessel analyzer is set of Matlab functions that have been put together to produce the vessel metrics written about. Each module pops up as a separate image that can be semi-automatically adjusted. This needs to be united into a single graphical user interface. There are also several redundancies within the steps. Many of the algorithms perform equal or similar tasks and should not be rerun in the next step. Rectifying these two things and adding the new metrics discussed could provide for commercially available tool to rival the other products mentioned in chapter 6. Once the system has been properly put together, testing should also be done by outside groups to determine the usefulness in terms of speed and accuracy of measurement in a clinical setting. This includes user testing based on disease category. Comparing the effectiveness against other available systems. A new dataset with adjudicated ground truth available for all vessel measurements should be used in these tests, a major undertaking in and of itself.

References

[1] World Health Organization, “Global Report on Diabetes,” vol. 978, p. 88, 2016. ISBN 978 92 4 156525 7

[2] “MEDICAL BLOG: Retinopati Hipertensif.” [Online]. Available: http://lanugojaya.blogspot.com/2010/07/retinopati-hipertensif.html. [Accessed: 28-Jan-2017].

[3] Lhacha, “Retina and Layers.” [Online]. Available: http://www.slideshare.net/Lhacha/retina-and-layers. [Accessed: 01-Jan-2016].

[4] G. Medics, “Age related macular degeneration.” [Online]. Available: http://geekymedics.com/age-related-macular-degeneration/. [Accessed: 01-Jan-2016].

[5] R. C. Store, “KOWA.” [Online]. Available: http://www.retinal-camera.com/kowa.html. [Accessed: 01-Jan-2016].

[6] EyeWiki, “Fluorescein Angiography.” [Online]. Available: http://eyewiki.aao.org/Fluorescein_Angiography. [Accessed: 01-Jan-2016].

[7] R. Gallery, “Fundus Autofluorescence.” [Online]. Available: http://retinagallery.com/displayimage.php?pid=3558. [Accessed: 01-Jan-2016].

[8] A. S. Neubauer, M. Kernt, C. Haritoglou, S. G. Priglinger, A. Kampik, and M. W. Ulbig, “Nonmydriatic screening for diabetic retinopathy by ultra-widefield scanning laser ophthalmoscopy (Optomap),” *Graefe’s Archives for Clinical and Experimental Ophthalmology*, vol. 246, no. 2, pp. 229–235, 2008.

[9] Wikipedia, “Optical choerence tomography.” [Online]. Available: https://en.wikipedia.org/wiki/Optical_coherence_tomography. [Accessed: 01-Jan-2016].

[10] T. Kauppi *et al.*, “DIARETDB1 diabetic retinopathy database and evaluation protocol,” in *Medical Image Understanding and Analysis, University of Wales Aberystwyth , 17-18 th July*, 2007, p. 61.

[11] “E Neurosurgery: Essential information for the budding neurosurgeon.” [Online]. Available: http://www.eneurosurgery.com/fundoscopy.html. [Accessed: 01-Jan-2016].

[12] Wikipedia, “Adaptive Histogram Equalization.” [Online]. Available: https://en.wikipedia.org/wiki/Adaptive_histogram_equalization#cite_note-clahe87-3. [Accessed: 01-Jan-2016].

[13] E. Grisan, A. Pesce, A. Giani, M. Foracchia, and A. Ruggeri, “A new tracking system for the robust extraction of retinal vessel structure.,” *Conference Proceedings IEEE Engineering in Medicine and Biology*, vol. 3, pp. 1620–1623, 2004.

[14] W. Tasman and E. Jaeger, *Duane’s Ophthalmology on DVD-ROM 2010 edition*. Lippincott Williams and Wilkins, 2010.

[15] C. P. Wilkinson *et al.*, “Proposed international clinical diabetic retinopathy and diabetic macular edema disease severity scales,” *Ophthalmology*, vol. 110, no. 9, pp. 1677–1682, 2003.

[16] T. Y. Wong, R. Klein, B. E. K. Klein, J. M. Tielsch, L. Hubbard, and F. J. Nieto, “Retinal microvascular abnormalities and their relationship with hypertension, cardiovascular disease, and mortality,” *Surveys of Ophthalmology*, vol. 46, no. 1, pp. 59–80, 2001.

[17] WHO, “A Global Brief on Hypertension,” *A global brief on hypertension*. p. 40, 2013.

[18] NIH and NHLBI, *Fact Book Fiscal Year 2012*. 2012.

[19] K. D. Kochanek, J. Xu, S. L. Murphy, A. M. Minino, and H.-C. Kung, “National Vital Statistics Reports Deaths : Final Data for 2009,” *National Center for Health Statistics*, vol. 60, no. 3, pp. 1–117, 2012.

[20] O. Hanon, “Hypertension artérielle et démences,” *Ann. Cardiol. Angeiol. (Paris).*, vol. 63, no. 3, pp. 204–208, 2014.

[21] M. Nagai, S. Hoshide, and K. Kario, “Hypertension and Dementia,” *Am. J. Hypertens.*, vol. 23, no. 2, pp. 116–124, 2010.

[22] J. H. Silverstein and a L. Rosenbloom, “Type 2 diabetes in children.,” *Curr. Diab. Rep.*, vol. 1, no. 1, pp. 19–27, 2001.

[23] Centers for Disease Control and Prevention, “National Diabetes Statistics Report , 2014 Estimates of Diabetes and Its Burden in the Epidemiologic estimation methods,” *US Dep. Heal. Hum. Serv.*, pp. 2009–2012, 2014.

[24] R. Mason, “Optimal therapeutic strategy for treating patients with hypertension and atherosclerosis: focus on olmesartan medoxomil,” *Vasc Heal. Risk Manag*, 2011. 7(405), p.16.

[25] R. Turner, “Intensive blood-glucose control with sulphonylureas or insulin compared with conventional treatment and risk of complications in patients with type 2 diabetes (UKPDS 33),” *Lancet*, vol. 352, no. 9131, pp. 837–853, 1998.

[26] B. Neal, S. MacMahon, and N. Chapman, “Effects of ACE inhibitors, calcium antagonists, and other blood pressure lowering drugs: results of prospectively designed overviews of randomised trials,” *ACC Curr. J. Rev.*, vol. 10, no. 3, pp. 28–29, 2001.

[27] D. S. Fong *et al.*, “Retinopathy in Diabetes,” *Diabetes Care*, vol. 27, no. SUPPL. 1, p. S84-S87, 2004.

[28] T. T. Nguyen, J. J. Wang, and T. Y. Wong, “Retinal Vascular Changes in Pre-Diabetes and Prehypertension,” *Diabetes Care*, vol. 30, no. 10, pp. 2708–15, 2007.

[29] G. A. Williams, I. U. Scott, J. A. Haller, A. M. Maguire, D. Marcus, and H. R. McDonald, “Single-field fundus photography for diabetic retinopathy screening: A report by the American Academy of Ophthalmology,” *Ophthalmology*, vol. 111, no. 5, pp. 1055–1062, 2004.

[30] E. Kirkizlar, N. Serban, J. A. Sisson, J. L. Swann, C. S. Barnes, and M. D. Williams, “Evaluation of telemedicine for screening of diabetic retinopathy in the veterans health administration,” *Ophthalmology*, vol. 120, no. 12, pp. 2604–2610, 2013.

[31] A. Ruggeri, S. Member, E. Poletti, D. Fiorin, L. Tramontan, and A. Description, “From Laboratory to Clinic: the Development of Web-based Tools for the Estimation of Retinal Diagnostic Parameters,” in *Proc. Annu. Int. Conf. IEEE Eng. Med. Biol. Soc. EMBS* 2011. (pp. 3379-3382).

[32] D. Fiorin and A. Ruggeri, “Computerized analysis of narrow-field ROP images for the assessment of vessel caliber and tortuosity,” *Proc. Annu. Int. Conf. IEEE Eng. Med. Biol. Soc. EMBS*, pp. 2622–2625, 2011.

[33] S. P. Chow *et al.*, “Comparison of Nonmydriatic Digital Retinal Imaging versus Dilated Ophthalmic Examination for Nondiabetic Eye Disease in Persons with Diabetes,” *Ophthalmology*, vol. 113, no. 5, pp. 833–840, 2006.

[34] P. H. Scanlon, C. Foy, R. Malhotra, and S. J. Aldington, “The Influence of Age, Duration of Diabetes, Cataract, and Pupil Size on Image Quality in Digital Photographic Retinal Screening,” *Diabetes Care*, vol. 28, no. 10, pp. 2448-2453, 2005.

[35] P. H. Scanlon *et al.*, “Comparison of two reference standards in validating two field mydriatic digital photography as a method of screening for diabetic retinopathy.,” *Br. J. Ophthalmol.*, vol. 87, no. 10, pp. 1258–63, 2003.

[36] J. Cuadros, G. Bresnick, and A. Affiliations, “EyePACS: An Adaptable Telemedicine System for Diabetic Retinopathy Screening,” *J. Diabetes Sci. Technol.*, vol. 3, no. 3, pp. 509–516, 2009.

[37] a K. Khurana, *Comprehensive OPHTHALMOLOGY: Fourth Edition*. 2007.

[38] R. SALUS and E. aldstein, “THE FUNDUS OCULI IN GENERALIZED HYPERTENSION AND ARTERIOSCLEROSIS,” *Arch. Ophthalmol.*, vol. 21, no. 3, pp. 505–508, Mar. 1939.

[39] T. Wong and P. Mitchell, “The eye in hypertension,” *Lancet*, vol. 369, no. 9559, pp. 425–435, 2007.

[40] F. K. P. Sutter and H. Helbig, “Familial retinal arteriolar tortuosity: A review,” *Surv. Ophthalmol.*, vol. 48, no. 3, pp. 245–255, 2003.

[41] C. Y.-L. Cheung *et al.*, “Retinal vascular tortuosity, blood pressure, and cardiovascular risk factors.,” *Ophthalmology*, vol. 118, no. 5, pp. 812–8, 2011.

[42] J. J. Staal, M. D. Abramoff, M. Niemeijer, M. a Viergever, and B. Van Ginneken, “Ridge based vessel segmentation in color images of the retina,” *IEEE Trans. Med. Imaging*, vol. 23, no. 4, pp. 501–509, 2005.

[43] E. Decencière *et al.*, “Feedback on a publicly distributed image database: The Messidor database,” *Image Anal. Stereol.*, vol. 33, no. 3, pp. 231–234, 2014.

[44] A. F. Frangi, W. J. Niessen, K. L. Vincken, and M. a Viergever, “Multiscale vessel enhancement filtering,” in *Medial Image Computing and Computer-Assisted Invervention - MICCAI’98. Lecture Notes in Computer Science, vol 1496*, 1998, vol. 1496, pp. 130–137.

[45] P. Bankhead, C. N. Scholfield, J. G. McGeown, and T. M. Curtis, “Fast retinal vessel detection and measurement using wavelets and edge location refinement,” *PLoS One*, vol. 7, no. 3, 2012. e32435

[46] S. Cugati, “Visual Impairment, Age-Related Macular Degeneration, Cataract, and Long-term Mortality,” *Arch. Ophthalmol.*, vol. 125, no. 7, p. 917, 2007.

[47] A. London, I. Benhar, and M. Schwartz, “The retina as a window to the brain-from eye research to CNS disorders.,” *Nat. Rev. Neurol.*, vol. 9, no. 1, pp. 44–53, 2013.

[48] A. . Bron, R. . Tripathi, and B. . Tripathi, *Wolff’s Anatomy of the Eye and Orbit*. London: Chapman & Hall Medical, 1997.

[49] O. Strauss, “The Retinal Pigment Epithelium in Visual Function,” *Physiol. Rev.*, vol. 85, pp. 845–881, 2005.

[50] I. B. Leskov *et al.*, “The gain of rod phototransduction: reconciliation of biochemical and electrophysiological measurements.,” *Neuron*, vol. 27, no. 3, pp. 525–37, 2000.

[51] D. . Schacter, D. Gilbert, and D. . Wegner, *Introducing Psychology*. New York, NY: Worth, 2011.

[52] G. Westheimer, “Spatial Interaction in Human Cone Vision,” *J. Physiol.*, vol. 190, no. 1, pp. 139–154, 1967.

[53] Hubel, David H., Janice Wensveen, and Bruce Wick. *Eye, brain, and vision*. New York: Scientific American Library, 1995.

[54] H. Kolb, “Simple Anatomy of the Retina,” 2011. [Online]. Available: http://webvision.med.utah.edu/book/part-i-foundations/simple-anatomy-of-the-retina/. [Accessed: 01-Jan-2016].

[55] E. Yamada, “Some Structural Features of the fovea centralis in the human retina,” *Arch. Ophthalmol.*, vol. 82, pp. 151–159, 1969.

[56] D. Albert and D. Gamm, “Optic Disk,” *Encyclopedia Britannica*, 2016. [Online]. Available: https://www.britannica.com/science/blind-spot. [Accessed: 01-Jan-2016].

[57] J. B. Jonas, G. C. Gusek, G. Otto, and H. Naumann, “Optic Disc , Cup and Neurorefinal Rim Size , Configuration ond Correlations in Normal Eyes,” vol. 29, no. 7, pp. 1151–1158, 1988.

[58] J. C. Parr and G. F. S. Spears, “General caliber of the retinal arteries expressed as the equivalent width of the central retinal artery,” *Am. J. Ophthalmol.*, vol. 77, no. 4, pp. 472–477, 1974.

[59] M. P. Maker *et al.*, “Automated Retinal Imaging System (ARIS) compared with ETDRS protocol color stereoscopic retinal photography to assess level of diabetic retinopathy.,” *Diabetes Technol. {&} Ther.*, vol. 14, no. 6, pp. 515–522, 2012.

[60] N. Smolek, A. Jaramillo, J. Diamond, and O. Battle, “Image quality and disease screening performance comparison of clinic-based and telemedicine-based retinal cameras,” in *ARVO Imaging Conference*, 2012.

[61] K. Prazdny, “Detection of binocular disparities,” *Biol. Cybern.*, vol. 52, no. 2, pp. 93–99, 1985.

[62] H. R. NOVOTNY and D. L. ALVIS, “A Method of Photographing Fluorescence in Circulating Blood in the Human Retina,” *Circulation*, vol. 24, no. 1, pp. 82–86, 1961.

[63] Y. J. Sepah *et al.*, “Fundus autofluorescence imaging: Fundamentals and clinical relevance,” *Saudi J. Ophthalmol.*, vol. 28, no. 2, pp. 111–116, 2014.

[64] R. H. Webb, G. W. Hughes, and F. C. Delori, “Confocal scanning laser ophthalmoscope.,” *Appl. Opt.*, vol. 26, no. 8, pp. 1492–1499, 1987.

[65] M. T. Witmer, G. Parlitsis, S. Patel, and S. Kiss, “Comparison of ultra-widefield fluorescein angiography with the Heidelberg Spectralis® noncontact ultra-widefield module versus the Optos® Optomap®,” *Clin. Ophthalmol.*, vol. 7, pp. 389–394, 2013.

[66] P. Soliz, A. Larichev, G. Zamora, S. Murillo, and S. Barriga, “Low-cost, high-resolution scanning laser ophthalmoscope for the clinical environment,” in *Proceedings of SPIE*, 2010.

[67] D. Huang *et al.*, “Optical Coherence Tomography HHS Public Access,” *Sci. Novemb.*, vol. 22, no. 2545035, pp. 1178–1181, 1991.

[68] A. G. Podoleanu, “Optical coherence tomography,” *J. Microsc.*, vol. 247, no. 3, pp. 209–219, 2012.

[69] G. S. Negretti, R. Amin, L. Webster, and C. A. Egan, “Does delay in referral of proliferative

diabetic retinopathy from the diabetic eye screening programme lead to visual loss?," *Eye (Lond).*, vol. 30, no. 6, pp. 873–876, 2016.

[70] V. Patel, S. Rassam, R. Newsom, J. Wiek, and E. Kohner, "Retinal blood flow in diabetic retinopathy.," *BMJ*, vol. 305, no. 6855, pp. 678–683, 1992.

[71] R. Klein *et al.*, "Retinal Vascular Abnormalities in Persons with Type 1 Diabetes: The Wisconsin Epidemiologic Study of Diabetic Retinopathy: XVIII," *Ophthalmology*, vol. 110, no. 11, pp. 2118–2125, 2003.

[72] H. P. Hammes *et al.*, "Pericytes and the pathogenesis of diabetic retinopathy," *Diabetes*, vol. 51, no. 10, pp. 3107–3112, 2002.

[73] M. Boulton, D. Foreman, G. Williams, and D. McLeod, "VEGF localisation in diabetic retinopathy.," *Br. J. Ophthalmol.*, vol. 82, no. 5, pp. 561–8, 1998.

[74] R. E. Klein, B. E. K. Klein, S. E. Moss, M. Davis, and D. L. DeMets, "The wisconsin epidemiologic study of diabetic retinopathy: IV. Diabetic macular edema," *Ophthalmology*, vol. 91, no. 12, pp. 1464–1474, 1984.

[75] T. Y. Wong and P. Mitchell, "Hypertensive retinopathy," *N. Engl. J. Med.*, pp. 2310–2317, 2004.

[76] N. Keith, H. Wagener, and N. Barker, "Some different types of essential hypertension: their course and prognosis," *Am. J. Med. Sci.*, vol. 197, no. 3, pp. 332–343, 1939.

[77] J. A. Kylstra, T. Wierzbicki, M. L. Wolbarsht, M. B. Landers, and E. Stefansson, "The relationship between retinal vessel tortuosity, diameter, and transmural pressure," *Graefe's Arch. Clin. Exp. Ophthalmol.*, vol. 224, no. 5, pp. 477–480, 1986.

[78] H. C. Han and Y. C. Fung, "Longitudinal strain of canine and porcine aortas," *J. Biomech.*, vol. 28, no. 5, pp. 637–641, 1995.

[79] A. A. H. A. R. Youssif, A. Z. Ghalwash, and A. A. S. A. R. Ghoneim, "Optic disc detection from normalized digital fundus images by means of a vessels' direction matched filter," *IEEE Trans. Med. Imaging*, vol. 27, no. 1, pp. 11–18, 2008.

[80] A. Hoover and M. Goldbaum, "Locating the optic nerve in a retinal image using the fuzzy convergence of the blood vessels," *IEEE Trans. Med. Imaging*, vol. 22, no. 8, pp. 951–958, 2003.

[81] M. Foracchia, E. Grisan, and A. Ruggeri, "Detection of optic disc in retinal images by means of a geometrical model of vessel structure," *IEEE Trans. Med. Imaging*, vol. 23, no. 10, pp. 1189–1195, 2004.

[82] M. Neimeijer, M. D. Abràmoff, and B. Van Ginneken, "Fast Detection of the Optic Disc and Fovea in Color Fundus Photographs," *Med. Image Anal.*, vol. 13, no. 6, pp. 859–870, 2009.

[83] A. E. Mahfouz and A. S. Fahmy, "Fast localization of the optic disc using projection of image features," *IEEE Trans. Image Process.*, vol. 19, no. 12, pp. 3285–3289, 2010.

[84] D. Welfer, J. Scharcanski, C. M. Kitamura, M. M. Dal Pizzol, L. W. B. Ludwig, and D. R. Marinho, "Segmentation of the optic disk in color eye fundus images using an adaptive morphological approach," *Comput. Biol. Med.*, vol. 40, no. 2, pp. 124–137, 2010.

[85] A. Aquino, M. E. Gegúndez-Arias, and D. Marín, "Detecting the optic disc boundary in digital fundus images using morphological, edge detection, and feature extraction techniques," *IEEE Trans. Med. Imaging*, vol. 29, no. 11, pp. 1860–1869, 2010.

[86] R. J. Qureshi, L. Kovacs, B. Harangi, B. Nagy, T. Peto, and A. Hajdu, “Combining algorithms for automatic detection of optic disc and macula in fundus images,” *Comput. Vis. Image Underst.*, vol. 116, no. 1, pp. 138–145, 2012.

[87] H. Yu *et al.*, “Fast Localization and Segmentation of Optic Disc in Retinal Images using Directional Matched Filtering and Level Sets.,” *IEEE Trans. Inf. Technol. Biomed.*, vol. 16, no. c, pp. 644–657, 2012.

[88] C. Pereira, L. Gonçalves, and M. Ferreira, “Optic disc detection in color fundus images using ant colony optimization.,” *Med. Biol. Eng. Comput.*, vol. 51, no. 3, pp. 295–303, 2013.

[89] T. Yu, Y. Ma, and W. Li, “Automatic localization and segmentation of optic disc in fundus image using morphology and level set,” in *International Symposium on Medical Information and Communication Technology, ISMICT*, 2015, vol. 2015–May, no. 1, pp. 195–199.

[90] J. Rahebi and F. Hardalac, “A new approach to optic disc detection in human retinal images using the firefly algorithm,” *Med Biol Eng Comput*, vol. 54, no. 2, pp. 453–461, 2015.

[91] M. Abdullah, M. M. Fraz, and S. A. Barman, “Localization and segmentation of optic disc in retinal images using Circular Hough transform and Grow Cut algorithm,” *PeerJ*, vol. 4, p. e2003, 2016.

[92] M. M. Fraz *et al.*, “Blood vessel segmentation methodologies in retinal images - A survey,” *Comput. Methods Programs Biomed.*, vol. 108, no. 1, pp. 407–433, 2012.

[93] M. Niemeijer, J. Staal, B. van Ginneken, M. Loog, and M. D. Abràmoff, “Comparative study of retinal vessel segmentation methods on a new publicly available database,” *Proc SPIE Med Imaging [San Diego] 2004*, p. 5370(648 (February)), 2004.

[94] J. V. B. Soares, J. J. G. Leandro, R. M. Cesar, H. F. Jelinek, and M. J. Cree, “Retinal Vessel Segmentation Using the 2-D Morlet Wavelet and Supervised Classification,” *IEEE Trans. Med. Imaging*, vol. 25, pp. 1214–1222, 2006.

[95] E. Ricci and R. Perfetti, “Retinal blood vessel segmentation using line operators and support vector classification,” *IEEE Trans. Med. Imaging*, vol. 26, no. 10, pp. 1357–1365, 2007.

[96] A. Osareh and B. Shadgar, “Automatic blood vessel segmentation in color images of retina,” *Iran. J. Sci. Technol. Trans. B Eng.*, vol. 33, pp. 191–206, 2009.

[97] D. Marín, A. Aquino, M. E. Gegúndez-Arias, and J. M. Bravo, “A new supervised method for blood vessel segmentation in retinal images by using gray-level and moment invariants-based features,” *IEEE Trans. Med. Imaging*, vol. 30, no. 1, pp. 146–158, 2011.

[98] A. Bhuiyan, B. Nath, J. Chua, and K. Ramamohanarao, “BLOOD VESSEL SEGMENTATION FROM COLOR RETINAL IMAGES USING UNSUPERVISED TEXTURE CLASSIFICATION,” in *Image Processing (ICIP)*, 2007, pp. 521–524.

[99] G. B. Kande, P. V. Subbaiah, and T. S. Savithri, “Unsupervised fuzzy based vessel segmentation in pathological digital fundus images,” *J. Med. Syst.*, vol. 34, no. 5, pp. 849–858, 2010.

[100] J. Ng *et al.*, “Maximum likelihood estimation of vessel parameters from scale space analysis,” *Image Vis. Comput.*, vol. 28, no. 1, pp. 55–63, 2010.

[101] A. Hoover, D. Ph, V. Kouznetsova, D. Ph, M. Goldbaum, and S. Diego, “Locating Blood Vessels in Retinal Images by Piece-wise Threshold Probing of a Matched Filter Response vDepartment of Ophthalmology,” *IEEE Trans. Inf. Technol. Biomed.*, vol. 19, pp. 203–210, 2000.

[102] X. Jiang and D. Mojon, “Adaptive local thresholding by verification-based multithreshold

probing with application to vessel detection in retinal images," *IEEE Trans. Pattern Anal. Mach. Intell.*, vol. 25, no. 1, pp. 131–137, 2003.

[103] M. Al-Rawi, M. Qutaishat, and M. Arrar, "An improved matched filter for blood vessel detection of digital retinal images," *Comput. Biol. Med.*, vol. 37, no. 2, pp. 262–267, 2007.

[104] L. Gang, O. Chutatape, and S. M. Krishnan, "Detection and measurement of retinal vessels in fundus images using amplitude modified second-order Gaussian filter," *IEEE Trans. Biomed. Eng.*, vol. 49, no. 2, pp. 168–172, 2002.

[105] S. Chaudhuri, S. Chatterjee, N. Katz, M. Nelson, and M. Goldbaum, "Detection of blood vessels in retinal images using two-dimensional matched filters.," *IEEE Trans. Med. Imaging*, vol. 8, no. 3, pp. 263–269, 1989.

[106] L. Sukkaew, B. Uyyanonvara, S. Barman, A. Fielder, and K. Cocker, "Automatic extraction of the structure of the retinal blood vessel network of premature infants," *J. Med. Assoc. Thail.*, vol. 90, no. 9, pp. 1780–1792, 2007.

[107] M. A. Amin and H. Yan, "High speed detection of retinal blood vessels in fundus image using phase congruency," *Soft Comput.*, vol. 15, no. 6, pp. 1217–1230, 2011.

[108] A. H. Can, H. Shen, J. N. Turner, H. L. Tanenbaum, and B. Roysam, "Rapid automated tracing and feature extraction from retinal fundus images using direct exploratory algorithms," *IEEE Transactions on Information Technology in Biomedicine*, vol. 3, no. 2. pp. 125–138, 1999.

[109] I. Liu and Y. Sun, "Recursive Tracking of Vascular Networks in Angiograms Based on the Detection-Deletion Scheme," *IEEE Trans. Med. Imaging*, vol. 12, no. 2, 1993. pp. 334-341

[110] L. Zhou, M. Rzeszotarski, L. Singerman, and M. Chokreff, "The Detection and Quantification of Retinopathy Using Digital Angiograms," *IEEE Trans. Med. Imaging*, vol. 13, no. 4, 1994. pp. 619-626.

[111] K. K. Delibasis, A. I. Kechriniotis, C. Tsonos, and N. Assimakis, "Automatic model-based tracing algorithm for vessel segmentation and diameter estimation," *Comput. Methods Programs Biomed.*, vol. 100, no. 2, pp. 108–122, 2010.

[112] M. E. Martínez-Pérez, A. D. Hughes, A. V. Stanton, S. A. Thom, A. A. Bharath, and K. H. Parker, "Retinal Blood Vessel Segmentation by Means of Scale-Space Analysis and Region Growing," *Med. Image Comput. Comput. Interv. – MICCAI'99*, pp. 90–97, 1999.

[113] O. Wink, J. Niessen, and M. Viergever, "Multiscale Vessel Tracking," *IEEE Trans. Med. Imaging*, vol. 23, no. 1, pp. 130–133, 2004.

[114] K. A. Vermeer, F. M. Vos, H. G. Lemij, and A. M. Vossepoel, "A model based method for retinal blood vessel detection," *Comput. Biol. Med.*, vol. 34, no. 4, pp. 209–219, 2004.

[115] L. Espona, M. J. Carreira, M. G. Penedo, and M. Ortega, "Retinal vessel tree segmentation using a deformable contour model," *2008 19th Int. Conf. Pattern Recognit.*, pp. 1–4, 2008.

[116] B. Al-Diri, A. Hunter, and D. Steel, "An active contour model for segmenting and measuring retinal vessels.," *IEEE Trans. Med. Imaging*, vol. 28, no. 9, pp. 1488–97, 2009.

[117] K. W. Sum and P. Cheung, "Vessel Extraction Under Non-Uniform Illumination: A Level Set Approach," *IEEE Trans. Biomed. Eng.*, vol. 55, no. 1, pp. 706–711, 2008.

[118] M. E. Martinez-Perez *et al.*, "Retinal Vascular Tree Morphology : A Semi - Automatic Quantification," *Ieee Trans. Biomed. Eng.*, vol. 49, no. 8, pp. 912–917, 2002.

[119] A. Bhuiyan, B. Nath, J. Chua, and K. Ramamohanarao, “Automatic detection of vascular bifurcations and crossovers from color retinal fundus images,” in *Proceedings - International Conference on Signal Image Technologies and Internet Based Systems, SITIS 2007*, 2007, no. January, pp. 711–718.

[120] U. T. V Nguyen *et al.*, “An automated method for retinal arteriovenous nicking quantification from color fundus images,” *IEEE Trans. Biomed. Eng.*, vol. 60, no. 11, pp. 3194–3203, 2013.

[121] J. Lowell, A. Hunter, and D. Steel, “Quantitative measurement of retinal vessel widths from fundus images based on 2d modelling,” *IEEE Trans. Inf. Technol. Biomed.*, vol. 23, no. 10, pp. 1196–1204, 2004.

[122] A. Bhuiyan, B. Nath, J. Chua, and K. Ramamohanarao, “Vessel cross-sectional diameter measurement on color retinal image,” in *International joint conference on biomedical engineering systems and technologies*, 2008. pp. 214-227). Springer Berlin Heidelberg.

[123] R. Chrastek, M. Wolf, K. Donath, H. Niemann, and G. Michelsont, “Automated Calculation of Retinal Arteriovenous Ratio for Detection and Monitoring of Cerebrovascular Disease Based on Assessment of Morphological Changes of Retinal Vascular System,” *IAPR Work. Mach. Vis. Appl.*, vol. 31, 2002. pp. 240-243

[124] E. Grisan and A. Ruggeri, “A divide et impera strategy for automatic classification of retinal vessels nto Arteries and Veins,” in *International Conference of Engineering in Medicine and Biology*, 2003, pp. 890–893.

[125] L. Tramontan, E. Grisan, and A. Ruggeri, “An improved system for the automatic estimation of the arteriolar-to-venular diameter ratio (AVR) in retinal images.,” *Conf. Proc. IEEE Eng. Med. Biol. Soc.*, vol. 2008, pp. 3550–3553, 2008.

[126] K. Rothaus, X. Jiang, and P. Rhiem, “Separation of the retinal vascular graph in arteries and veins based upon structural knowledge,” *Image Vis. Comput.*, vol. 27, no. 7, pp. 864–875, 2009.

[127] M. Niemeijer *et al.*, “Automated measurement of the arteriolar-to-venular width ratio in digital color fundus photographs,” *IEEE Trans. Med. Imaging*, vol. 30, no. 11, pp. 1941–1950, 2011.

[128] A. Zamperini, A. Giachetti, E. Trucco, and K. S. Chin, “Effective features for artery-vein classification in digital fundus images,” *Proc. - IEEE Symp. Comput. Med. Syst.*, 2012. (pp. 1-6)

[129] L. Hubbard, R. Brothers, W. King, L. Clegg, and R. Klein, “Methods for evaluation of retinal microvascular abnormalities associated with hypertension/sclerosis in the Atherosclerosis Risk in Communities Study,” *Ophthalmology*, pp. 2269–2280, 1999.

[130] J. C. Parr and G. F. S. Spears, “General caliber of the retinal arteries expressed as the equivalent width of the central retinal artery,” *Am. J. Ophthalmol.*, 1974. pp 472-477.

[131] M. D. Knudtson, K. E. Lee, L. D. Hubbard, T. Y. Wong, R. Klein, and B. E. K. Klein, “Revised formulas for summarizing retinal vessel diameters.,” *Curr. Eye Res.*, vol. 27, no. 3, pp. 143–149, 2003.

[132] P. K. anti Roy, U. T. V Nguyen, A. Bhuiyan, and K. Ramamohanarao, “An effective automated system for grading severity of retinal arteriovenous nicking in colour retinal images,” *Conf. Proc. ... Annu. Int. Conf. IEEE Eng. Med. Biol. Soc. IEEE Eng. Med. Biol. Soc. Annu. Conf.*, vol. 2014, pp. 6324–6327, 2014.

[133] W. Lotmar, A. Freiburghaus, and D. Bracher, “Measurement of vessel tortuosity on fundus

photographs," *Albr. von Graefes Arch. f??r Klin. und Exp. Ophthalmol.*, vol. 211, no. 1, pp. 49–57, 1979.

[134] A. Lisowska, R. Annunziata, G. K. enneth Loh, D. Karl, and E. Trucco, "An experimental assessment of five indices of retinal vessel tortuosity with the RET-TORT public dataset," in *Conference proceedings : ... Annual International Conference of the IEEE Engineering in Medicine and Biology Society. IEEE Engineering in Medicine and Biology Society. Annual Conference*, 2014, vol. 2014, pp. 5414–5417.

[135] E. Grisan, M. Foracchia, and A. Ruggeri, "A novel method for the automatic evaluation of retinal vessel tortuosity," *IEEE Trans. Med. Imaging*, no. Mx, pp. 310–319, 2003.

[136] E. Bullitt, G. Gerig, S. M. Pizer, W. Lin, and S. R. Aylward, "Measuring Tortuosity of the Intracerebral Vasculature from MRA Images," *IEEE Trans. Med. Imaging*, vol. 22, no. 9, pp. 1163–1171, 2003.

[137] K. V Chandrinos, R. B. Fisher, and P. E. Trahanias, "Image Processing Techniques for the Quanti cation of Atherosclerotic," in *Mediterranian Conference of Medical and Biological Engineering and Computing*, 1998.

[138] W. E. Hart, M. Goldbaum, B. Côté, P. Kube, and M. R. Nelson, "Measurement and classification of retinal vascular tortuosity," *Int. J. Med. Inform.*, vol. 53, no. 2–3, pp. 239–252, 1999.

[139] H. Azegrouz, E. Trucco, B. Dhillon, T. MacGillivray, and I. J. MacCormick, "Thickness dependent tortuosity estimation for retinal blood vessels," in *Annual International Conference of the IEEE Engineering in Medicine and Biology - Proceedings*, 2006, no. Section III, pp. 4675–4678.

[140] E. Trucco, H. Azegrouz, and B. Dhillon, "Modeling the tortuosity of retinal vessels: Does caliber play a role?," *IEEE Trans. Biomed. Eng.*, vol. 57, no. 9, pp. 2239–2247, 2010.

[141] G. Dougherty and J. Varro, "A quantitative index for the measurement of the tortuosity of blood vessels," *Med. Eng. Phys.*, vol. 22, no. 8, pp. 567–574, 2000.

[142] D. Patašius, Martynas; Marozas, Vaidotas; Lukoševičius, Arūnas; Jegelevičius, "Evaluation of tortuosity of eye blood vessels using the integral of square of derivative of curvature," in *proceedings of the 3rd IFMBE European Medical and Biological Engineering Conference*, 2005. pp. 20-25.

[143] E. Bribiesca, "A measure of tortuosity based on chain coding," *Pattern Recognit.*, vol. 46, no. 3, pp. 716–724, 2013.

[144] H. Quigley, A. Brown, J. Morrison, and S. Drance, "The size and shape of the optic disc in normal human eyes," *Arch. Ophthalmol.*, vol. 108, no. 1, pp. 51–57, 1990.

[145] C. Stellingwerf, P. L. Hardus, and J. M. Hooymans, "Two-field photography can identify patients with vision-threatening diabetic retinopathy: a screening approach in the primary care setting.," *Diabetes Care*, vol. 24, no. 12, pp. 2086–90, 2001.

[146] E. T. D. R. S. R. Group, "Grading Diabetic Retinopathy from Stereoscopic Color Fundus Photographs—An Extension of the Modified Airlie House Classification: ETDRS Report Number 10," *Ophthalmology*, vol. 98, no. 5, pp. 786–806, 1991.

[147] E. W. Dijkstra, "A note on two problems in connection with graphs," *Numerische Mathematik*, vol. 1. pp. 269–271, 1959.

[148] V. S. Joshi, M. K. Garvin, J. M. Reinhardt, and M. D. Abràmoff, "Automated method for the

identification and analysis of vascular tree structures in retinal vessel network," *Proc. SPIE Med. Imaging, Comput. Diagnosis*, vol. 7963, p. 79630I–79630I–11, 2011.

[149] J. . M. B. Merickel, M. D. Abramoff, M. Sonka, and X. Wu, "Segmentation of the optic nerve head combining pixel classification and graph search," *Proc. SPIE*, vol. 20, pp. 651215-651215–10, 2007.

[150] K. Zuiderveld, *Contrast Limited adaptive histogram equalization*. Academic Press Professional, Inc, 1994. pp. 474-485

[151] S. S. S. Yoon, M. D. Carroll, and C. D. Fryar, "Hypertension Prevalence and Control Among Adults: United States, 2011-2014.," *NCHS Data Brief*, no. 220, pp. 1–8, 2015.

[152] M. Tso and L. Jampol, "Pathophysiology of hypertensive retinopathy," *Ophthalmology*, vol. 89, no. 10, pp. 1132–1145, 1982.

[153] V. Patel and E. Kohner, *The eye in hypertension*. *Text Book of Hypertension Blackwell Scientific Publications: Oxford* (1994): 1015-1025.

[154] R. Klein, B. E. K. Klein, S. E. Moss, and S. M. Meuer, "the Epidemiology of Retinal Vein Occlusion: the Beaver Dam Eye Study*," *Tr Am Ophth Soc*, vol. 98, pp. 133–143, 2000.

[155] P. Soille, *Morphological image analysis: Principles and Applications*. Springer Science & Business Media, 2013.

[156] E. Poletti and A. Ruggeri, *Graph Search Retinal Vessel Tracking*. *Ophthalmological Imaging and Applications*. CRC Press, 2014. 97-116.

[157] E. Grisan, "Automatic Analysis of Retinal Images: Retinopathy Detection and Grading," Ph.D. thesis, 2005.

[158] D. Calvo, M. Ortega, M. G. Penedo, and J. Rouco, "Automatic detection and characterisation of retinal vessel tree bifurcations and crossovers in eye fundus images," *Comput. Methods Programs Biomed.*, vol. 103, no. 1, pp. 28–38, 2011.

[159] J. S. Wolffsohn, G. A. Napper, S. M. Ho, A. Jaworski, and T. L. Pollard, "Improving the description of the retinal vasculature and patient history taking for monitoring systemic hypertension," *Ophthalmic Physiol. Opt.*, vol. 21, no. 6, pp. 441–449, 2001.

[160] M. B. Sasongko *et al.*, "Alterations in retinal microvascular geometry in young type 1 diabetes," *Diabetes Care*, vol. 33, no. 6, pp. 1331–1336, 2010.

[161] C. Heneghan, J. Flynn, M. O. Keefe, and M. Cahill, "C haracterization of changes in blood vessel width and tortuosity in retinopathy of prematurity using image analysis," *Med. Image Anal.*, vol. 6, pp. 407–429, 2002.

[162] V. Joshi, J. M. Reinhardt, and M. D. Abràmoff, "Automated measurement of retinal blood vessel tortuosity," *SPIE Med. Imaging*, vol. 7624, pp. 1–9, 2010.

[163] A. A. Kalitzeos, G. Y. H. Lip, and R. Heitmar, "Retinal vessel tortuosity measures and their applications," *Exp. Eye Res.*, vol. 106, pp. 40–46, 2013.

[164] A. Perez-Rovira *et al.*, "VAMPIRE: Vessel assessment and measurement platform for images of the REtina," in *Proceedings of the Annual International Conference of the IEEE Engineering in Medicine and Biology Society, EMBS*, 2011, pp. 3391–3394.

[165] M. D. Abràmoff, P. J. Magalhães, and S. J. Ram, "Image processing with imageJ," *Biophotonics Int.*, vol. 11, no. 7, pp. 36–41, 2004.

[166] D. Maberley, H. Walker, A. Koushik, and A. Cruess, “Ontario : a cost-effectiveness analysis,” no. February, 2003.

[167] C. R. Taylor *et al.*, “Improving diabetic retinopathy screening ratios using telemedicine-based digital retinal imaging technology: The vine hill study,” *Diabetes Care*, vol. 30, no. 3, pp. 574–578, 2007.

[168] D. B. Mak, A. J. Plant, and I. McAllister, “Screening for diabetic retinopathy in remote Australia: A program description and evaluation of a devolved model,” *Aust. J. Rural Health*, vol. 11, no. 5, pp. 224–230, 2003.

[169] G. S. Scotland *et al.*, “Cost-effectiveness of implementing automated grading within the national screening programme for diabetic retinopathy in Scotland.,” *Br. J. Ophthalmol.*, vol. 91, no. 11, pp. 1518–23, 2007.

[170] T. Y. Wong, M. D. Knudtson, R. Klein, B. E. K. Klein, S. M. Meuer, and L. D. Hubbard, “Computer-assisted measurement of retinal vessel diameters in the Beaver Dam Eye Study: Methodology, correlation between eyes, and effect of refractive errors,” *Ophthalmology*, vol. 111, no. 6, pp. 1183–1190, 2004.

[171] L. Sherry and J. Wang, “Reliability of computer assisted retinal vessel measurement in a population,” *Clin. Exp. Ophthalmol.*, pp. 179–182, 2002.

[172] C. M. Wilson *et al.*, “Computerized analysis of retinal vessel width and tortuosity in premature infants,” *Investig. Ophthalmol. Vis. Sci.*, vol. 49, no. 8, pp. 3577–3585, 2008.

[173] C. Y. Cheung *et al.*, “Quantitative and qualitative retinal microvascular characteristics and blood pressure,” *J Hypertens*, vol. 29, no. 7, pp. 1380–1391, 2011.

[174] M. Ortega, N. Barreira, J. Novo, M. G. Penedo, A. Pose-Reino, and F. Gómez-Ulla, “Sirius: A web-based system for retinal image analysis,” *Int. J. Med. Inform.*, vol. 79, no. 10, pp. 722–732, 2010.

[175] B. Dashtbozorg, A. M. aria Mendonça, S. Penas, and A. Campilho, “RetinaCAD, a system for the assessment of retinal vascular changes,” *Conf. Proc. ... Annu. Int. Conf. IEEE Eng. Med. Biol. Soc. IEEE Eng. Med. Biol. Soc. Annu. Conf.*, vol. 2014, pp. 6328–6331, 2014.

[176] D. K. Wallace, Z. Zhao, and S. F. Freedman, “A pilot study using ‘ROPtool’ to quantify plus disease in retinopathy of prematurity,” *J. AAPOS*, vol. 11, no. 4, pp. 381–387, 2007.

[177] N. Otsu, “A threshold selection method from gray-level histograms,” *IEEE Trans. Syst. Man. Cybern.*, vol. 9, no. 1, pp. 62–66, 1979.

[178] E. Poletti, D. Fiorin, E. Grisan, and A. Ruggeri, “Retinal Vessel Axis Estimation through a Multi-Directional Graph Search Approach,” in *World Congress on Medical Physics and Biomedical Engineering, September 7 - 12, 2009, Munich, Germany:* Springer Berlin Heidelberg, 2009, pp. 137–140.

[179] L. Tramontan, E. Poletti, D. Fiorin, and A. Ruggeri, “A web-based system for the quantitative and reproducible assessment of clinical indexes from the retinal vasculature,” *IEEE Trans. Biomed. Eng.*, vol. 58, no. 3 PART 2, pp. 818–821, 2011.